

AD-776 414

MELT-GROWN OXIDE-METAL COMPOSITES

GEORGIA INSTITUTE OF TECHNOLOGY

PREPARED FOR
ADVANCED RESEARCH PROJECTS AGENCY

DECEMBER 1973

DISTRIBUTED BY:

NTIS

National Technical Information Service
U. S. DEPARTMENT OF COMMERCE

Unclassified

Security Classification

AD776 414

DOCUMENT CONTROL DATA - R & D

1. ORIGINATING ACTIVITY (Corporate author)		2a. REPORT SECURITY CLASSIFICATION Unclassified 2b. GROUP	
School of Ceramic Engineering Georgia Institute of Technology			
3. REPORT TITLE MELT-GROWN OXIDE-METAL COMPOSITES			
4. DESCRIPTIVE NOTES (Type of report and inclusive dates) (10 June 1971 - 31 December 1973)			
5. AUTHOR(S) (First name, middle initial, last name) Alan T. Chapman, James F. Benzel, J. K. Cochran, Robert K. Feeney, F. W. Ling, J. D. Norgard			
6. REPORT DATE December 1973		7a. TOTAL NO. OF PAGES 217	7b. NO. OF REFS 25
8a. CONTRACT OR GRANT NO. DAAH01-71-C-1046		9a. ORIGINATOR'S REPORT NUMBER(S) E18-604-6	
b. PROJECT NO.		9b. OTHER REPORT NO(S) (Any other numbers that may be assigned to this report) ARPA ORDER NO. 1637	
10. DISTRIBUTION STATEMENT Distribution of this document is unlimited.			
11. SUPPLEMENTARY NOTES		12. SPONSORING MILITARY ACTIVITY Advanced Research Projects Agency 1400 Wilson Boulevard Arlington, Virginia 22209	
13. ABSTRACT This research program was designed to develop melt-grown oxide-metal composite structures for high field electron emission testing. To meet these objectives the research program was divided into five areas: 1) Solidification Behavior of Oxide-Metal Mixtures, 2) The Formation of Optimum Emitting Arrays, 3) Oxide-Metal Composite Properties, 4) Experimental Emission Measurements, 5) Theoretical Analysis of Electron Emitting Arrays. A variety of refractory oxide-metal mixtures have been successfully induction melted and unidirectionally solidified to form aligned metallic fibers embedded in the oxide matrix. Composite structures containing between 5 and 70×10^6 fibers per cm^2 were obtained. Metal solubility in the molten oxides, control of the oxide stoichiometry and metal volatility were shown to be significant parameters controlling the successful composite growth in these systems. Chemical etching and annealing treatments were employed to form a variety of emitter geometries. Emission measurements were performed with a variety of unusual emitter geometries, including metallic coated samples and structures designed to operate at low voltages (< 100V). Several emitter samples have produced current densities above 500 ma/cm^2 . Analysis of post-emission damage and emission performance were used to assess the probable failure mechanism limiting the current density and life of the oxide-metal cathode structures.			

DD FORM 1 NOV 65 1473 (PAGE 1)

S/N 0101.807.6801

Unclassified

Security Classification

235

Unclassified
Security Classification

14 KEY WORDS	LINK A		LINK B		LINK C	
	ROLE	WT	ROLE	WT	ROLE	WT
Oxide-Metal Composites		4				
Field Emission		4				
Rf Heating		3				
Field Emission Theory		3				
Oxides		2				
Refractory Metals		2				
Unidirectional Solidification		4				
Eutectic Structures		3				
UO ₂		2				
ZrO ₂ (Stabilized)		1				
HfO ₂ (Stabilized)		1				
Gd ₂ O ₃		2				
Nd ₂ O ₃		2				
La ₂ O ₃		2				
CeO ₂		2				
Internal Melting		3				
Etching		2				
Tungsten Fibers		4				
Molybdenum Fibers		4				
Electron Emitting Arrays		4				
Oxide-Metal Solidification		3				
High Field Emission		4				

ia

DD FORM 1 NOV 1973 (BACK)
S/N 0102-014-6600

Unclassified

Security Classification

A-31409

AD776 414

Report No. 6

MELT-GROWN OXIDE-METAL COMPOSITES

FINAL TECHNICAL REPORT

(Period: 10 June 1971 - 31 December 1973)

from

THE SCHOOL OF CERAMIC ENGINEERING

GEORGIA INSTITUTE OF TECHNOLOGY

ATLANTA, GEORGIA 30332

PROJECT DIRECTOR: A. T. CHAPMAN

December 1973

Sponsored by:

ADVANCED RESEARCH PROJECTS AGENCY

DEPARTMENT OF DEFENSE

ARPA ORDER NO. 1637

CONTRACT NO. DAAH01-71-C-1046

Distribution of this document is unlimited.

ib.

Reproduced by
NATIONAL TECHNICAL
INFORMATION SERVICE
U S Department of Commerce
Springfield VA 22151

PERSONNEL PARTICIPATING IN PROJECT

Principal Investigators

J. F. Benzel
J. K. Cochran
R. K. Feeney
F. W. Ling
J. D. Norgard

Graduate Students

B. C. Bechtold
M. A. Burke
J. A. Graves
B. A. Keener
W. L. Ohlinger
M. C. Pao
A. V. Petty
G. B. Ricks
J. W. Stendera
J. O. Tarter
M. D. Watson

TABLE OF CONTENTS

<u>Section</u>	<u>Title</u>	<u>Page</u>
I	INTRODUCTION	1
II	SOLIDIFICATION BEHAVIOR OF OXIDE-METAL MIXTURES	7
A.	Induction Coupling and Solidification Behavior of Oxide-Metal Mixtures	7
1.	Yttria Stabilized ZrO_2 -W and HfO_2 -W	8
2.	UO_2 -W	10
3.	Rare Earth Oxide-Metal Systems	26
4.	Al_2O_3 (Cr_2O_3)-W or Mo	47
5.	Cr_2O_3 -Mo	49
B.	Effect of Lowering Rate on the Eutectic Composition of Unidirectionally Solidified Oxide-Metal Mixtures	51
C.	Electron Beam Melting and Solidification of Oxide-Metal Systems	53
D.	Possible Banding Mechanisms in Oxide-Metal Composites	55
E.	X-Ray Analysis of Oxide-Metal Composites	60
III	THE FORMATION OF OPTIMUM EMITTING ARRAYS	70
A.	UO_2 -W Emitting Arrays	71
B.	Gd_2O_3 -Mo Emitting Arrays	82
IV	OXIDE METAL COMPOSITE PROPERTIES	95
A.	Electrical Resistivities	96
B.	Thin Films	100
1.	Apparatus and Calibration	101
2.	Coating Studies	109
V	EXPERIMENTAL EMISSION MEASUREMENTS	119
A.	Summary of Previous Experimental Work	119
B.	Electron Emission Measurements	123
1.	Metallic Overcoatings	129
2.	Annealed Tips	133
3.	Low Voltage Electron Guns	136
4.	Emission Life-Time Testing	141
5.	High Current Density Emitters	146
6.	Other Composite Materials	150
7.	Resistive Coated Samples	153
C.	Analysis of Emitter Failure	155
D.	Summary	162

TABLE OF CONTENTS (Continued)

<u>Section</u>	<u>Title</u>	<u>Page</u>
VI	THEORETICAL ANALYSIS OF ELECTRON EMITTING ARRAYS	163
A.	Introduction	163
B.	Model	165
C.	Numerical Analysis	169
D.	Analytical Analysis	175
E.	Field Emission Equations	189
F.	The Fowler-Nordheim Plot	192
G.	Summary	204
VII	SUMMARY	205

LIST OF ILLUSTRATIONS

<u>Figure</u>	<u>Title</u>	<u>Page</u>
I-1	Schematic Diagram of the Facility for the Growth of Oxide-Metal Composites.	3
II-1	Degeneration of Uniform Composite Structure because of Reduced W Solubility in Molten UO_2 .	14
2	Microstructure of UO_2 -W Samples Solidified in $CO + 4$ v/o CO_2 Showing Fine W Needles and Platelets.	20
3	Uniform and Continuous UO_2 -W Composite Structures in Samples Solidified in $CO + 1$ v/o CO_2 .	23
4	Effect of Growth Rate on Molybdenum Fiber Density in Gd_2O_3 - CeO_2 -Mo Composites.	29
5	Disordered Composite Morphology of CeO_2 Doped Gd_2O_3 -Mo Sample Grown at 5 cm/hr. Dark Field, X600.	31
6	CeO_2 Doped Gd_2O_3 -Mo Sample Grown at 4 cm/hr Displaying Mo Fibers in the Cell Interior Which Gradually Grade to Platelets at the Cell Boundary. Dark Field, X600.	32
7	CeO_2 Doped Gd_2O_3 -Mo Sample Grown at 2 cm/hr Showing Cells Essentially Composed of Narrow Mo Platelets. Dark Field, X800.	32
8	Comparison of the Size of CeO_2 Doped Gd_2O_3 -Mo Composite Samples Initially Prepared by Uniaxial Pressing in a Steel Die (Right Pellet) and Iso-Pressing in a Rubber Mold (Left Rod).	34
9	Proposed Phase Diagram for the System CeO_2 Doped Gd_2O_3 -Mo Including Non-Equilibrium Subsolidus Region of Eutectic Growth.	37
10	Transverse Sections of a CeO_2 Doped Nd_2O_3 -Mo Sample Showing the Transition from Fiber to Platelet Morphology from the Base to Top of Solidified Zone. Dark Field, X600.	41
11	Longitudinal Section of CeO_2 Doped Y_2O_3 -Mo Samples Grown in a $N_2 - 10$ v/o H_2 Atmosphere. Dark Field, X600.	45

LIST OF ILLUSTRATIONS (Continued)

<u>Figure</u>	<u>Title</u>	<u>Page</u>
II-12	Longitudinal Section of CeO_2 - 10 w/o Mo Sample (Showing Mo Platelets) Solidified in a N_2 - 10 v/o H_2 Atmosphere. Dark Field, X600.	48
13	Longitudinal Section of CeO_2 - 10 w/o Mo Sample (Displaying Oxide Dendrites) Solidified at 2.8 cm/hr. Dark Field, X600.	48
14	Eutectic Regions in Cr_2O_3 -Mo(Cr) Samples Solidified in a Mo Crucible.	50
15	Effect of Growth Rate on v/o Mo Present as Fibers in Gd_2O_3 - CeO_2 -Mo Composites.	52
16	Banding Produced by a Power Fluctuation in a Y_2O_3 Stabilized ZrO_2 -W Composite. Dark Field, X600.	56
17	Fan Type Banding in Oxide-Rich Area of a Y_2O_3 Stabilized ZrO_2 -W Composite. Dark Field, X600.	57
18	Thin Oxide Band With Aligned Fibers in a Y_2O_3 Stabilized ZrO_2 -W Composite. Dark Field, X600.	58
19	Schematic Diagram of Steps Leading to a Thin Oxide Band During a Minor Remelt.	61
20	The Orientation Relationships of the Metal Fibers and Oxide Matrix in a Single Cell from UO_2 -W Sample No. 113-23-1. Hollow Marks are Poles of the Fibers; Solid Marks are Poles of the Matrix.	63
21	Laue Pattern for Single Cell from UO_2 -W Sample No. 113-23-1.	64
22	The Orientation Relationships of the Metal Fibers and Oxide Matrix in a Single Cell from UO_2 -W Sample No. 113-23-2. Hollow Marks are Poles of the Fibers; Solid Marks are Poles of the Matrix.	66
23	Laue Pattern for Single Cell from UO_2 -W Sample No. 113-23-2.	67

LIST OF ILLUSTRATIONS (Continued)

<u>Figure</u>	<u>Title</u>	<u>Page</u>
III-1	UO ₂ -W Composite Displaying W Pins Recessed In Oxide Matrix. Scanning Electron Micrograph, X6,400.	72
2	Plot of Hole Depth vs. Etching Time for UO ₂ -W Composite in K ₃ Fe(CN) ₆ -NaOH Etchant.	75
3	Blunt Tip Shapes Obtained in UO ₂ -W Composite by Etching of Holes with K ₃ Fe(CN) ₆ -NaOH Etchant. Scanning Electron Micrograph, X10,600.	77
4	Rounded Tip Shapes Obtained by Annealing of UO ₂ -W Composite in Which W Has Been Selectively Removed by K ₃ Fe(CN) ₆ -NaOH Etchant. Scanning Electron Micrograph, X10,900.	77
5	Initially Cylindrical, Unpointed W Pins in UO ₂ -W Composite after Annealing at 1600°C for 15 minutes. Scanning Electron Micrograph, X10,000.	78
6	Pointed W Pins in UO ₂ -W Composite As Etched. Scanning Electron Micrograph, X11,200.	78
7	Rounding of Initially Pointed W Pins in UO ₂ -W Composite Produced by Annealing at 1600°C for 15 Minutes. Scanning Electron Micrograph, X11,500.	80
8	Rounding of W Pins in UO ₂ -W Composite Produced by Annealing of Pins at 1400°C for 25 Minutes. Scanning Electron Micrograph, X10,500.	80
9	Unannealed Gd ₂ O ₃ -Mo Composite Etched to Expose Fibers. Scanning Electron Micrograph, X4,800.	84
10	Plot of Exposed Fiber Length vs. Etching Time for Gd ₂ O ₃ -Mo Composite in H ₂ SO ₄ -12% Methyl Alcohol Etchant.	86
11	Gd ₂ O ₃ -Mo Composite Displaying Pointed Fibers Resulting from NH ₄ NO ₃ Addition to H ₂ SO ₄ Etchant. Etched by rotation at 20 rpm. Electron Micrograph, X11,700.	88

LIST OF ILLUSTRATIONS (Continued)

<u>Figure</u>	<u>Title</u>	<u>Page</u>
III-12	Gd ₂ O ₃ -Mo Composite Etched in NH ₄ NO ₃ -H ₂ SO ₄ Etchant Utilizing Rotation and Electrosonic Agitation. Scanning Electron Micrograph, X2,350.	88
13	Rounded Tip Shapes in Gd ₂ O ₃ -Mo Composite Produced by Annealing of Initially Pointed Mo Pins at 1200°C for 25 Minutes. Scanning Electron Micrograph, X12,200.	90
14	Plot of Hole Depth vs. Etching Time for Gd ₂ O ₃ -Mo Composite in K ₃ Fe(CN) ₆ -NaOH Etchant.	92
15	Gd ₂ O ₃ -Mo Sample Showing Pointed Pins Recessed in Holes Produced by Two-Step Etching Process. Scanning Electron Micrograph, X1,000.	94
IV-1	Schematic of Ion Beam Coater.	103
2	Diagram of Ion Beam Coater Stage Utilizing Vibrating Quartz Crystal Thickness Monitor.	106
3	Effect of Ion Beam Current and Accelerating Potential on Deposition Rate of Molybdenum	108
4	Scanning Electron Micrograph of 1000 Å Gold Deposit on UO ₂ -W Sample No. 31-12-1, X6,400.	110
5	Scanning Electron Micrograph of UO ₂ -W Sample No. 25-59-10 Prior to Molybdenum Deposition, X10,000.	112
6	Scanning Electron Micrograph of UO ₂ -W Sample No. 25-59-10 Coated with 1000 Å of Molybdenum Showing Rounded Pin Tips, X11,000.	112
7	Scanning Electron Micrograph of UO ₂ -W Sample No. 25-59-10 Coated with 1000 Å of Molybdenum Showing "Collar" Deposits, X5,700.	113
8	Scanning Electron Micrograph of UO ₂ -W Sample No. 25-59-10 Coated with 1000 Å of Molybdenum Showing Deposit Sheets On Fiber Ends, X5,700.	113

LIST OF ILLUSTRATIONS (Continued)

<u>Figure</u>	<u>Title</u>	<u>Page</u>
IV-9	Scanning Electron Micrograph of UO_2 -W Sample No. 31-39-8/30/20-33/62 Coated with 1000 Å of Mo Prior to Emission Testing, X25,500.	114
10	Scanning Electron Micrograph of 1800 Å Platinum Coating Deposited on Recessed Pin Composite Showing Holes Remaining After Deposition, X5,150.	116
V-1	Pre- and Post-Emission Scanning Electron Micrographs of Sample No. 25-66-7/113-31Y/54,56,57,58.	131
2	Pre- and Post-Emission Scanning Electron Micrographs of Heat Treated UO_2 -W Sample No. 31-12-2/11-71/59.	135
3	Scanning Electron Micrograph Showing Type of Recessed Pin Geometry Used In Low Voltage Electron Gun Experiments. UO_2 -W Sample No. 25-99-4/11-67/55 Not Overcoated. X5,270. 0° View.	137
4	Schematic Diagram of Gold-Overcoated Low Energy Electron Gun.	137
5	Conventional Test Diode Modified For Low Voltage Emission.	139
6	Scanning Electron Micrograph of Long-Term UO_2 -W Emission Sample No. 113-25/23-28B/Pl. Pre-Emission. X5,695.	143
7	Scanning Electron Micrographs of Long-Term UO_2 -W Sample No. 113-25/23-28B/P2.	145
8	Pre-Emission Scanning Electron Micrograph of UO_2 -W Annealed Samples No. 25-59/11-79/63 and 25-59-1/11-81/23-53/64.	147
9	Post-Emission Scanning Electron Micrograph of UO_2 -W Sample No. 25-59/11-79/63. X800.	151
10	Post-Emission Scanning Electron Micrograph of UO_2 -W Sample No. 25-59-1/11-81/23-53/64.	151
11	Scanning Electron Micrograph of Gd_2O_3 -Mo Sample No. 22-89/122-3. X12,100.	152

LIST OF ILLUSTRATIONS (Continued)

<u>Figure</u>	<u>Title</u>	<u>Page</u>
V-12	Predicted Effect of an Individual-Pin Series Resistance Upon Emission Current.	154
VI-1	Typical Geometry of a Planar Array of Conducting Metallic Pins Embedded In An Insulating Dielectric Substrate.	166
2	Uniform Pin Geometry for the Spheroidal Models.	167
3	Cross Sectional Geometry of the Exposed-Pin Emitting Device.	171
4	Cross Sectional Geometry of the Recessed-Pin Emitting Device.	174
5	Prolate Spheroidal Model; Single Pin Cross Section	177
6	Oblate Spheroidal Model; Single Pin Cross-Section	183
7	Graphs of the Modified Fowler-Nordheim Relation, Showing Field-Current Density J as a Function of the Applied Surface Electric Field E , for Several Values of the Work Function ϕ in ev, at a Temperature of 0°K .	193
8	Graphs of the Modified Fowler-Nordheim Relation, Showing Field-Current Density J as a Function of the Applied Surface Electric Field E , for Several Values of the Temperature T , for a Work Function of 4.5 ev.	194
9	Electric Field Intensity on the Pin Surface as a Function of v . Anode Voltage 10 kV; Anode Spacing $10 \mu\text{m}$; Pin Height $2 \mu\text{m}$; Pin Base Radius $1 \mu\text{m}$.	195
10	Current Density as a Function of v , Assuming a Constant Work Function of 4.5 eV, and a Constant Temperature of 293°K . Anode Voltage 10 kV; Spacing $10 \mu\text{m}$; Pin Height $2 \mu\text{m}$; Pin Base Radius $1 \mu\text{m}$.	197
11	Field Enhancement Factor as a Function of Pin Radius, with Pin Height as a Parameter.	200
12	Field Enhancement Factor as a Function of Pin Height with Pin Radius as a Parameter. Packing Density is $1 \times 10^6 \text{ Pins/cm}^2$.	201

LIST OF ILLUSTRATIONS (Continued)

<u>Figure</u>	<u>Title</u>	<u>Page</u>
VI-13	Field Enhancement Factor as a Function of Pin Radius with Pin Height as a Parameter.	202
14	Field Enhancement Factor as a Function of Pin Height with Pin Radius as a Parameter. Packing Density is 2×10^6 Pins/cm ² .	203

LIST OF TABLES

<u>Table</u>	<u>Title</u>	<u>Page</u>
II-I	THE RESULTS OF UO_2 - W COMPOSITE GROWTH EXPERIMENTS PERFORMED IN A N_2 - 10 v/o H_2 ATMOSPHERE	12
II	THE RESULTS OF UO_2 - W COMPOSITE GROWTH EXPERIMENTS PERFORMED IN A H_2 SATURATED WITH H_2O ATMOSPHERE	15
III	THE RESULTS OF UO_2 - W COMPOSITE GROWTH EXPERIMENTS PERFORMED IN CO - CO_2 ATMOSPHERES	18-19
IV	COMPOSITION PROFILES OF UO_2 - W COMPOSITES GROWN FROM A MIXTURE OF UO_2 2.04 AND 6 w/o W IN AN ATMOSPHERE OF CO - 1 v/o CO_2	22
V	SUMMARY OF COMPOSITE GROWTH IN THE RARE EARTH OXIDE-METAL SYSTEMS	28
VI	SUMMARY OF THE SOLIDIFICATION OF EXCESS METAL Gd_2O_3 (CeO_2) - Mo SAMPLES GROWN AT RAPID RATES TO TEST THE COUPLED GROWTH THEORY	38
IV-I	SUMMARY OF LOWEST OXIDE-METAL COMPOSITE RESISTIVITIES PRODUCED BY VARIOUS CONTACT METHODS	97
II	COMPOSITE MATRIX RESISTANCE MEASUREMENTS	99
III	MOLYBDENUM DEPOSITION RATES PRIOR TO MODIFICATION OF THE ION-BEAM COATER	104
V-I	CHRONOLOGICAL SUMMARY OF EMISSION EXPERIMENTS	124-123
II	COMPARISON OF EMISSION CAPABILITY OF SAMPLES HAVING SHORT AND LONG TUNGSTEN PINS	148
VI-I	VALUES OF THE FUNCTIONS $v(x)$ AND $t(x)$	191
VII-I	OXIDE-METAL SYSTEMS FORMING EUTECTIC STRUCTURES	206

FOREWARD

This research was supported by the Advanced Research Projects Agency of the Department of Defense and was monitored by the U. S. Army Missile Command under Contract Number DAAH01-71-C-1046.

"The views and conclusions contained in this document are those of the authors and should not be interpreted as necessarily representing the official policies, either expressed or implied, of the Advanced Research Projects Agency or the U. S. Government."

ABSTRACT

This research program was designed to develop melt-grown oxide-metal composite structures for high field electron emission testing. To meet these objectives the research program was divided into five areas: 1) Solidification Behavior of Oxide-Metal Mixtures, 2) The Formation of Optimum Emitting Arrays, 3) Oxide-Metal Composite Properties, 4) Experimental Emission Measurements, 5) Theoretical Analysis of Electron Emitting Arrays. A variety of refractory oxide-metal mixtures (i.e. UO_2 -W, stabilized ZrO_2 and HfO_2 -W, UO_2 -Ta, and the rare earth oxides of Gd_2O_3 , Nd_2O_3 and La_2O_3 -Mo and W) have been successfully induction melted and unidirectionally solidified to form aligned metallic fibers embedded in the oxide matrix. Composite structures containing between 5 and 70×10^6 fibers per cm^2 were obtained. Metal solubility in the molten oxides, control of the oxide stoichiometry and metal volatility were shown to be significant parameters controlling the successful composite growth in these systems. Chemical etching and annealing treatments were employed to form a variety of emitter geometries. Various materials were tested as brazes for use with the composite materials and pure Cu appeared to adequately wet both the oxide matrix and metal fibers, and provided good electrical contact between the emitter and cathode support structure. Emission measurements were performed with a variety

of unusual emitter geometries, including metallic coated samples and structures designed to operate at low voltages (< 100V). Several emitter samples have produced current densities above 500 ma/cm^2 . Long-term testing has extended to over 1000 hours for samples operating at a few ma/cm^2 . Analysis of post-emission damage and emission performance were used to assess the probable failure mechanism limiting the current density and life of the oxide-metal cathode structures. The theoretical analysis of emission employed a single-pin model with corrections introduced to account for the electric-flux-sharing produced when a multi-pin array is involved. Results from this model qualitatively predict the effects of pin density, pin height, and pin radius on the electron emission.

SECTION I

INTRODUCTION

This is the sixth and Final Report describing research performed on the "Melt-Grown Oxide-Metal Composites" Project, ARPA Order Number 1637, and also the Annual Technical Report for Contract DAAH01-71-C-1046, covering the report period 10 June 1971 through 31 December 1973. The information contained in this Report will emphasize work accomplished since the Semi-Annual Report¹, although some of the earlier information will be repeated to provide informational continuity. The Summary Section (Section VII) of this Report reviews the significant accomplishments of the entire oxide-metal composite research program, lasting three and one half years.

Previous reports^{2,4} contained a description of the modified internal floating zone technique employed during the growth of the oxide-metal composites. These materials typically contain many millions of less than 1 μm diameter metallic fibers per cm^2 uniformly embedded in an oxide (insulating or semi-conducting) matrix. A brief description of the growth technique will be included again, as it provides valuable background information for interpreting the various sections of this Report. In addition, it was the availability of the induction melted internal zone technique which made the growth of the refractory oxide-metal composite structures possible. The major research objectives in the different

project areas are also outlined in this section.

A modified floating-zone technique was used to grow oxide-metal composites. In this technique pressed rods of the oxide-metal mixture were sintered inside rf heated molybdenum tubes in an inert atmosphere to densify and preheat the material. A schematic diagram of the growth facility is shown in Figure I-1. After the initial heating, which also served to increase the electrical conductivity of the oxides, the molybdenum tube heaters were separated to expose approximately 2 cm of the rod to an rf field normally between 3 to 5 megahertz (Mhz). Often only a single Mo preheater was used, and in this configuration the Mo tube was simply lowered out of the coil to expose the sample to the rf field. The concurrent increase of temperature, electrical conductivity and resistance heating continued until the interior of the rod melted at temperatures up to 3000°C. The high radiant heat loss from the surface and the inherent low thermal conductivity of the oxides maintained the skin of the rod well below the eutectic temperature of the mixture. The solid skin acted as a crucible to contain the molten zone. Composite growth was obtained by moving the molten zone up through the rod. In practice a cavity was generated in the molten zone because of the difference in density between the initial polycrystalline rod and solidified composite. During growth the oxide and metal melted from the roof of this cavity and solidified at the base.

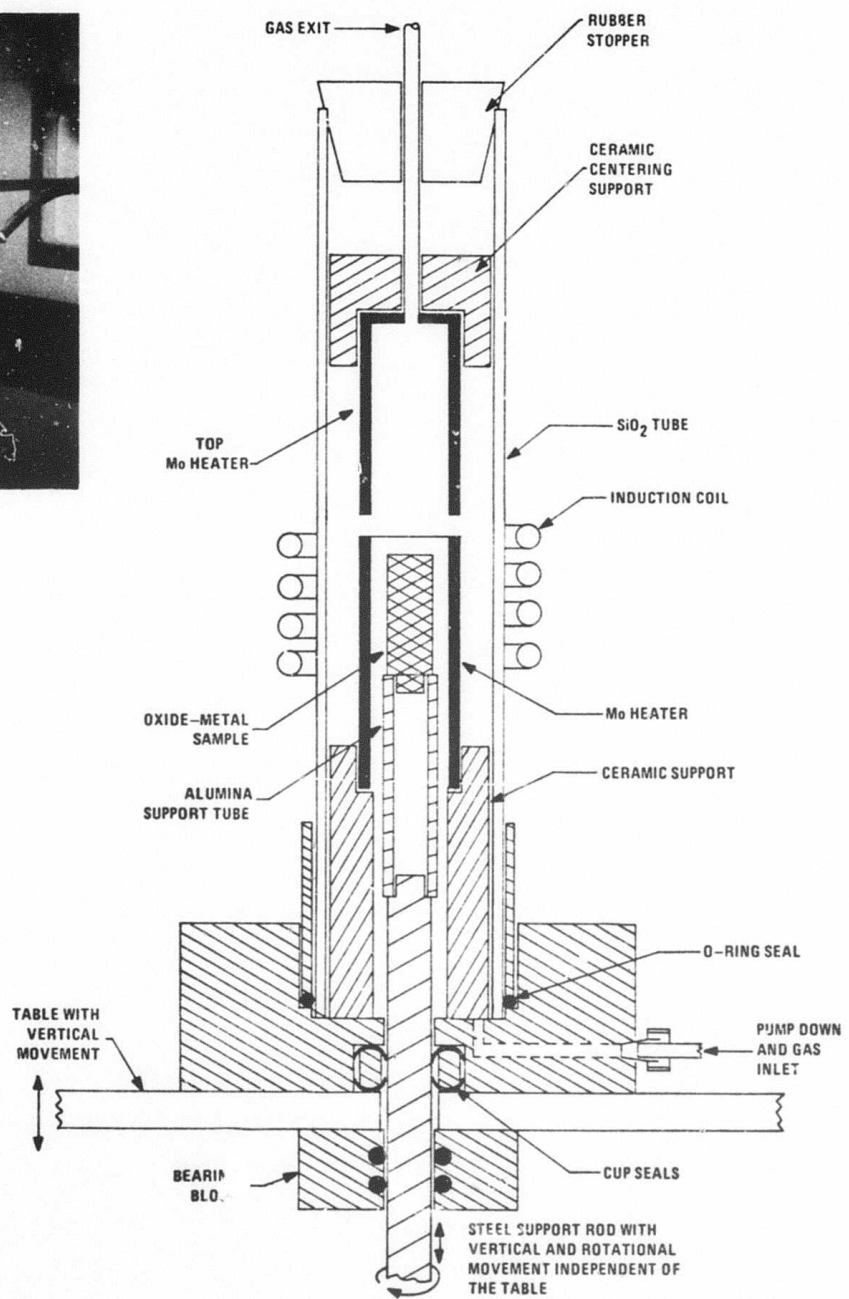
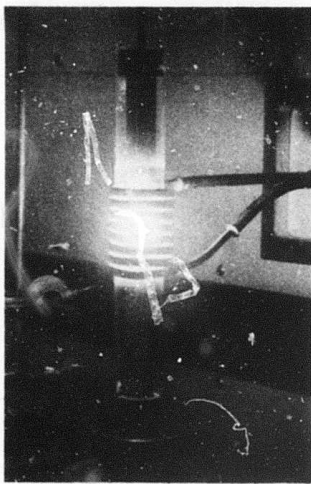


Figure I-1. Schematic Diagram of the Facility for the Growth of Oxide-Metal Composites.

The primary technical objective of this study was to understand the growth processes leading to coupled growth and ordered microstructures during the controlled solidification of refractory oxide-metal mixtures, and to successfully produce useable samples of these composites and evaluate their potential for electronic applications, with the major emphasis on high field electron emission. The research program was divided into five areas, and the objectives of these project areas and recent work in each area is briefly outlined below.

A. SOLIDIFICATION BEHAVIOR OF OXIDE-METAL MIXTURES

A study of the chemical, thermal, electrical and mechanical variables active during the solidification of numerous oxide-metal mixtures was employed to interpret and understand the parameters that control the successful growth of oxide-metal composites. Various techniques including doping, higher sample densification and higher preheat temperatures were used to increase the number of oxide-metal mixtures that could be internally melted by induction heating. Of fundamental importance were the factors which impart and control the metal solubility in the molten oxides. Oxides which possess variable stoichiometry appeared to dissolve the refractory metals more effectively than the compounds of fixed stoichiometry.

B. FORMATION OF OPTIMUM EMITTING ARRAYS

Selective chemical etching to expose, shape and remove the metallic pins from the oxide-metal composites were used to obtain structures of interest for electron emission testing. The development of sequential chemical etching and annealing treatments were employed to achieve a range of hemispherical pin tips sizes for UO_2 -W and CeO_2 doped Gd_2O_3 -Mo samples.

C. OXIDE-METAL COMPOSITE PROPERTIES

Work in this area was designed to explore the properties of these materials which are unique and potentially useful for applications. Emphasis was placed on electrical conductivity and the development of suitable brazing materials and procedures for use with the composite samples. Both front and back surface metallic coatings were also employed to achieve good electrical contact with the individual fibers.

D. EXPERIMENTAL EMISSION MEASUREMENTS

The electron emission performance of oxide-metal composites was evaluated as a function of pin array geometry and such electrical variables as field strength and inter-electrode spacing with the objective of obtaining the largest current density possible. Emission measurements were conducted under carefully controlled conditions so that the onset of

physical damage to the emitter structure could be determined. A variety of unusual emitter geometries, including metallic coated samples and structures designed to operate at low voltages (<100V), were tested. Several emitter samples have produced current densities above 0.5 A/cm^2 . Long term testing has extended to over 1000 hours for samples operating at a few ma/cm^2 . Analysis of post-emission damage and emission performance were used to assess the probable failure mechanism limiting the current density and life of the oxide-metal cathode structures.

E. THEORETICAL ANALYSIS OF ELECTRON EMITTING ARRAY

Initial theoretical efforts produced an approximate analytical solution for the electron emission valid in the neighborhood of the pin tips. Since the pin shape and periodic geometry precluded an exact solution, the analytical work was later supplemented by a numerical solution. The numerical methods, which could be made arbitrarily accurate, produced very good results for a single pin or arrays of several pins. However, capabilities of available computing facilities made many-pin solutions very difficult.

The latest study embodied a single-pin model with corrections introduced to account for the electric-flux-sharing produced when a multi-pin array is involved. Results from this model, and presented in this report, qualitatively predict the effects of pin density, pin height, and pin radius on the electron emission.

SECTION II

SOLIDIFICATION BEHAVIOR OF OXIDE-METAL MIXTURES

This section is subdivided into five major subsections:

A) Induction Coupling and Solidification Behavior of Oxide-Metal Systems, B) Variation of Eutectic Compositions with Growth Rate, C) Electron Beam Melting and Solidification of Oxide-Metal Systems, D) Possible Banding Mechanisms in Oxide-Metal Composites, and E) X-ray Analysis of Oxide-Metal Composites.

These subsections cover investigations designed to develop new oxide-metal systems that are capable of being internally melted by high frequency induction heating, development of techniques designed to grow oxide-metal composites suitable for high field electron emission testing, the determination of some of the parameters which control the successful growth of oxide-metal composites, and the initiation of research into the use of an electron-beam zone refiner to investigate oxide-metal systems that cannot be internally melted by direct induction heating.

A. INDUCTION COUPLING AND SOLIDIFICATION BEHAVIOR OF OXIDE-METAL MIXTURES

Melting and subsequent controlled solidification of refractory oxides and oxide-metal mixtures have been previously reported¹⁻⁵ using high (4 to 30 MHz) frequency rf heating. This technique is limited to systems that have sufficient electrical conductivity at elevated temperatures to support eddy current heating at the level required to produce internal melting.

Since the Annual Technical Report² (July 1972) a number of major accomplishments have been achieved in the ordered growth of metal fibers in oxide matrices. These include: 1) extensive ordered growth in the Gd_2O_3 - CeO_2 -Mo system and the fabrication of composite rods in this system up to 5 cm long; 2) the development of growth parameters designed to achieve "steady state" conditions during solidification in the UO_2 -W system; 3) the growth of ordered composites from the Y_2O_3 (CeO_2)-Mo and Y_2O_3 (CeO_2)-W systems; 4) the initial ordered oxide-metal composite growth in the CeO_2 -Mo system; 5) the calculation of the eutectic composition of the Y_2O_3 stabilized HfO_2 -W system, and determination that the eutectic composition for several of the oxide-metal systems varies with growth rate; and 6) the successful induction melting of two Al_2O_3 -based systems.

This subsection is subdivided into four areas based on the oxide matrix materials.

1. Stabilized ZrO_2 -W and HfO_2 -W
2. UO_2 -W
3. Rare Earth Oxide-Metal
4. $(\text{Al}_2\text{O}_3\text{-Cr}_2\text{O}_3)$ -W or Mo
5. Cr_2O_3 -Mo

1. Yttria Stabilized ZrO_2 -W and HfO_2 -W

Previous reports^{1,2} have described the influence of rf frequency, Y_2O_3 and W content, and growth rate on composite growth in Y_2O_3 stabilized ZrO_2 -W samples melted in N_2 - H_2 atmospheres. These samples (ZrO_2 - 10 m/o Y_2O_3) required

the addition of 16 w/o W to achieve the best eutectic growth and still contained areas of primary oxide.

Similar samples grown in a H_2 atmosphere required only about 6.5 w/o W to produce fibers throughout the entire solidified area. Calculation of the W content before and after growth in those samples solidified in H_2 indicated that very little W was lost from the rods by vaporization during growth. Samples previously solidified in N_2 - H_2 mixtures which initially contained 16 w/o W lost so much W by vaporization that the good growth areas contained only about 6 w/o W and the upper portions of the rod, which typically contained primary oxide areas, retained even less W.

An analysis of well ordered eutectic areas in a previously grown Y_2O_3 stabilized HfO_2 -W sample was made to estimate the eutectic composition in this system. The sample composed of HfO_2 with 10 m/o Y_2O_3 and initially 12.3 w/o W was found to contain only 2.5 w/o W in the final eutectic structure. This is a reasonable eutectic composition for Y_2O_3 stabilized HfO_2 and W. This composition was determined by measuring fiber diameters and counting fiber densities on SEM micrographs and then using 9.75 and 19.27 gm/cm^3 as the theoretical densities of HfO_2 stabilized with 10 m/o Y_2O_3 ⁶ and tungsten respectively to convert from volume percent to weight percent tungsten. The tungsten content in the molten zone apparently decreased

throughout the growth process by vaporization of W, W_2 and W_3 which were detected in vapor coatings deposited on the quartz atmosphere containment tube.

2. UO_2 -W

In previous reports,^{1,2,3} the importance of the stoichiometry of uranium dioxide on composite growth in the system UO_2 -W was reviewed. The influence of the O/U ratio on the sintering and rf coupling characteristics and on the melting and solidification behavior of the UO_2 -W samples were described in detail. Special emphasis was placed on the role of the O/U ratio on the solubility of tungsten in molten UO_2 . During the present report period, work in this system continued on approaches designed to achieve "steady state" growth condition. In many of the solidification experiments the entire length of the interior of the UO_2 -W rod was melted with the intent of maintaining a constant temperature and a uniform concentration of W dissolved in the molten oxide. To achieve these conditions the oxide-metal rod was exposed to the rf field (by removing the molybdenum pre- and post-heaters from the rf coil), and the unmelted skin acted as a crucible to contain a two to three centimeter long molten zone. The sample was lowered in various atmospheres designed to keep the stoichiometry of the melt above 2.00⁷. In the following discussions, the growth

of UO_2 -W composites in an atmosphere of $\text{N}_2\text{-H}_2$ is reviewed and recent experiments designed to increase the oxygen potential in the growth atmosphere using $\text{H}_2\text{O/H}_2$ and $\text{CO}_2\text{/CO}$ gas mixtures are reported. Lastly, the status of composite growth in the system UO_2 -W is presented.

Most of the early composite growth in the system UO_2 -W was performed using powders with an O/U ratio above 2.10 and melting and solidification was accomplished in a $\text{N}_2\text{-H}_2$ atmosphere, typically containing approximately 10 v/o H_2 , using molybdenum pre-and post-heaters. Table II-I reviews the series of experiments performed since the last Annual Report², employing the $\text{N}_2\text{-H}_2$ gas mixture and Mo heaters, designed to assess the influence of various starting O/U ratio powders on composite growth in the system UO_2 -W. Some general observations can be obtained from the data in Table II-I. Using an oxide powder with an O/U ratio of 2.03 and melting in the $\text{N}_2\text{-H}_2$ atmosphere apparently resulted in an oxide-metal system where the O/U ratio of the melt was below that required to maintain the necessary tungsten solubility for ordered growth (Table II-I, experiments Numbers 3-29 to 13-64). The majority of the metal usually appeared as undissolved droplets dispersed in the oxide. By increasing the O/U ratio of the powder to 2.1⁴ and above the growth of well-ordered composite materials occurred during the initial period of solidification. However, as growth proceeded in the $\text{N}_2\text{-H}_2$ atmosphere kinetic processes

TABLE II-I

THE RESULTS OF UO_2 - W COMPOSITE GROWTH EXPERIMENTSPERFORMED IN A N_2 - 10 v/o H_2 ATMOSPHERE

<u>Experiment Number</u>	<u>Starting O/U Ratio</u>	<u>w/o W</u>	<u>Growth Rate, cm/hr</u>	<u>Composite Growth Description</u>
3-29	2.03	6.0	6.0	
3-29a	2.03	7.7	3.1	
13-63	2.03	5.0	-	
13-64	2.03	3.3	2.4	
25-30	2.14	10	1.9	Growth very good at base, banded in middle and fair at top of zone.
25-32	2.14	10	1.8	Good growth for about 8 mm, thin cells but long and continuous growth
25-39	2.14	10	1.9	10 mm of solidified zone with badly banded fibers. W droplets in the bands, short thin cells.
25-43	2.16	10	1.9	6 mm of solidified zone with badly banded fibers. W droplets in bands.
25-45	2.16	10	1.9	Badly banded with W droplets
25-47	2.16	9	2.16	Badly banded with W droplets
25-51	2.16	9	2.0	7 mm of solidified zone but fibers the entire length of zone. Moderate banding and thin cells.

* In these experiments heated ($\sim 1400^\circ C$) Mo pre-and post-heaters were used (as shown in Figure I-1).

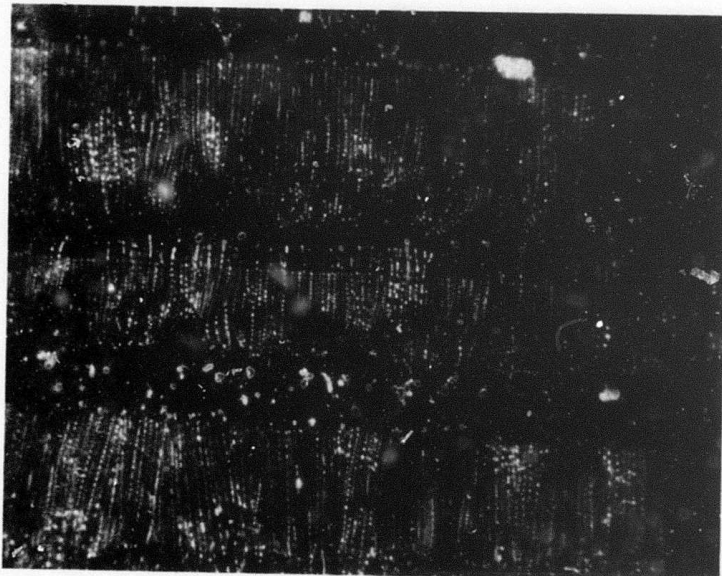
reduced the O/U ratio of the oxide, and vaporization of W and W oxides, etc., continued and resulted in limited metal solubility in the top portion of the UO_2 -W samples (Table II-I, Experiments Numbers 25-30 to 25-51). Figures II-1a and b are typical of the oxide bands and W droplets formed in UO_2 -W samples solidified in the N_2 - H_2 atmosphere. As a result of the UO_2 -W solidification experiments performed with different starting O/U ratio powders and listed in Table II-I it was aptly demonstrated that the tungsten solubility was dependent on the stoichiometry maintained in the liquid oxide.

Approximately a year and one-half ago an effort to minimize the major variations of temperatures and compositions during the solidifications of UO_2 -W samples was initiated. As noted in the introduction to this section, this approach was designed to achieve "steady state" conditions by melting and maintaining a long (several centimeter) molten zone. Composite growth was accomplished in $\text{H}_2\text{O}/\text{H}_2$ or CO_2/CO atmospheres where oxygen was available to maintain the stoichiometry of the molten oxide at or above 2.00⁷.

A series of UO_2 -W solidification experiments performed in a H_2 atmosphere saturated with H_2O ($\sim 20,000$ ppm H_2O) are listed in Table II-II. Most of these composite experiments were run with the long molten zone without any heated Mo in the system. The pre-and post-heaters were removed to prevent the reaction between the Mo and H_2O resulting in a reduction of the oxygen potential available to the UO_2 -W samples.



a) Bright Field,
X600.



b) Dark Field,
X600

Figure II-1. Degeneration of Uniform Composite Structure because of Reduced W Solubility in Molten UO_2 .

TABLE II-II

THE RESULTS OF UO_2 - W COMPOSITE GROWTH EXPERIMENTSPERFORMED IN A H_2 SATURATED WITH H_2O ATMOSPHERE

Experiment Number	Initial O/U Ratio	w/o W	General Growth Description	Length of Good Composite Growth
31-13	2.06	6	Generally good, fan banding in middle of zone	
31-23	2.04	6	Good growth from very bottom of molten zone	11 mm
31-25	2.043	8	Very poor	
31-28	2.034	6 $\frac{1}{2}$	Fibers slow to start, excess W at base	7 mm
31-29*	2.04	6	Excess W at base, good growth low in pellet	
31-34	2.035	6 $\frac{1}{2}$	Good	12 mm
31-39**	2.035	6 $\frac{1}{2}$	Good, primary oxide at base	
31-42**	2.019	6 $\frac{1}{2}$	Very poor, large W blobs entire length of sample	
31-44**	2.035	6 $\frac{1}{2}$	Good, primary oxide at base	12 mm
31-46	2.035	6 $\frac{1}{2}$	Good growth from base	8 mm
31-50***	2.035	6 $\frac{1}{2}$	Good growth, base has layer of oxide with W needles	18 mm

* Test of ceria doping. Composition: 84.6 w/o UO_2 , 9.4 w/o CeO_2 and 6.0 w/o W.

** A platinum tube was employed as post-heater ($\sim 1400^\circ C$) to reduce thermal gradients during cooling.

*** Atmosphere was diluted with approximately 50 v/o N_2 .

In general, the UO_2 -W growth experiments performed in an atmosphere of H_2 saturated with H_2O yielded 0.5 to 1.0 cm of good composite growth at the base of the sample followed by an upper region of apparent low oxide stoichiometry and insufficient W solubility. This behavior is similar to that observed with the experiments performed in the N_2 - H_2 atmosphere and reported in Table II-I. (Note that the runs reported in Table II-II used oxide powders with O/U ratios of about 2.04 with 6 w/o W.)

Several items of special note in Table II-II include Experiment Numbers 31-39, 31-42 and 31-44 where a platinum tube was employed as a post-heater. The platinum was substituted for the Mo tube to prevent the Mo reaction with the H_2O and the depletion of this gas from the growth atmosphere. Unfortunately, the surface temperature of the UO_2 -W samples was too high and the platinum melted as the heated sample was lowered into the tube. Experiment Number 31-50 was also noteworthy because it indicated that diluting the H_2O/H_2 gas with inert N_2 resulted in an approximately 50% increase in the usable length of uniform UO_2 -W composite growth. In general, the data from Table II-II indicated there was a continual reduction of the O/U ratio of the oxide during composite growth in the H_2O/H_2 atmosphere and, consequently, CO_2/CO gas mixtures were considered as means of further increasing the oxygen potential in the UO_2 -W growth atmosphere.

A tabulation of the UO_2 -W runs performed in CO_2 /CO gas mixtures is listed in Table II-III. The majority of the UO_2 -W runs performed in the CO_2 /CO atmospheres were also accomplished without the Mo pre-and post-heaters and with the long (several centimeter) molten zone. A significant result of this series of experiments was the generally poor or complete lack of composite growth obtained in Experiment Numbers 25-71, 25-90,-92,-94, 31-8 utilizing 4 to 5 v/o CO_2 . Apparently this gas mixture ($\text{CO} + 4$ v/o CO_2) sets an upper limit of the usable oxygen potential for composite growth in the system UO_2 -W. The reactions that eliminated eutectic growth under these conditions are unknown, although excessive vaporization of W as WO_2 or WO_3 undoubtedly was a major contribution to this behavior, since the resultant oxide-metal structure was almost depleted of W. Figure II-2 shows the distinct UO_2 -W microstructure found in large areas of the UO_2 -W samples grown in the CO -4 v/o CO_2 atmosphere. Similar structures have been observed in ZrO_2 -W and HfO_2 -W samples previously.³ Another significant result of the series of CO_2 /CO experiments was the excellent reproducibility between UO_2 -W samples consecutively grown in the CO -1 v/o CO_2 atmosphere. This behavior suggested the initial comparative study of the composition profiles along the length of composite growth of several samples. Four of the better UO_2 -W samples were cut in wafers approximately 60 mils thick and the wafers were

TABLE II-III

THE RESULTS OF UO_2 - W COMPOSITE GROWTH EXPERIMENTS
 PERFORMED IN CO - CO_2 ATMOSPHERES

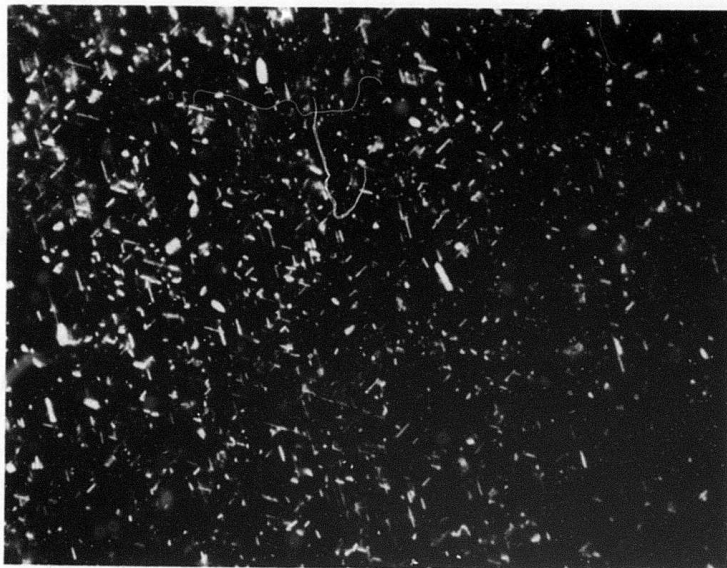
<u>Experiment Number</u>	<u>Initial O/U Ratio</u>	<u>w/o W</u>	<u>v/o CO_2</u>	<u>Growth Rate, cm/hr</u>	<u>Description of Growth</u>	<u>Length of Good Growth</u>
113-17	2.04	6	0.3	3.6	Good (1)	2 cm
113-20	2.04	8	1.0	7.2	Good (1) Excess at top	1 cm
25-49	2.04	6	0.3	1.7	Good, low fiber density, thick walls	-
25-53	2.04	6	0.3	2.1	Good growth	-
25-55	2.16	6	0.3	1.9	Very poor, banding and primary oxide	-
25-57	2.04	6	1.0	3.14	Good growth	-
25-59	2.04	6	1.0	3.44	Very good (2)	2.5 cm
25-61	2.04	6	1.0	3.4	Very good (2)	2.0 cm
25-64	2.04	6	1.0	3.4	Very poor, No W solubility	-
25-66	2.04	6	1.0	4.1	Good (2)	1.5 cm
25-69	2.04	6	1.0	5.65	Good (2)	1.5 cm
25-71	2.12	6	4.5	3.4	Very poor W platelets and fan banding	-
25-72	2.12	6	1.0	3.4	Short length of good growth at base (1)	-
25-73	2.12	6	1.0	2.4	Short length of good growth at base (1)	-

TABLE II-III (continued)

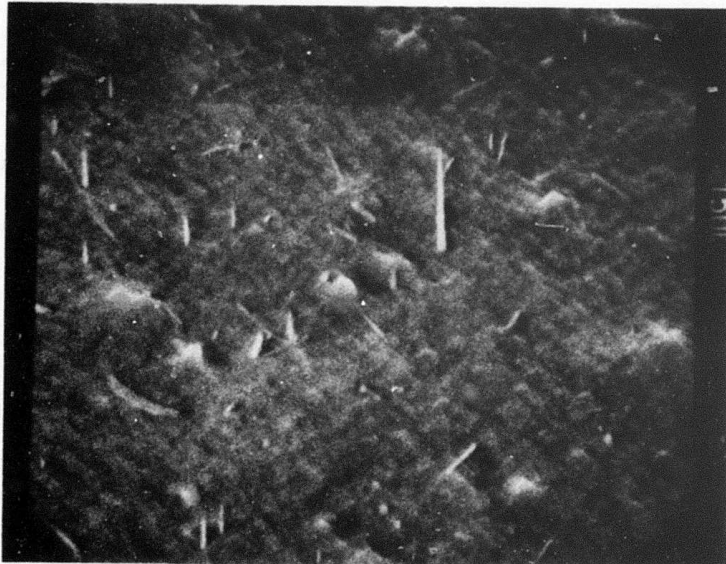
<u>Experiment Number</u>	<u>Initial O/U Ratio</u>	<u>w/o W</u>	<u>v/o CO₂</u>	<u>Growth Rate, cm/hr</u>	<u>Description of Growth</u>	<u>Length of Good Growth</u>
25-77	2.049	6	1.0	3.4	Good (1)	1.0 cm
25-81	2.049	6	1.0	3.4	Good (1)	1.5 cm
25-85	2.04	4	1.0	3.4	Larger cells, short area at base with no W (1)	0.9 cm
25-88	2.05	4	1.0	3.1	Large cells	1.0 cm
25-90	2.05	4	4.3	3.1	Very bad, random W platelets	-
25-92	2.11	10	4.3	3.1	Good, primary oxide at top (1)	0.6 cm
25-94	2.18	10	4.3	3.1	Very poor, primary oxide (1)	-
31-8	2.04	6	5.0	3.1	Very short fiber zone, mostly large area without W (3)	-

Notes:

- (1) The upper portion of the solidified zone in these samples contained poor growth containing "fan banding" with W droplets in the oxide bands.
- (2) See Table II-IV for data on fiber diameters, density and w/o W in these samples.
- (3) Slow cooling was accomplished with a Mo post-heater which reacted with the CO₂/CO atmosphere.



a) Dark Field,
X600



b) Scanning Electron
Micrograph after
 UO_2 selectively
removed to expose
the W Needles,
X10,000.

Figure II-2. Microstructure of UO_2 -W Samples Solidified in
 $CO + 4$ v/o CO_2 Showing Fine W Needles and Platelets.

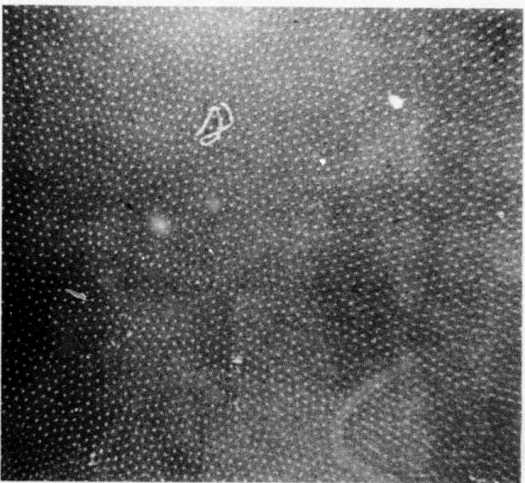
numbered starting at the base of the composite growth. Table II-IV shows the fiber density, diameter and weight % W which was determined from SEM micrographs of selected wafers. An error analysis on the calculations involved in obtaining these figures indicated errors of $\pm 10\%$ in both fiber diameter and density and an error of $\pm 30\%$ in the weight % W. Based on this limited data (only three sections per sample) three of the UO_2 -W composite rods showed wide variations in the fiber size and density; however, the examination of Sample No. 25-59 indicated, in principle at least, that 2 cm or longer UO_2 -W composite rods with differences of $\pm 3\%$ in fiber diameter and $\pm 12\%$ in fiber density are feasible. Eutectic growth typical of the UO_2 -W samples grown in the 1 v/o CO_2 starting with a mixture of $\text{UO}_{2.04}$ and 6 w/o W is shown in Figure II-3.

The major consideration for successful and extensive oxide-metal composite growth in any system, and especially with UO_2 -W mixtures, is the necessity of obtaining and maintaining a homogeneous oxide-metal liquid. In earlier reports^{1,2,3} the importance of the O/U ratio on sintering, rf coupling behavior and low temperature oxidation problems was described. This brief summary reviews the problems associated with maintaining W solubility in molten UO_2 at temperatures of 2700-2800°C, and the general status of composite growth in the system UO_2 -W.

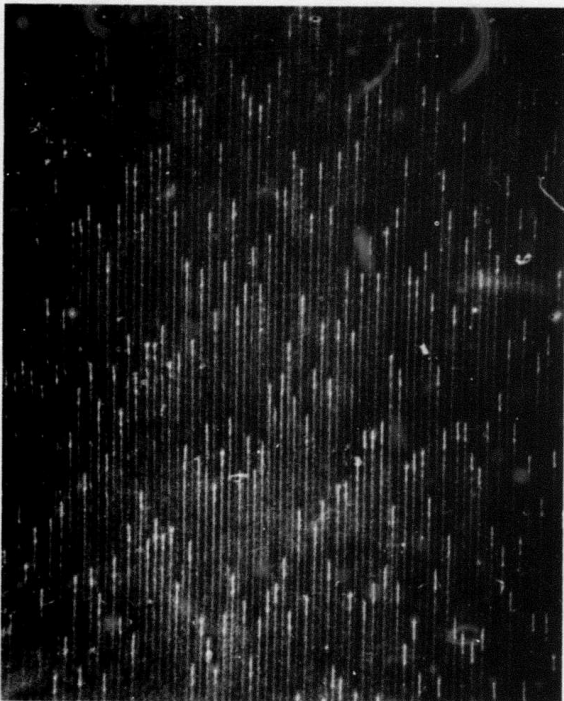
TABLE II-IV

COMPOSITION PROFILES OF UO_2 - W COMPOSITES
 GROWN FROM A MIXTURE OF $UO_{2.04}$ AND 6 w/o W
 IN AN ATMOSPHERE OF CO - 1 v/o CO_2

<u>Experiment Number</u>	<u>Wafer Number</u>	<u>Lowering Rate, cm/hr</u>	<u>Fiber Diameter, Microns</u>	<u>Density, Fibers/cm²</u>	<u>w/o W</u>
25-59	1	3.44	0.45	8.0×10^6	2.2
25-59	5	3.44	0.47	8.6×10^6	2.6
25-59	10	3.44	0.45	6.8×10^6	1.9
25-61	2	3.40	0.40	11.9×10^6	2.6
25-61	4	3.40	0.49	8.9×10^6	2.9
25-61	6	3.40	0.41	19.8×10^6	4.6
25-66	3	4.10	0.35	11.7×10^6	2.0
25-66	5	4.10	0.41	10.8×10^6	2.5
25-66	7	4.10	0.50	10.4×10^6	3.6
25-69	3	5.65	0.34	10.5×10^6	1.9
25-69	5	5.65	0.28	17.8×10^6	1.9
25-69	7	5.65	0.32	19.0×10^6	2.6



a) Transverse Section,
Bright Field, X480.



b) Longitudinal Section,
Dark Field, X600.

Figure II-3. Uniform and Continuous UO_2 -W Composite Structures
in Samples Solidified in CO + 1 v/o CO_2 .

It has been well documented in this and previous reports^{1,2,3} that the solidified oxide-metal composites typically contain significantly less metal than originally used in the initial starting mixture. Consequently, any growth scheme must face the continual depletion of the metal from the molten zone predominantly through vaporization losses (especially in the systems with high eutectic temperatures, i.e. UO_2 -W, ZrO_2 -W). In the case of UO_2 -W this behavior is further complicated by the need to maintain the stoichiometry of the molten oxide at or above 2.00 (using high starting O/U ratio powders, WO_3 additions, or with H_2O or CO_2 additions to the growth atmosphere) to maintain solubility of W in the molten oxide. Obviously, any increased oxygen potential in the system only aggravates the W oxidation and the UO_2 and W vaporization problems.

The modification of the growth procedures to achieve "steady-state" conditions and minimize temperature and compositional variations has proved moderately successful and led to reproducible UO_2 -W composite structures.

Unfortunately, this approach requires maintaining the entire length of the oxide-metal rod at $2700-2800^{\circ}C$ and, consequently, the oxidation and vaporization reactions are proceeding rapidly under these conditions, and the growth of UO_2 -W composite samples with uniform structures longer than 2 cm has proved difficult.

In the previous report¹ the prospect of varying the metal content of the oxide-metal liquid using controlled stoichiometry was discussed. Unfortunately, a much better understanding of the high-temperature chemistry of the molten oxide-metal system is needed before this control can be exercised over the growth of UO_2 -W eutectic structures.

Some general comments about growing "crack-free" UO_2 -W samples are also pertinent. In the early UO_2 -W runs made with molybdenum pre- and post-heaters shown schematically in Figure I-1, numerous crack-free samples were obtained because this geometry greatly reduced the thermal gradient the sample was subjected to during cooling. In most of the controlled atmosphere experiments described in this report (Tables II-II and II-III) the molybdenum was removed from the system to simplify interpreting the experimental variables, and the resulting temperature gradient typically produced cracked samples. At present it is not certain whether using inert refractory tubes (Ir or Re) to replace the molybdenum and growing in the CO_2/CO atmosphere or returning to the molybdenum pre- and post-heaters and utilizing high O/U ratio powders in a $\text{N}_2\text{-H}_2$ gas mixture will yield the best eutectic structures.

In summary, oxide-metal composite growth in the system UO_2 -W has progressed to the point where samples 10 to 12 mm in diameter and 20 mm long can be routinely produced. Composite

geometries containing between 10 and 30×10^6 ordered metal fibers/cm² are available. The parameters associated with induction melting and the mechanics of solidification have been fairly well optimized. The high temperature chemistry of the UO_2 -W system needs more study, both from an equilibrium viewpoint as well as the kinetic considerations associated with the unidirectional solidification process.

3. Rare Earth Oxide-Metal Systems

During the past two years unidirectionally solidified rare earth oxide-metal eutectics have been developed into a promising class of oxide-metal composites. Some of the reasons the rare earth oxide composites are attractive can be summarized as follows: a) they are stable materials (excepting pure CeO_2) which can be melted in H_2 atmospheres without major stoichiometry changes; b) they form easily controlled molten zones which allow a wide latitude of power settings between solidification and excessive melting; c) these oxides withstand the severe thermal gradients present in the zone melting technique very well and yield crack-free samples; d) large samples 4 to 5 cm long with good fiber continuity can be routinely grown. One major disadvantage, however, is that the grown fiber arrays are not as uniform in both diameter and spacing as the other oxide-metal systems.

As reported in a previous report,² ordered eutectic structures have been achieved using Mo or W in conjunction with Gd_2O_3 , La_2O_3 and Nd_2O_3 . The best composites were grown from these systems when the metal solubility was increased by the addition of ceria. During this report period work has been concentrated on the Gd_2O_3 - CeO_2 -metal system to avoid the hydration problems associated with La_2O_3 and Nd_2O_3 . In addition, the use of CeO_2 , Sm_2O_3 , Y_2O_3 , Eu_2O_3 , and Ho_2O_3 as matrix materials has also been investigated.

A summary of the rare earth oxide-metal systems investigated to date is presented in Table II-V.

a) Gd_2O_3 - CeO_2 -Mo

The variation of fiber density and fiber diameter versus growth rate has been determined for the Gd_2O_3 -20 w/o CeO_2 -10 w/o Mo composition. Fiber density versus growth rate varied in a near linear manner as shown in Figure II-4 for growth rates between 0.75 and 4.8 cm/hr. However, the parabolic equation

$$Y = 0.822 + 11.9X - 0.741 X^2$$

where Y is the fiber density per cm^2 in millions and X is the growth rate in cm/hr had a higher correlation coefficient (0.966) and a lower standard error of estimate (2.61×10^{-6} fibers/ cm^2) than did the best linear fit for these data points.

TABLE II-V
SUMMARY OF COMPOSITE GROWTH IN THE
RARE EARTH OXIDE-METAL SYSTEMS

Oxide	Metal	Description of Composites		
Nd_2O_3	Mo W Nb Ta	Poor Fiber Continuity Poor Fiber Continuity Unstable Zone Unstable Zone		Slowly Hydrates
$\text{Nd}_2\text{O}_3(\text{CeO}_2)$	Mo W Fe Ni Co	Good Fibers Good Fibers No Fibers, Unstable Zone No Fibers, Unstable Zone No Fibers, Unstable Zone		Matrix Slowly Hydrates
La_2O_3	Mo W	Poor Fiber Continuity Poor Fiber Continuity		Matrix Rapidly Hydrates
$\text{La}_2\text{O}_3(\text{CeO}_2)$	Mo W	Good Fibers Good Fibers	Matrix	Rapidly Hydrates
$\text{Eu}_2\text{O}_3(\text{CeO}_2)$	Mo	Good Fibers		
$\text{Ho}_2\text{O}_3(\text{CeO}_2)$	Mo	Good Fibers		
CeO_2	Mo W Ni	Good Fibers Good Fibers No Fibers	Structure Dependent On Oxide Stoichiometry	
Gd_2O_3	Mo	Did Not Couple		
$\text{Gd}_2\text{O}_3(\text{CeO}_2)$	Mo W Cu Rh	Good Fibers, No Hydration Good Fibers, Zone Unstable No Fibers No Fibers		
Dy_2O_3	Mo	Did Not Couple, Possible Phase Change		
Sm_2O_3	W	Did Not Couple, Slowly Hydrates		
$\text{Y}_2\text{O}_3(\text{CeO}_2)$	Mo W	Good Fibers Platelets		

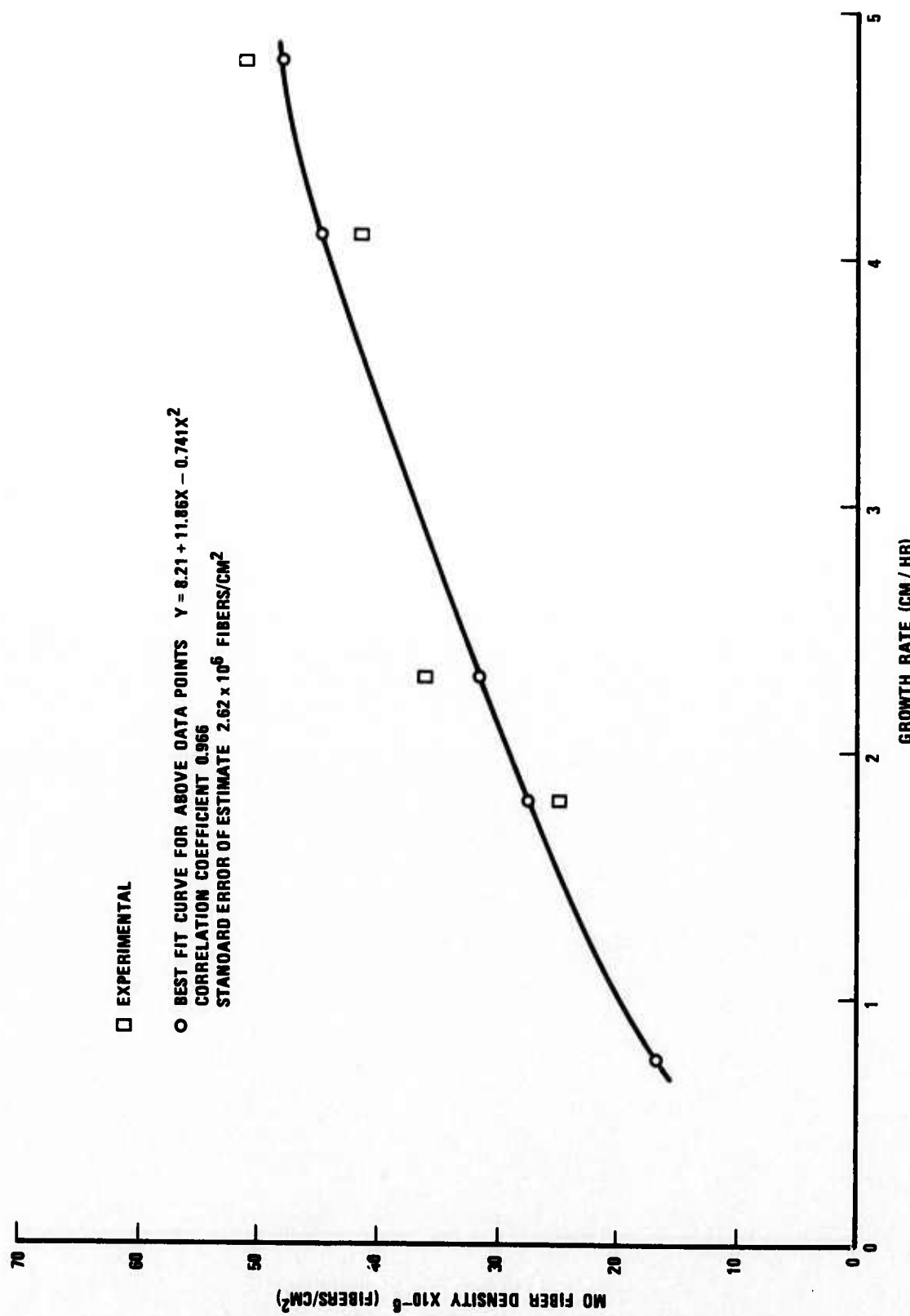


Figure II-4. Effect of Growth Rate on Molybdenum Fiber Density in $\text{Gd}_2\text{O}_3\text{-CeO}_2\text{-Mo}$ Composites.

The relationship between fiber diameter and growth rate is also parabolic in nature and is described by the equation

$$Y = 0.966 - 0.376X + 0.045X^2$$

where Y is the fiber diameter in microns and X is the growth rate in cm/hr. The correlation coefficient for this equation was 0.990, and its standard error of estimate was 0.031 μm .

Metal morphology and cell size versus growth rate and cell size versus growth length have been qualitatively determined in the Gd_2O_3 -Mo system. The number and size of platelets decreased significantly as the growth rate was increased. However, samples grown at rates of 3.5 cm/hr and greater exhibited areas of disordered growth (similar to those observed in samples where the molten zone spontaneously traveled to the top of the pellet), and these disordered areas increased in size as the growth rate increased. A sample grown at 5 cm/hr had this disordered morphology (see Figure II-5) throughout the entire solidified zone.

Figure II-6 shows the typical microstructure of a Gd_2O_3 -Mo sample grown at 4 cm/hr. Platelets are only present at cell boundaries, and no cell contains only platelets. However, when the growth rate was reduced to 2 cm/hr (see Figure II-7), some cells contained almost entirely platelets and most cells contained a few platelets in their interiors. Cell size appeared to increase with growth length and decrease with increasing rate of growth.

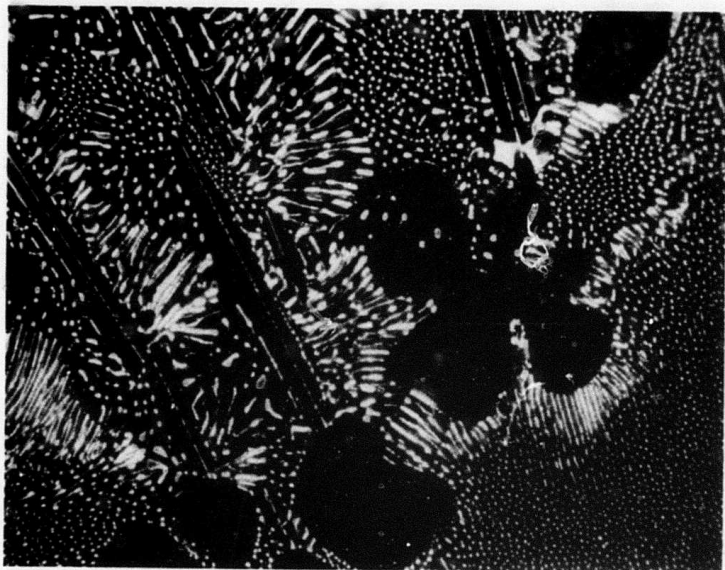


Figure II-5. Disordered Composite Morphology
of CeO_2 Doped Gd_2O_3 -Mo Sample
Grown at 5 cm/hr. Dark Field,
x600.



Figure II-6. CeO₂ Doped Gd₂O₃-Mo Sample Grown at 4 cm/hr Displaying Mo Fibers in the Cell Interior Which Gradually Grade to Platelets at the Cell Boundary. Dark Field, X600.

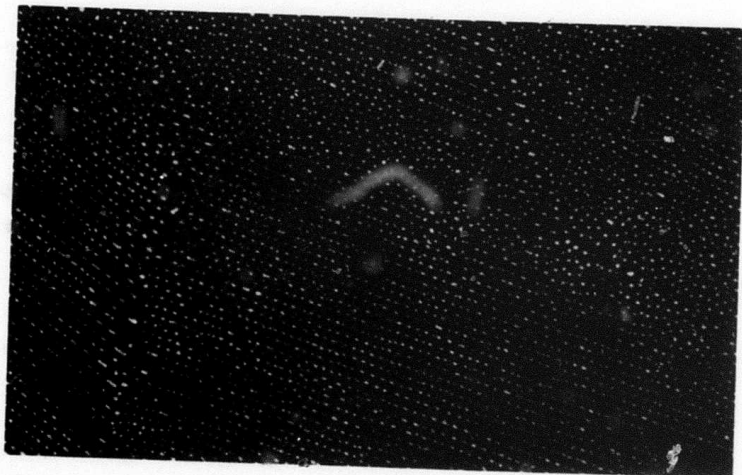


Figure II-7. CeO₂ Doped Gd₂O₃-Mo Sample Grown at 2 cm/hr Showing Cells Essentially Composed of Narrow Mo Platelets. Dark Field, X800.

The advantages of growing longer samples include larger cell size and more uniform growth the longer the length of the solidified zone since the more preferentially orientated cells will tend to predominate, and initial melt inhomogeneities will tend to be damped out. It was felt that the high sintered density of the rare earth samples would permit the growth of composites up to 15 cm in length, since the void size (a factor limiting growth in other systems) would not be a problem.

The use of thick-walled rubber molds and isopressing techniques allowed long uniformly dense green rods to be produced. Using these rods, unidirectionally solidified lengths from 4 to 5 cm long were easily produced (see Figure II-8). Even longer samples could be produced if the growth-lowering apparatus had a greater stroke length.

Examination of cross sections taken at increasing distances from the base of the solidified zone showed that platelet size and density increased with increasing growth length. Oxide-metal composite structures typical of this behavior are shown for a Nd_2O_3 (CeO_2) - Mo sample (see Figure II-10).

Various schemes were tried in an attempt to eliminate the platelets and produce more uniform fiber arrays. Small changes in composition were tried, such as lowering the CeO_2 content and metal content, but no improvement was observed.

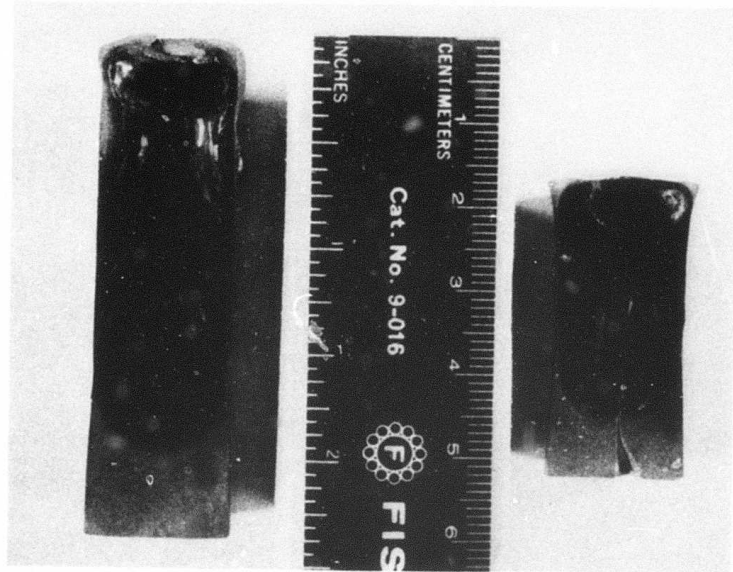


Figure II-8. Comparison of the Size of CeO_2 Doped Gd_2O_3 -Mo Composite Samples Initially Prepared by Uniaxial Pressing in a Steel Die (Right Pellet) and Iso-Pressing in a Rubber Mold (Left Rod).

TiO_2 and Pr_6O_{11} were substituted for CeO_2 in hopes they would act similarly but would reduce the metal solubility slightly. Neither sample melted, and both showed poor thermal shock characteristics.

Impurities were added in trace amounts in hopes they would preferentially concentrate at the metal growth front causing the metal solidification front to coincide with (or lag slightly behind) the oxide solidification front. Traces of Ni and As were tried but no difference in fiber structure was observed.

As has been previously reported, as the growth rate was increased a disordered area in the center of the rod appeared in CeO_2 doped Gd_2O_3 -Mo samples grown at about 3.5 cm/hr. This region increased as the growth rate was further increased until at about 5 cm/hr it encompassed the entire rod (see Figure II-5). The disordered area consisted of oxide dendrites embedded in a matrix of eutectic material. This phenomena could be explained by the existence of a coupled region similar to that proposed by Hogan⁸ for metal-metal systems. Hogan states that there is a range of compositions over which normal eutectic growth can be obtained if there is sufficient undercooling of the liquid. At zero growth rate, i.e equilibrium, there is only one composition, the eutectic composition, which will produce coupled growth. But if the growth rate is increased, thus

increasing undercooling, a range of compositions can be solidified into normal composites. On a conventional phase diagram this region can be thought of as a metastable region spreading out from the eutectic below the solidus line. If the two phases have different melting temperatures, the coupled region will be skewed toward the higher melting phase. A proposed pseudo-binary phase diagram is shown in Figure II-9, and, for a selected composition "A", as the growth rate (undercooling) is increased the structure will pass through three stages. First, at very slow rates metal dendrites and eutectic regions will be observed; second, at moderate growth rates, the composition will be entirely in the coupled region and good composite growth will occur. Lastly, as the growth rate is increased, the composition will be out of the coupled region requiring oxide dendrites to precipitate in the disordered region to bring the composition back into the coupled zone. As the growth rate is increased further, more primary oxide must precipitate in order to bring the composition into the coupled region and the disordered area increases until it encompasses the entire growth area. If, however, the composition is moved to B (Figure II-9), further toward the metal rich side, this composition will remain in the coupled zone at greater undercoolings without oxide precipitation. Table II-VI summarizes experiments run at high growth rates with excess metal in an effort to

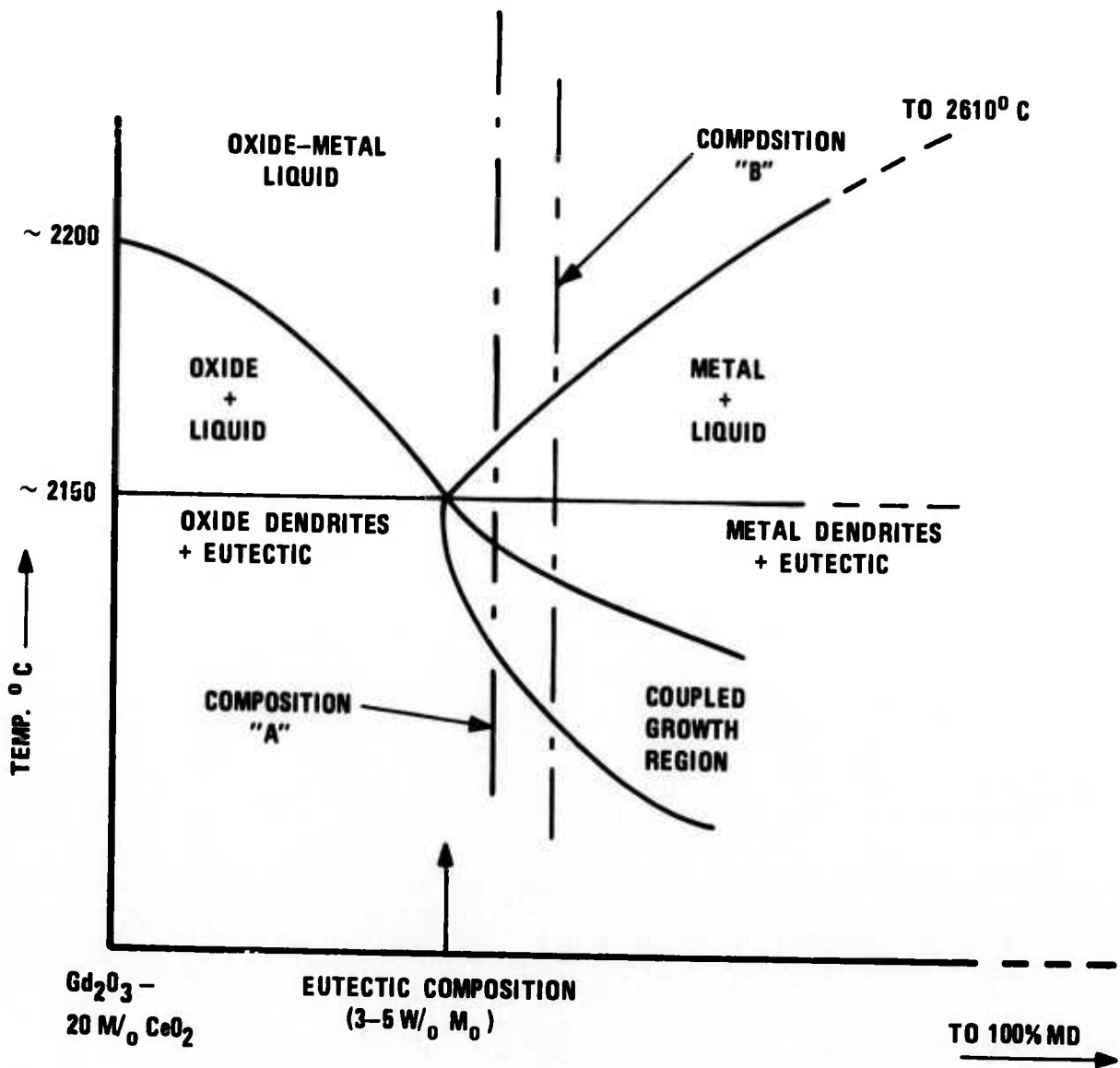


Figure II-9. Proposed Phase Diagram for the System CeO_2 Doped Gd_2O_3 -Mo Including Non-Equilibrium Subsolidus Region of Eutectic Growth.

TABLE II-VI

SUMMARY OF THE SOLIDIFICATION OF EXCESS METAL
 $\text{Gd}_2\text{O}_3(\text{CeO}_2)$ -Mo SAMPLES GROWN AT RAPID RATES
 TO TEST THE COUPLED GROWTH THEORY

Composition Weight %	Growth Rate Cm/Hr	Comments
Gd_2O_3 20% CeO_2 12% Mo	10	Oxide Dendrites + Eutectic Very Little Excess Mo
Gd_2O_3 20% CeO_2 12% Mo	6	Oxide Dendrites + Eutectic Very Little Excess Mo
Gd_2O_3 15% CeO_2 15% Mo	8.2	Oxide Dendrites Some Fiber Areas Near Metal Blobs
Gd_2O_3 20% CeO_2 12% Mo	4.3	Good Uniform Growth
Gd_2O_3 20% CeO_2 14% Mo	6.4	Oxide Dendrites + Fiber Growth Near Metal Blobs
Gd_2O_3 20% CeO_2 12% Mo	4.9	Oxide Dendrites + Eutectic

experimentally observe this phenomenon. Although good results were obtained with one sample (Gd_2O_3 -20 w/o CO_2 -12 w/o Mo at 4.3 cm/hr), the existence and extent of a coupled zone is still inconclusive. It is felt that even though undercooling should be increased by increasing the growth rate the difference could be so small as to make extremely rapid growth rates necessary to change undercooling a significant amount. It is also probable that the growth kinetics, such as mixing and melting, cannot be successfully carried out at greatly increased growth rates. This conclusion is born out by the undissolved metal "blobs" seen in good composite areas while other areas in the sample are oxide rich. There is probably just not enough time to get the metal dissolved and distributed evenly across the growth front when samples are grown too rapidly.

Although the rare earth oxide-metal composites do not, at present, possess uniform fiber arrays comparable to other oxide-metal composite systems, the avenues of approach to eliminate this problem have not been fully explored. Presently composite samples 16 mm in diameter and 70 mm long containing between 8 to 50×10^6 fibers per cm^2 can be routinely grown in the CeO_2 doped Nd_2O_3 and Gd_2O_3 -Mo systems. These systems are quite insensitive to changes in growth atmosphere and display excellent thermal shock resistance. Etching techniques have been devised to produce a variety of fiber-matrix configurations and several samples have been emission tested. The rare-earth oxide-metal systems may prove attractive for future applications

requiring improved mechanical properties or where large quantities of composite area are needed.

b) $\text{Gd}_2\text{O}_3\text{-CeO}_2\text{-W}$

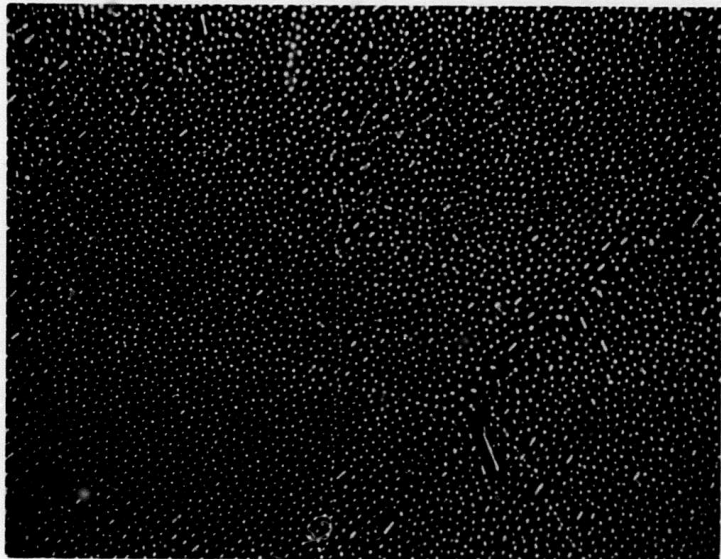
Long (4 to 5 cm) composite areas were difficult to produce in $\text{Gd}_2\text{O}_3\text{-CeO}_2\text{-W}$ samples which had been initially prepared by isostatic pressing. The primary problem was that it was difficult to control the rf generator power so as to maintain the molten zone without decoupling or melting out through the sample skin.

c) $\text{Nd}_2\text{O}_3\text{-CeO}_2\text{-Mo}$

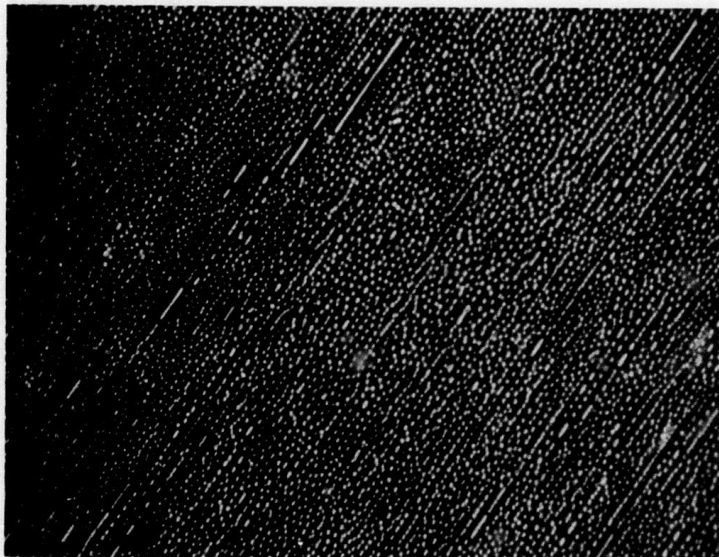
Examination of a long unidirectionally solidified $\text{Nd}_2\text{O}_3\text{-CeO}_2\text{-Mo}$ sample at 3 mm intervals showed that the metal platelets increased in size and number from the base to the top of the solidified zone. Four representative slices from this 30 mm long sample are shown in Figure II-10. This behavior, also noted in the $\text{Gd}_2\text{O}_3\text{-CeO}_2\text{-Mo}$ system, may be related to the segregation of impurities in the upper portion of the sample resulting in conditions favorable for platelet formation.

d) $\text{Gd}_2\text{O}_3\text{-CeO}_2\text{-Rh}$

A $\text{Gd}_2\text{O}_3\text{-CeO}_2\text{-Rh}$ sample (10 w/o Rh) was successfully induction melted and unidirectionally solidified, however, only metal "blobs" were observed in the melted regions of the sample indicating no metal solubility.



a) First Liquid to Solidify, Base.

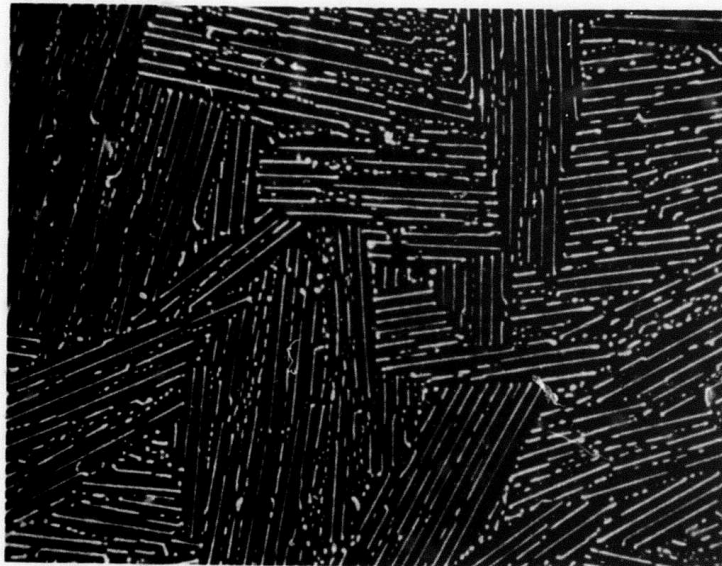


b) 15 mm Above Base

Figure II-10. Transverse Sections of a CeO_2 Doped Nd_2O_3 -Mo Sample Showing the Transition from Fiber to Platelet Morphology from the Base to Top of Solidified Zone. Dark Field, X600.

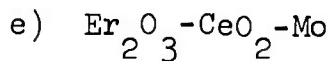


c) 24 mm Above Base

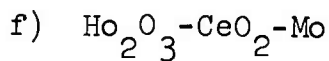


d) Last Liquid to Solidify, 30 mm Above Base.

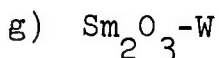
Figure II-10 (Continued).



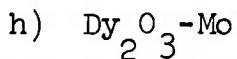
An $\text{Er}_{2/3}\text{O}_3\text{-CeO}_2\text{-Mo}$ sample (10 w/o Mo) was successfully melted and unidirectionally solidified producing an ordered oxide-metal (fiber) eutectic structure.



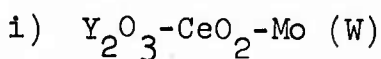
A 10 w/o Mo sample of $\text{Ho}_{2/3}\text{O}_3\text{-CeO}_2$ was also internally melted and unidirectionally solidified and produced an ordered metal fiber composite structure.



A pellet of $\text{Sm}_{2/3}\text{O}_3$ with 10 w/o W was preheated to 1800°C in a $\text{N}_2\text{-H}_2$ atmosphere but the sample could not be induction melted.



A $\text{Dy}_{2/3}\text{O}_3$ pellet containing 5 w/o Mo did not couple when preheated to 1900°C and broke up badly on cooling, suggesting the presence of a destructive phase change.



Composite growth in the CeO_2 doped $\text{Y}_{2/3}\text{O}_3$ - Mo system has been investigated within the compositional ranges of 0 to 50 w/o CeO_2 and 0 to 25 w/o Mo. The effect of various growth atmospheres on composite growth have also been observed.

The optimum starting composition for uniform composite growth has been established as Y_2O_3 - 50 w/o CeO_2 - 15 w/o Mo when the samples are grown at about 2.5 cm/hr in a N_2 - 10 v/o H_2 atmosphere. Composite rods containing 12×10^6 fibers/cm² have been routinely produced using these conditions and a typical microstructure is shown in Figure II-11. More recent experiments have shown that Mo solubility in the molten oxide mixture was increased to 20 w/o or higher when the growth atmosphere was modified by passing the 10 v/o H_2 through H_2O and adding this mixture with the N_2 to the composite growth assembly.

Composite growth in the $(\text{Y}_2\text{O}_3$ - 50 w/o CeO_2) + Mo system possesses several favorable characteristics:

1. Rf coupling is easily accomplished due to the low (1500°C) preheat requirement;
2. The Y_2O_3 (CeO_2) liquid is capable of dissolving large amounts of Mo (20 w/o);
3. Composites are relatively free of banding - no banding has been observed in the composites grown in $\text{N}_2:\text{H}_2/\text{H}_2\text{O}$ atmospheres.

Other Y_2O_3 (CeO_2) - metal mixtures were successfully melted. A Y_2O_3 - 25 w/o CeO_2 + 16 w/o W rod was melted and solidified at 2.2 cm/hr. The microstructure contained extensive areas of ordered platelet growth. Mixtures of Y_2O_3 and CeO_2 containing Ti and Zr were easily induction

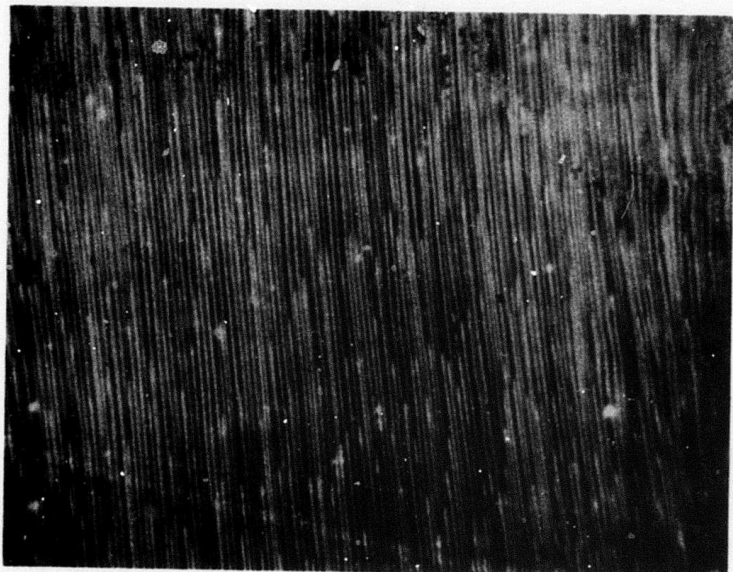


Figure II-11. Longitudinal Section of CeO_2 Doped Y_2O_3 -Mo Samples Grown in a N_2 - 10 v/o H_2 Atmosphere. Dark Field, X600.

melted, but a stable molten zone could not be formed.

Sample cracking has been a problem throughout the CeO_2 doped Y_2O_3 - metal solidification work. However, slow cooling reduced the number of visible cracks in similar samples from 13 to 1 when the cooling rate was reduced to $15^\circ\text{C}/\text{min}$ from $60^\circ\text{C}/\text{min}$. It also appears that the use of high oxygen potential atmospheres such as $\text{N}_2:\text{H}_2/\text{H}_2\text{O}$ or CO/CO_2 reduced cracking.

j) CeO_2 -Mo

Mixtures of CeO_2 and Mo have been induction melted and unidirectionally solidified to produce ordered oxide-metal composites consisting of metal fibers and platelets aligned in the oxide matrix. Mixtures of CeO_2 with other metals (W and Ni) were also investigated; however, the CeO_2 work has centered on CeO_2 -Mo mixtures because of the better structures obtained from this system.

Development studies have emphasized the influence of growth atmospheres and lowering rates on composite geometries. Growth atmospheres employed included N_2 , $\text{N}_2\text{-H}_2$, and $\text{N}_2\text{-CO-CO}_2$ mixtures. Solidification of numerous CeO_2 - 10 w/o Mo samples indicated a growth atmosphere of N_2 - 10 v/o H_2 consistently produced the best samples (see Figure 11-12). Increasing the oxygen potential during growth using $\text{N}_2\text{-CO}_2\text{-CO}$ gas mixtures resulted in an oxide matrix void of any metal; no trace of Mo fibers, platelets or particles could be found in the solidified region.

The influence of lowering rates on composite geometries was studied using CeO_2 - 10 w/o Mo samples solidified in the atmosphere consisting of N_2 - 10 v/o H_2 . The lowering rates varied from 1.0 to 2.8 cm/hr. At the lower growth rates, 1.0 - 1.5 cm/hr, the most uniform and extensive composite geometries were achieved and a typical structure is shown in Figure II-12. At the fast growth rates, 2 cm/hr and above, the occurrence of primary oxide areas (dendrites) increased (see Figure II-13).

The system CeO_2 -Mo has not been as extensively studied as is the case for UO_2 -W; however, the wide stoichiometry changes existing from CeO_2 to $\text{Ce}_{2/3}\text{O}_3$ suggest most of the comments pertinent to UO_2 -W eutectic growth (Section II A2) are most applicable to CeO_2 -metal systems. A potential unique feature with CeO_2 is that its oxide-metal eutectic temperatures are significantly below that obtained with the current refractory oxides under investigation, and consequently, CeO_2 , with proper stoichiometry control, is considered a possible host for a variety of the lower melting metals. However, the initial attempts to produce CeO_2 -Ni composites have not been successful so far.

4. Al_2O_3 (Cr_2O_3) - W or Mo

Alumina would be an attractive matrix material for oxide-metal composites; however, most efforts to induction melt this material have been unsuccessful because of the

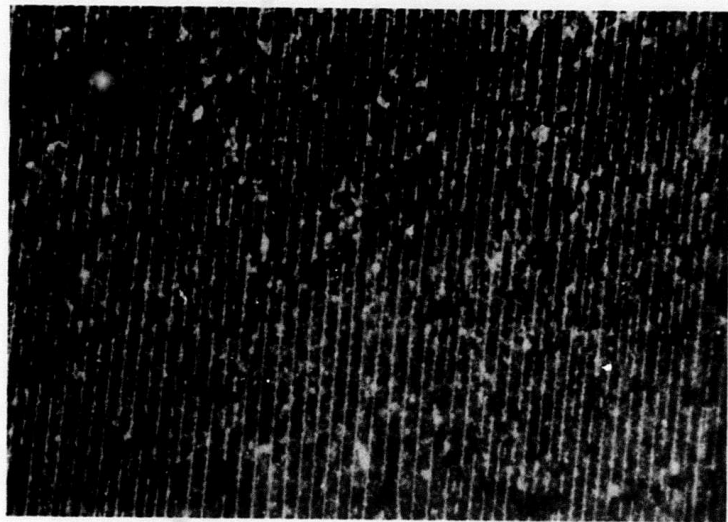


Figure II-12. Longitudinal Section of CeO_2 - 10 w/o Mo Sample (Showing Mo Platelets) Solidified in a N_2 - 10 v/o H_2 Atmosphere. Dark Field, X600.

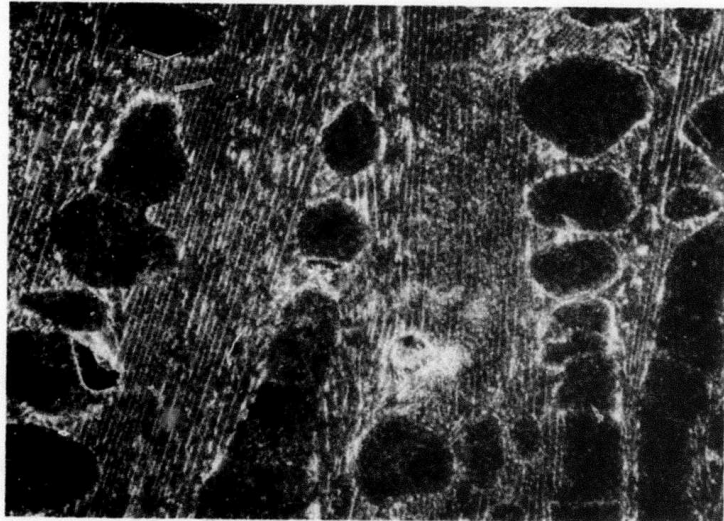


Figure II-13. Longitudinal Section of CeO_2 - 10 w/o Mo Sample (Displaying Oxide Dendrites) Solidified at 2.8 cm/hr. Dark Field, X600.

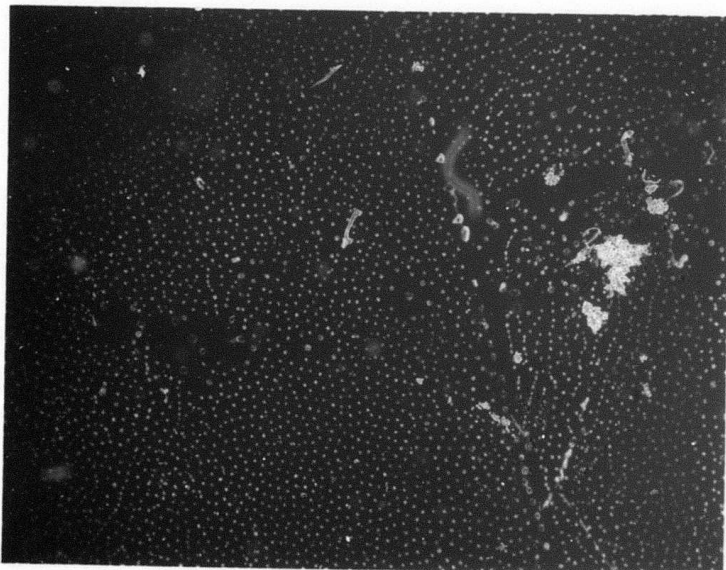
inability to impart enough electrical conductivity for eddy current heating. Two different techniques were described previously¹ for melting $\text{Al}_2\text{O}_3(\text{Cr}_2\text{O}_3)$ -W or Mo mixtures using direct rf heating, but unfortunately there was little if any apparent solubility of the refractory metals in these molten oxides.

5. Cr_2O_3 -Mo

Mixtures of Cr_2O_3 containing 3 w/o Cr metal were melted in closed Mo crucibles using rf heating and solidified by slowly lowering the crucible out of the rf coil. The resulting structures contained many well ordered fiber structure areas. (See Figure II-14). These fibers were determined to be predominately Mo by analyzing the primary x-rays produced by electron impingement in the SEM. Apparently the solubility and mobility of Mo (dissolved from the crucible walls) is sufficient to readily disperse this metal in molten Cr_2O_3 . Since the x-ray analysis indicated that both the starting and melted matrix material was type III Cr_2O_3 , it is uncertain as to the location of the Cr metal added in the original starting mixture. The metallic fibers could actually be a Mo-Cr alloy, since it would be impossible to distinguish any Cr in the fibers from the intense Cr background from the Cr_2O_3 matrix.



a) Bright Field,
X600.



b) Dark Field,
X600.

Figure II-14. Eutectic Regions in Cr_2O_3 -Mo(Cr) Samples Solidified in a Mo Crucible.

B. EFFECT OF LOWERING RATE ON THE EUTECTIC COMPOSITION OF UNIDIRECTIONALLY SOLIDIFIED OXIDE-METAL MIXTURE

As has been reported in previous reports,^{1,2,3} the fiber density and fiber diameter of unidirectionally solidified oxide-metal composites vary with growth rate. If the eutectic composition for a given system was independent of growth rate, the volume percent metal calculated by determining the product of fiber cross-sectional area and fiber density should be a constant for different growth rates. This has not proven to be the case in analysis of single samples in the UO_2 -W, Gd_2O_3 - CeO_2 -Mo and ZrO_2 - Y_2O_3 -W systems.¹

The first analysis of the volume % Mo contained in the eutectic composition of CeO_2 doped Gd_2O_3 samples at five different lowering rates was found to follow the parabolic equation

$$Y = 8.927 - 3.500X + 0.3947X^2$$

where Y is the volume % Mo, and X is the growth rate in cm/hr.¹ A plot of this curve and the experimentally determined Mo v/o is shown in Figure II-15. The results of similar analysis of UO_2 -W and ZrO_2 - Y_2O_3 -W composites also indicated a minimum in the metal content for samples grown at 4-6 cm/hr.¹

A second investigation of the effect of growth rate on the eutectic compositions of Gd_2O_3 - CeO_2 -Mo composites indicated that the v/o Mo decreased with increasing growth rates and then increased as the growth rate was increased above 4 cm/hr.

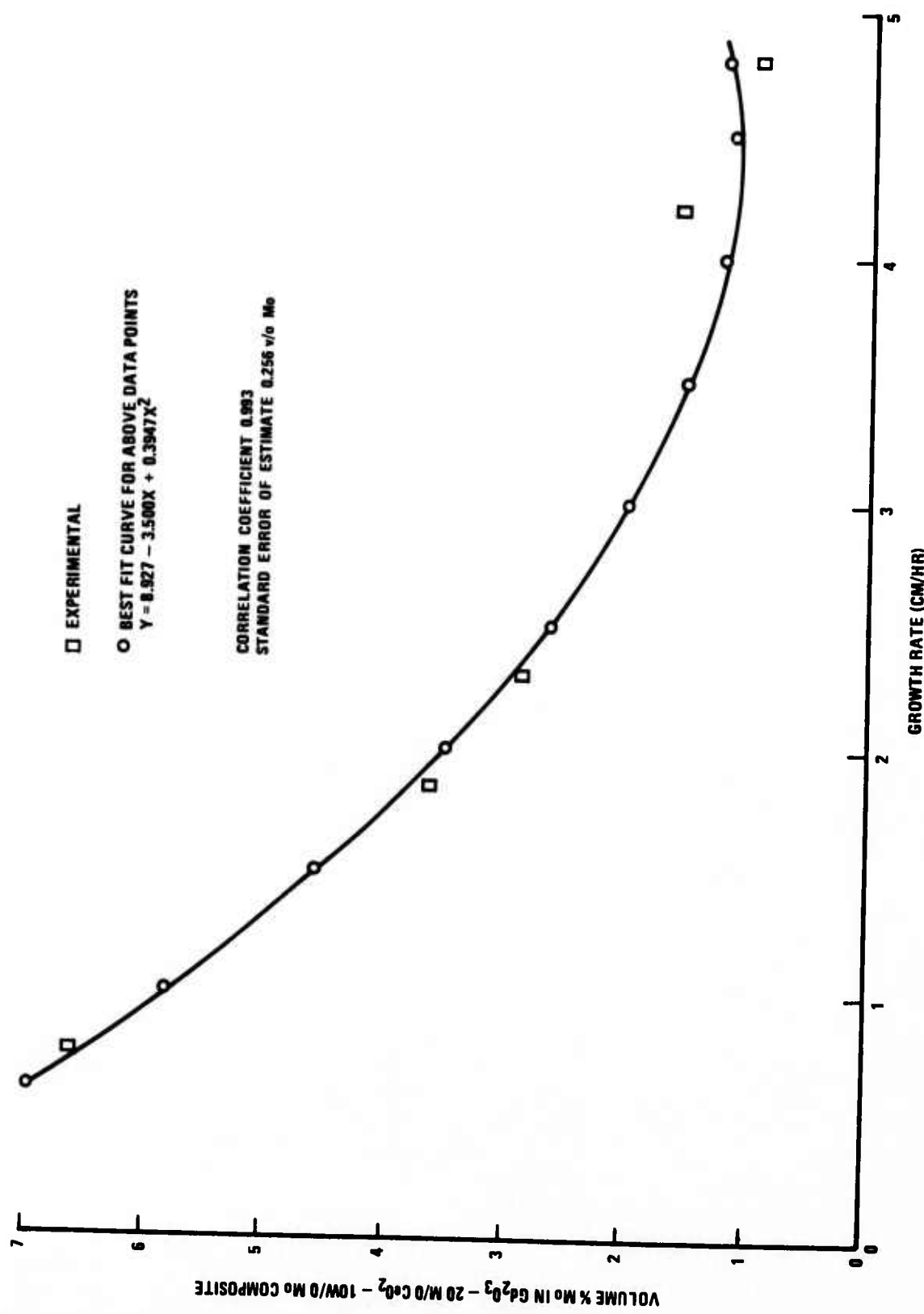


Figure III-15. Effect of Growth Rate on v/o Mo Present as Fibers in $\text{Gd}_2\text{O}_3\text{-CeO}_2\text{-Mo}$ Composites.

(Behavior similar to that shown in Figure II-15). It should be noted, however, that in the second analysis of the Gd_2O_3 - CeO_2 -Mo samples the Mo contents were significantly higher than those shown in Figure II-15. X-ray analysis of the 405 d spacing increased with increasing growth rates. This might indicate that at least some Mo is in solid solution in the Gd_2O_3 samples grown at the faster rates. Since examination of three oxide-metal systems showed a decrease in the metal component (found in the eutectic structures) as the growth rate increased up to about 4 cm/hr, it is likely this is a realistic model of oxide-metal solidification behavior. However, no completely satisfactory explanation for this behavior has been found.

C. ELECTRON BEAM MELTING AND SOLIDIFICATION OF OXIDE-METAL SYSTEMS

A Materials Research Corporation electron beam zone refiner has been utilized in attempts to produce unidirectionally solidified eutectic composites in oxide-metal systems that cannot be inductively melted or cannot be successfully self-contained using the internal floating zone technique because of their low melting points.

The last Report¹ described a series of modifications to the eb zone refiner that were necessary in order to utilize this equipment for oxide-metal melting experiments (in Mo crucibles) at temperatures above 2000°C.

After these modifications were completed, a spinel ($\text{Al}_2\text{O}_3 \cdot \text{MgO}$)-10 w/o Mo mixture was heated above the melting point of the spinel (2105°C). Examination of the sample showed unmelted Mo particles surrounded by solidified spinel matrix. Additional samples of spinel ($\text{Al}_2\text{O}_3 \cdot \text{MgO}$) containing 10 w/o of either Fe, Ni, or Co were melted in Mo crucibles in the electron beam furnace in an attempt to grow oxide-metal composites containing magnetic fibers. Random metal spheres were observed in all three samples after melting and the samples containing Ni and Co appeared to contain a second oxide phase at the grain boundaries. The Co addition colored the spinel matrix blue, indicating some solubility, at least in the solid state.

The primary experimental problems associated with developing successful electron beam melting techniques suitable for the unidirectional solidification of oxide-metal mixtures are: the difficulty in obtaining accurate temperature readings on the highly reflective crucible wall, just behind the hot tungsten filament, the increase in crucible temperature as the thermal geometry changes as the hot zone is moved towards the top of the crucible and electrical leakage or arcs caused by vapor depositions of crucible metal on insulators.

D. POSSIBLE BANDING MECHANISMS IN OXIDE-METAL COMPOSITES

The major growth discontinuity observed in the oxide-metal eutectic structures is a horizontal oxide band, partially or completely void of metal, which interrupts the growth of continuous parallel fibers. This phenomenon is termed "banding" and three types of banding have been observed in essentially all the unidirectionally solidified oxide-metal systems.

The most disruptive type of banding (Figure II-16) consists of an abrupt halt in fiber growth, above which a rather wide band of oxide which contains metal droplets is solidified. The fibers subsequently are renucleated in a limited number of sites at the top of the band and fan out to again produce a continuous uniform fiber structure. This second type appears similar to the first type except the oxide bands are generally thinner (Figure II-17) and there is no solidified metal in the oxide band. The third type of banding (Figure II-18) consists of a much thinner band of oxide (1-5 μm thick) and a few of the fibers may be continuous across the band.

It has been previously reported² that the first type of banding is the result of power fluctuations equivalent to typical line voltage variations occurring during the solidification process. Possible explanations for the other two types are discussed below.

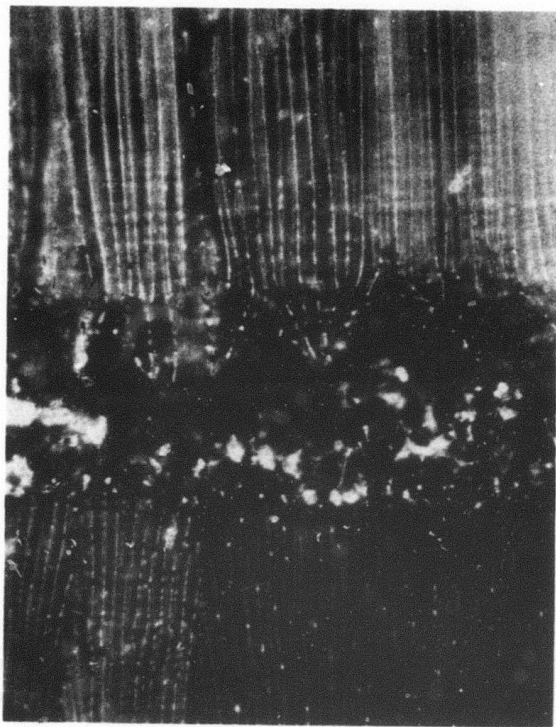


Figure II-16. Banding Produced by a Power Fluctuation
in a Y_2O_3 Stabilized ZrO_2 -W Composite.
Dark Field, X600.

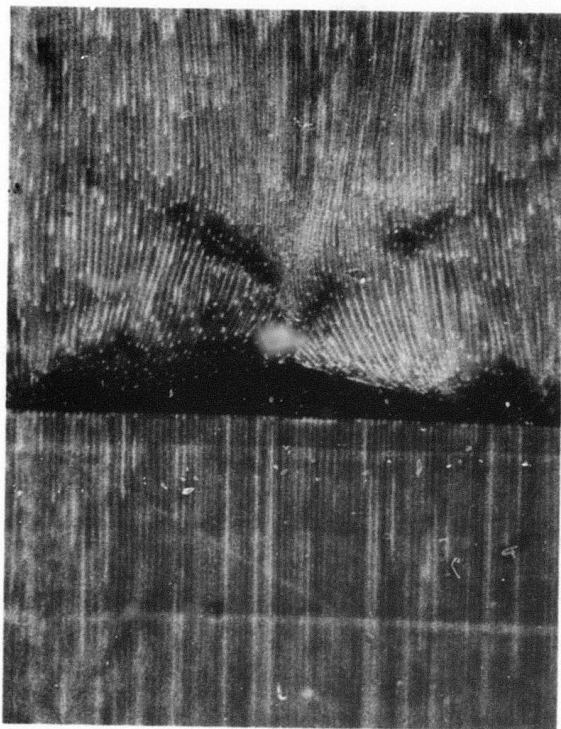


Figure II-17. Fan Type Banding in Oxide-Rich Area of a Y_2O_3 Stabilized ZrO_2 -W Composite. Dark Field, X600.

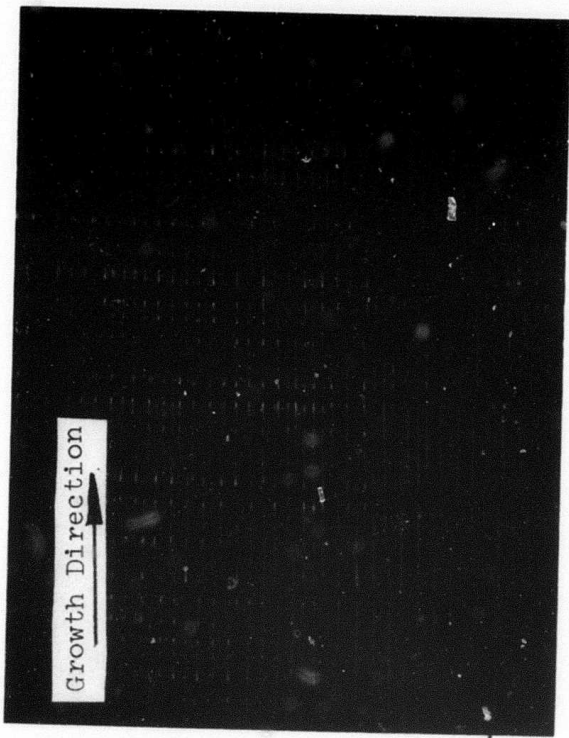


Figure II-18. Thin Oxide Band With Aligned Fibers in a Y_2O_3 Stabilized ZrO_2 -W Composite. Dark Field, x600.

The second type of banding (Figure II-17) is most likely related to the depletion of the metal content of the liquid ahead of the solidification front during the solidification process. If the metal content of the liquid is decreased sufficiently (in effect supersaturated with primary oxide), the eutectic growth could suddenly stop and a band of primary oxide containing no metal would precipitate. As this occurs the metal concentration of the liquid would increase until a few stable metal nuclei form, and then the metal fibers would appear to fan out from these renucleation sites. An alternate mechanism to revert an oxide-rich liquid back toward the eutectic composition is through the formation of oxide dendrites; such structures typically display circular primary oxide areas in both longitudinal and transverse sections of the composites.

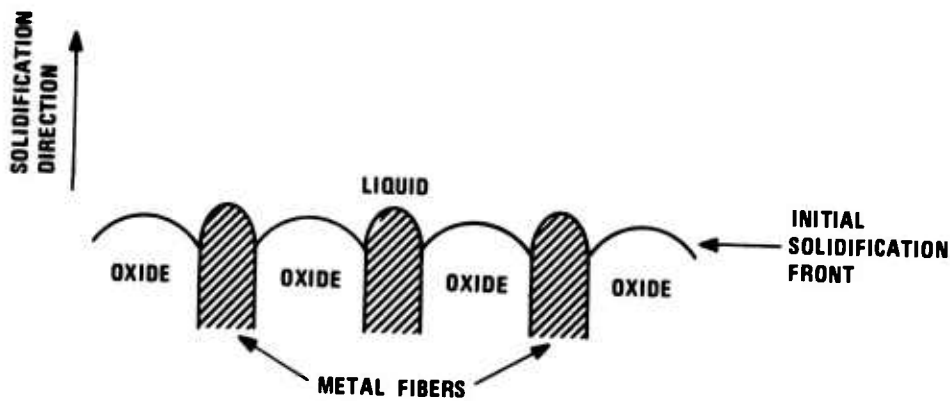
Thin banding (Figure II-18) may be related to small, short duration variations of the energy absorbed by the liquid pool in the sample during composite growth. The energy supplied to the liquid pool could be temporarily increased by two possible mechanisms, rapid fluctuations in the rf generator line voltage or the change in the density of the magnetic field in the liquid pool due to a geometrical change of the interior of the pellet (such as a very large drop of liquid falling from the roof of the void into the liquid pool). This in turn could cause a thin layer of the solidified material to remelt. As the energy level quickly returns to normal, the initial solidification is pure oxide as the supersaturation necessary for metal nucleation is absent, and the concentration gradients existing in the liquid

necessary for eutectic growth were destroyed during remelting. The precipitation of pure oxide increases the metal content of the liquid (ahead of the solidifying oxide) until the required supersaturation results. Supersaturation occurs first in the liquid region just above the existing fibers since the excess energy condition lasted only a short time, and the metal from the remelted fibers does not have time to uniformly disperse within the oxide liquid by diffusion (Figure II-19-b). This process may account for the almost perfect alignment of the fibers across the narrow oxide band (Figure II-19-c).

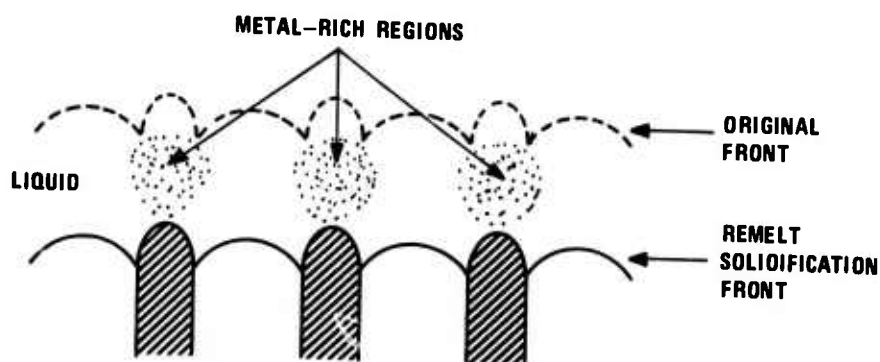
E. X-RAY ANALYSIS OF OXIDE-METAL COMPOSITES

In the previous work^{1,3} the orientation relationship of the metallic fibers and oxide matrix was estimated using x-ray methods on bulk polygrain composite samples. An improved method which can precisely determine the orientation of the fibers and matrix within a cell has been developed. A single cell which was separated from the bulk composite was examined using the diffractometer single crystal technique and a Laue back reflection pattern. This method was mainly applied to UO_2 -W samples because this system was chosen for the majority of field emission experiments and its cell sizes were large enough to utilize these methods.

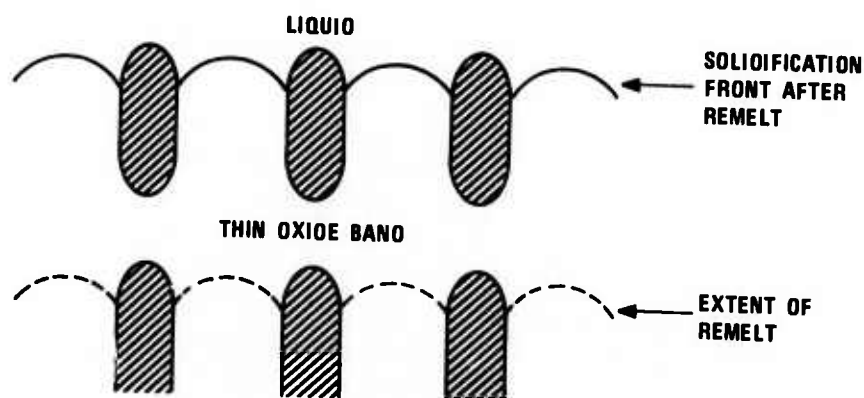
The bulk composite sample was first crushed and the "grains" were examined using an optical microscope and a large single "grain" (cell) was chosen for x-ray examination. The grain (in which the growth direction was easily identifiable)



A. BEFORE REMELTING



B. DURING REMELTING



C. AFTER UNIFORM GROWTH REINITIATED

Figure II-19. Schematic Diagram of Steps Leading to a Thin Oxide Band During a Minor Remelt.

was attached to the goniometer head of the single crystal orienter of the G. E. XRD-6 diffractometer. The 2θ angle was set on the position for the (111) UO_2 reflection. The angles χ and ϕ (see Figure II-20) were then systematically adjusted until a reflection was detected at the maximum intensity. These values of χ and ϕ were the orientation of a (111) pole of UO_2 . Two poles can determine an orientation of a crystal; however, in order to completely confirm the orientation, all four (111) poles of the UO_2 were searched. The 2θ angle was then repositioned so that (110) reflection of the W fibers was detected. The same process was used to record the various (110) poles of the W fibers.

Figure II-20 shows that the orientation of the W fibers and UO_2 matrix are almost identical. The growth direction of both the fibers and matrix is very close to the (111) pole. Figure II-21 shows the Laue back reflection of the same grain. The reflections from the fibers spread into clusters of barely visible tiny spots (because of the very small W content of the composites) which consistently fall on the zones reflected from the UO_2 matrix. Note that the Laue pattern was taken approximately 25° from the growth direction of the grain. There are also a few very weak reflection rings in Figure II-21 which may be reflections from random orientated W fibers as the diffraction angles correspond to that of tungsten.

DETECTED (110) REFLECTION OF FIBRES, ★ DETECTED (111) REFLECTIONS OF MATRIX,
SAMPLE GROWTH DIRECTION. Δ [111], \square [110], \square [100], \circ [112].

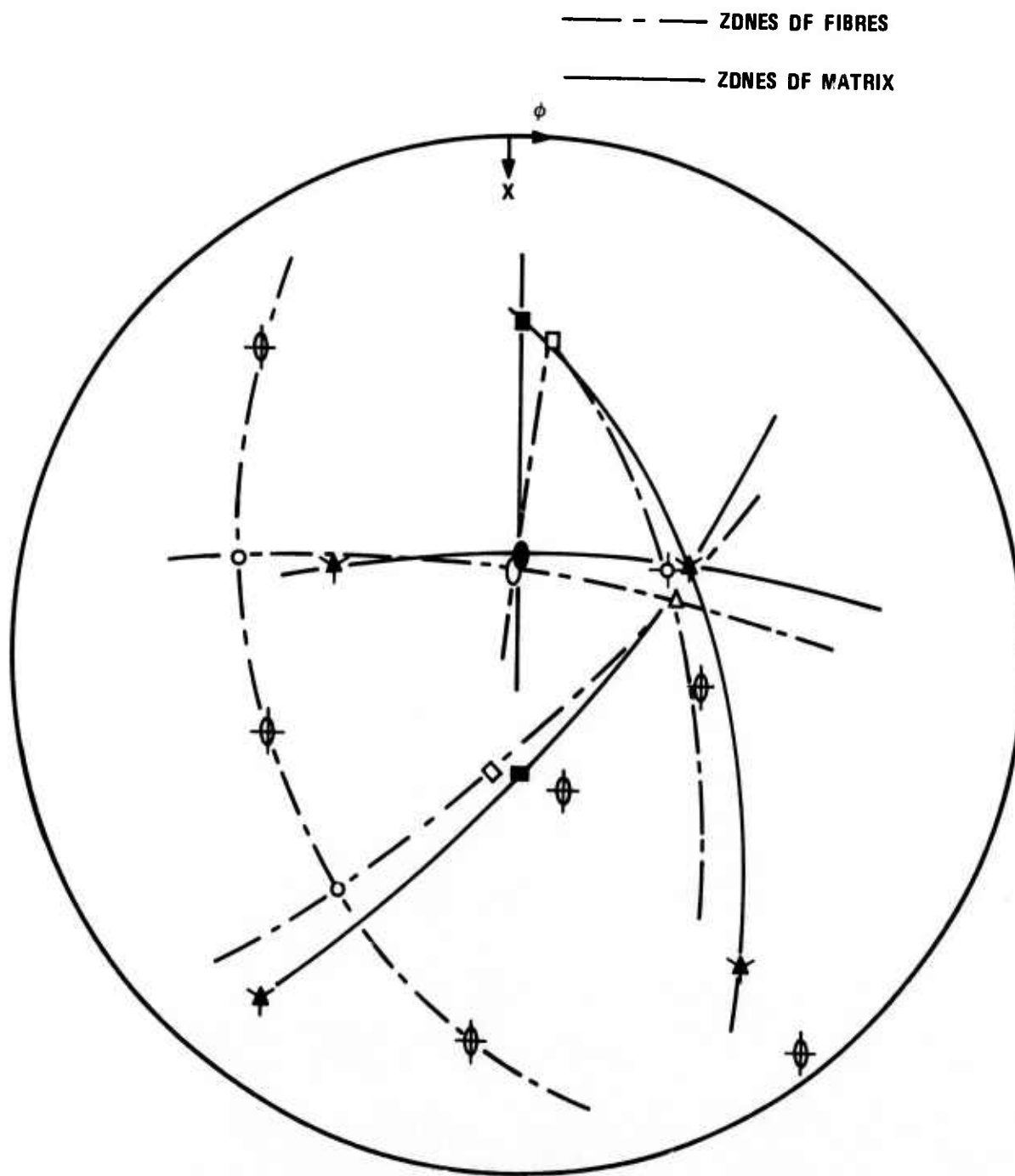


Figure II-20. The Orientation Relationships of the Metal Fibers and Oxide Matrix in a Single Cell from UO_2 -W Sample No. 113-23-1. Hollow Marks are Poles of the Fibers; Solid Marks are Poles of the Matrix.

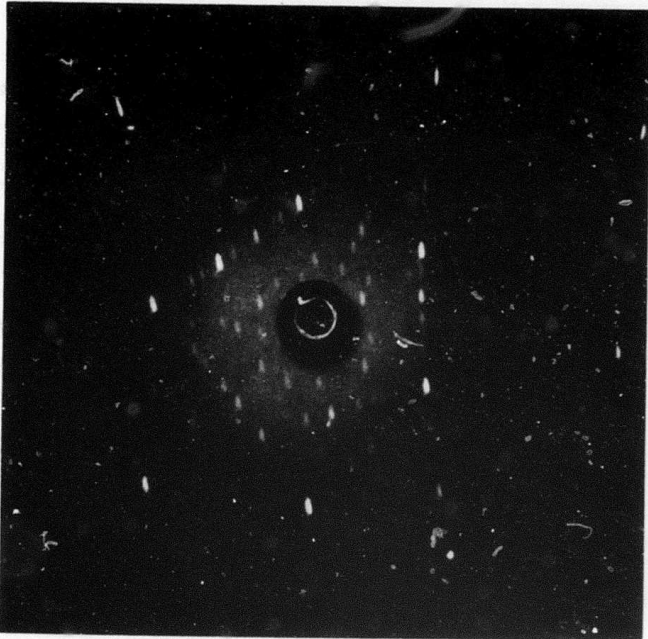


Figure II-21. Laue Pattern for Single Cell from UO_2 -W
Sample No. 113-23-1.

The orientation relationship of another UO_2 -W composite grain in which the (111) pole of UO_2 and (110) of tungsten fibers are both close to the growth direction is shown in Figure II-22. The (110) direction of fibers was approximately 14° from the (111) direction of the matrix. The (110) zone of the matrix closely matched with the (211) zone of fibers. The back reflection Laue pattern is shown in Figure II-23. Several additional UO_2 -W grains have been examined using the same method. Usually it was rather difficult to determine the orientation of the fibers because of the overlap of the reflections from more than one orientation. The detected extra (110) reflections of the W fibers shown in Figures II-20 and II-22 is the evidence of this overlapping.

Based on the x-ray analysis of these two single grains, the following conclusions can be drawn regarding the orientation relationships in the UO_2 -W composites. The UO_2 matrix has a very strong (111) preferred growth direction. There are three types of W fibers: (1) the fibers which have their orientation identical with that of the matrix, (2) fibers which have a (110) growth direction independent of the matrix orientation, (3) randomly oriented fibers.

The same x-ray technique was employed in an effort to determine the orientation of the Gd_2O_3 -Mo system; however, the cells were too small for single analysis. In addition, the apparent single cell grains as judged by the optical

DETECTED (110) REFLECTION OF FIBRES, \star DETECTED (111) REFLECTIONS OF MATRIX,
 SAMPLE GROWTH DIRECTION. Δ [111], \bigcirc [110], \square [100], \circ [112].

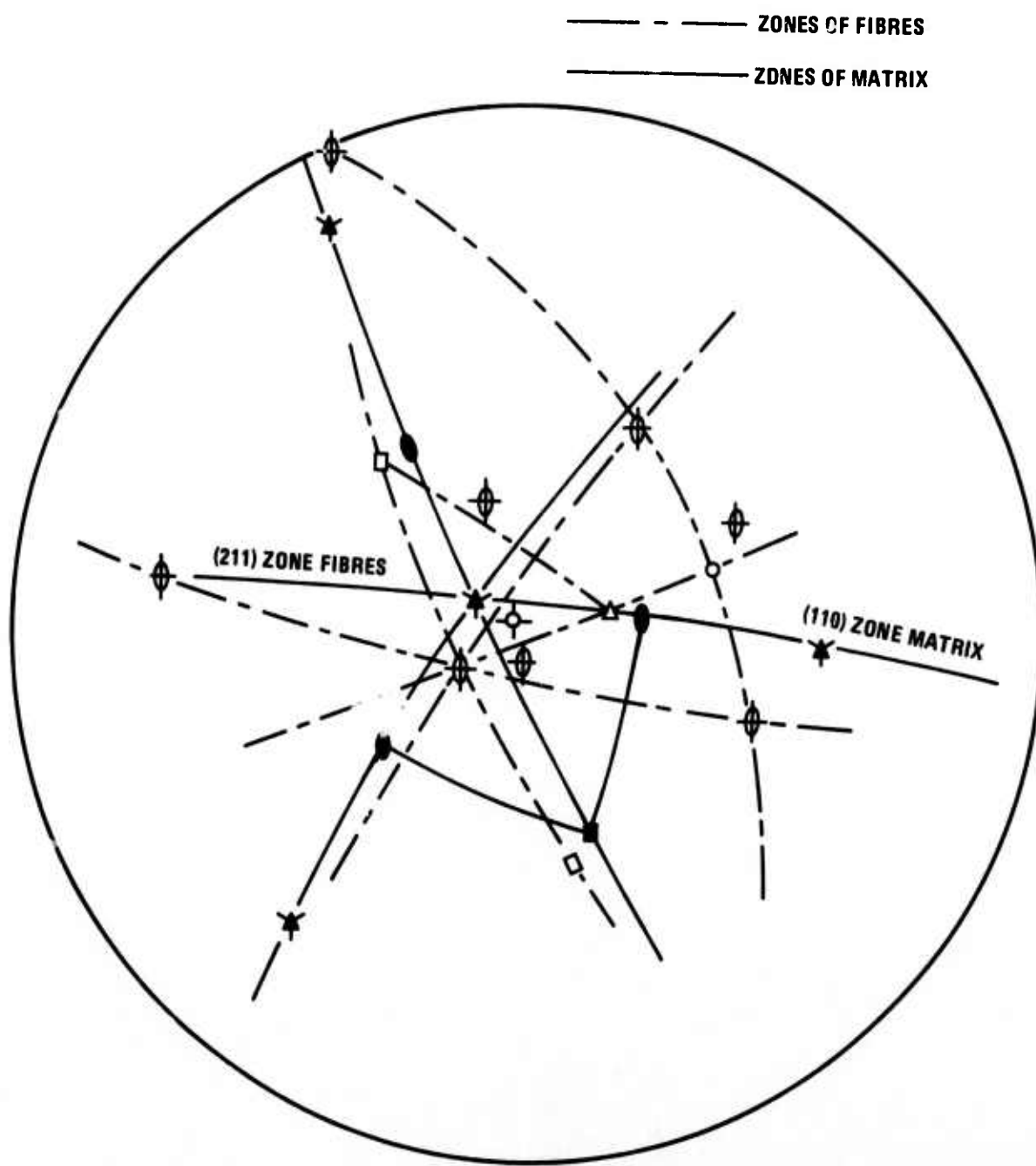


Figure II-22. The Orientation Relationships of the Metal Fibers and Oxide Matrix in a Single Cell from UO_2 -W Sample No. 113-23-2. Hollow Marks are Poles of the Fibers; Solid Marks are Poles of the Matrix.

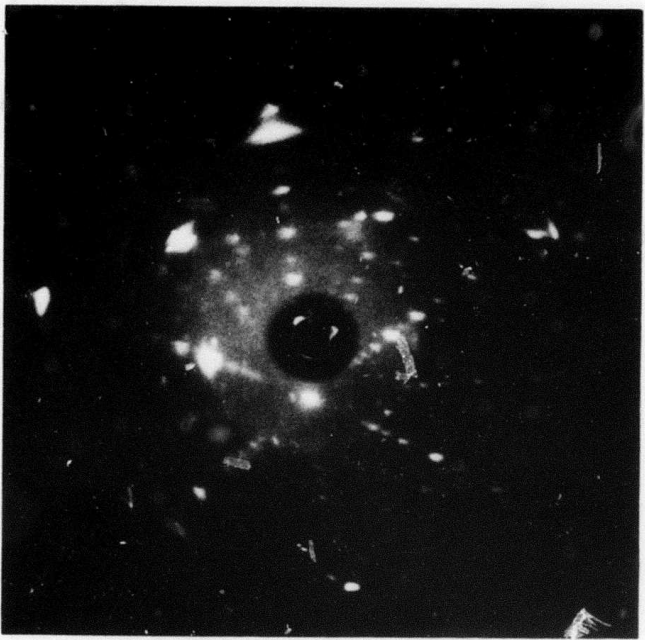


Figure II-23. Laue Pattern for Single Cell from
 $\text{UO}_2\text{-W}$ Sample No. 113-23-2.

microscope usually turned out to be polycrystals when examined by x-ray. Pole figures of (110) of Mo, (222) and (313) of Gd_2O_3 were studied. It was found that the Gd_2O_3 matrix has a preferred growth direction at (313). No preferred growth for Mo fibers was determined. Also the pole figures of (110) Mo and (222) Gd_2O_3 are compatible and it is suggested that (110) Mo // (222) Gd_2O_3 .

Since the thermal expansion of the metal fibers and the oxide matrix are not the same, the metal fibers may have a considerable strain. An x-ray line broadening experiment was conducted to determine the internal strain and particle size of the metallic fibers in both UO_2 -W and Gd_2O_3 -Mo samples. Two different reflections are needed to determine both the particle size and strain by line broadening analysis⁹, usually (110) and (220) for bcc metals, (111) and (222) for fcc metals. However, for an elastic isotropic metal such as tungsten, any two reflections may be used for the analysis.¹⁰ In the UO_2 -W samples the (220) reflection of tungsten was overlapped by the (224) reflection of UO_2 , therefore (211) was substituted for (220). While in the Gd_2O_3 -Mo system, (110) and (220) reflections of Mo were used for the analysis. A well annealed tungsten powder was used as a standard for the instrumental correction.

The results of this analysis indicated there was negligible particle size broadening for the W and Mo fibers, i.e., the particle size was larger than 1000 \AA . However,

there are measurable root-mean-squared strain in the fibers of both composites, especially in the case of the W fibers in UO_2 . The Mo fibers in Gd_2O_3 had a rms strain of

$$\langle \epsilon^2 \rangle_{50 \text{ \AA}}^{1/2} = 0.0010$$

which is lower than that observed for Mo filings¹¹ ($\langle \epsilon^2 \rangle_{50 \text{ \AA}}^{1/2} = 0.0032$). However, the strain observed for the W in UO_2 was

$$\langle \epsilon^2 \rangle_{50 \text{ \AA}}^{1/2} = 0.0052$$

which is higher than that found for W filings¹⁰ ($\langle \epsilon^2 \rangle_{50 \text{ \AA}}^{1/2} = 0.0038$).

The occurrence of strain in the metal fibers in the oxide-metal composites was expected because of the large difference in the expansion coefficients of the refractory metals and oxides. It was also reasonable to observe the larger strain in the W since it displays less ductility than the Mo and has a lower expansion coefficient. In fact, it was somewhat surprising that more strain was not detected in the metal fibers because of this mismatch in expansion characteristics between the oxide and metal components of the composites.

SECTION III

THE FORMATION OF OPTIMUM EMITTING ARRAYS

The objective of this phase of the research program was to develop emitting geometries from the oxide-metal composites for use in the experimental electron field emission testing work. In previous reports the results of selective chemical etching studies on UO_2 -W^{1,2,3,4}, Gd_2O_3 -Mo¹, and ZrO_2 -W and HfO_2 -W² samples have been described. Analysis of the chemical etching behavior of the UO_2 -W composites has received most attention because of the better emission performance of this material. Recent field emission test results suggested the use of pointed W pins (pin tip radius ~ 100 Å) may have led to localized pin tip heating and subsequent electrical breakdown. Consequently, some of the work designed to achieve ideal emitting geometries for UO_2 -W samples performed this reporting period utilized annealing techniques to increase the emitting area through the formation of larger diameter rounded or hemispherical pin tips. The system CeO_2 doped Gd_2O_3 -Mo also received extensive attention using both chemical etching and annealing approaches to achieve a variety of Mo pin geometries. The best chemical etching solutions and conditions established previously¹ were used as a starting point for this further study on the Gd_2O_3 -Mo samples.

A. UO_2 -W EMITTING ARRAYS

A number of areas of interest in the etching of UO_2 -W composites have been investigated and the following items will be reported in this section.

1. Pointed, recessed pins for low voltage emitter geometries
2. Rate of W removal in etching of holes
3. The alteration of pin tip shape by annealing
4. Accurate determination of UO_2 etching rate
5. Effects of etchant aging

The capability of producing pointed W fibers recessed into the oxide matrix has been reported previously¹ using the following etchant composition:

20 ml glacial acetic acid	}	Pointed recessed pin etchant
20 ml saturated aqueous CrO_3 solution		
14 ml concentrated HNO_3		
20 ml concentrated HF		

In this work the fibers were recessed into holes which were approximately three times the diameter of the fibers with the fiber tips either flush with the oxide surface or only slightly recessed ($\sim 0.5\mu\text{m}$, see Figure III-1). A number of etchant compositional variations were tried in attempts to increase the recession of the fiber tips. Although reduction of chromic acid content in an etchant used for producing exposed pointed fibers was the change that first produced this geometry¹, further reduction of chromic acid did not

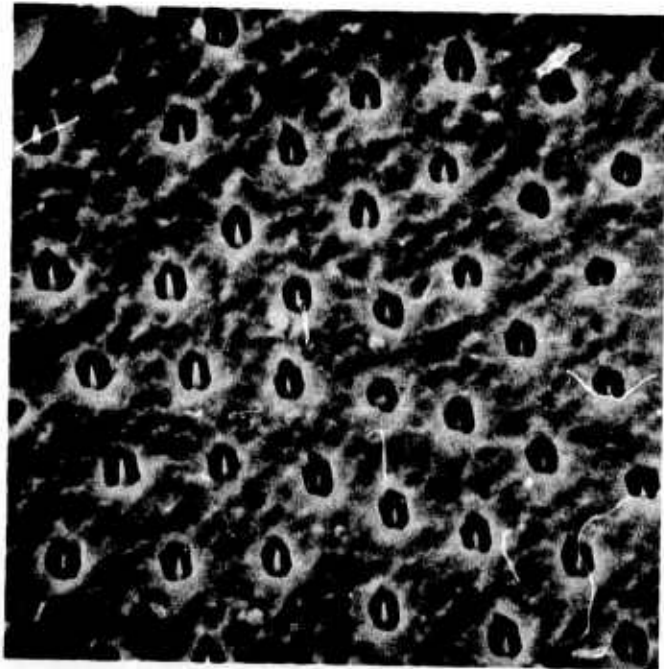
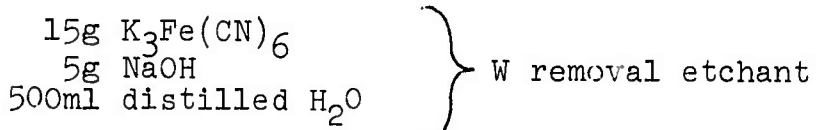


Figure III-1. UO_2 -W Composite Displaying W Pins Recessed In Oxide Matrix. Scanning Electron Micrograph, X6,400.

give the desired results. Changes in hydrofluoric and nitric acid concentrations were also tried without success.

In another scheme designed to produce pointed recessed pins the fibers were recessed $2-4\mu\text{m}$ using a $\text{K}_3\text{Fe}(\text{CN})_6$ -NaOH solution prior to treatment in the etchant used to produce the pointed recessed pins. The etchant composition used to recess the pins was:



Recessing of pins was accomplished by holding the sample in tweezers and agitating vigorously in the etchant for about five seconds. After recessing the W pins the sample was etched in the composition noted above to produce pointed, recessed pins, but no increase in recession depth was observed after the treatment. Consequently, the sample shown in Figure III-1 is the best recessed pin geometry available at present.

The necessity of understanding the mechanism used to selectively remove the W fibers led to an investigation of this etching process. Prior work had shown that a wide concentration range of the $\text{K}_3\text{Fe}(\text{CN})_6$ -NaOH etchant would successfully remove the W fibers, but the dependence of the hole depth on time of etching and etchant concentration was not defined. A direct method of hole depth measurement was devised since previous attempts to measure changes in

resistance or other properties as a function of hole depth were unsuccessful. The samples were first polished on $1\mu\text{m}$ diamond paste and thoroughly cleaned and rinsed in the ultrasonic cleaner. Etching was performed by rotation of the sample at 20 rpm in the $\text{K}_3\text{Fe}(\text{CN})_6$ -NaOH etchant at room temperature (22-25°C) and the etching times were 10, 30, 90, and 300 seconds. This step was followed by treatment in an etchant which removed the oxide matrix at a known rate (the determination of this rate will be described later in this section) without affecting the W fibers. Once the fibers were re-exposed, their height was measured using optical examination in the metallograph by moving the plane of focus from the matrix surface to the fiber tips and noting the difference in elevation. Subtracting this fiber height from the amount of oxide known to have been removed gave the depth to which the W fibers were recessed by the $\text{K}_3\text{Fe}(\text{CN})_6$ -NaOH etchant.

A series of experiments were completed for the above stated etching times using the W removal etchant and the results are shown in Figure III-2. The relationship between hole depth and etching time for this etchant concentration appears to be essentially parabolic for etching times up to five minutes. Diluting this etchant with distilled H_2O to 0.1 of its initial concentration showed virtually no attack on the W fibers for short etching times.

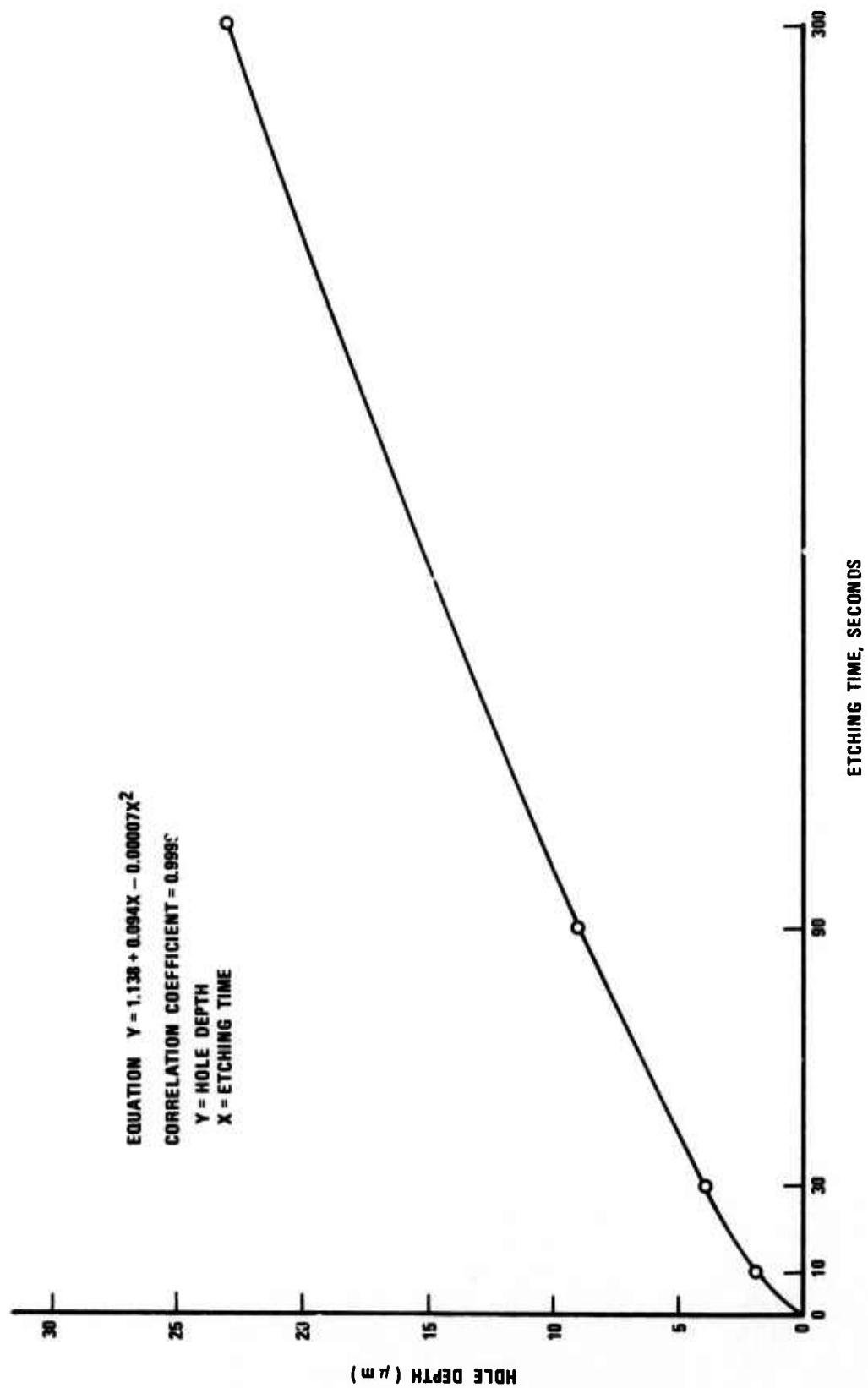


Figure III-2. Plot of Hole Depth vs. Etching Time for UO_2 -W Composite in $\text{K}_3\text{Fe}(\text{CN})_6$ -NaOH Etchant.

The shape of the fiber tips obtained from samples where the pins were initially recessed, and subsequently exposed, were observed in the SEM for possible use as emitter test samples. Inspection of a typical sample, shown in Figure III-3, revealed that the fiber tips were essentially blunt with some radiusing of the corners. On the basis of this information an experiment was performed to determine whether or not the tip shape could be modified by heat treatment. After recessing the W pins with the $K_3Fe(CN)_6$ -NaOH etchant, a UO_2 -W sample was annealed at 1600-1700°C for five minutes in an induction heated Mo cylinder. The fibers were then re-exposed by etching the matrix away without affecting the fibers and the sample was inspected in the SEM. Figure III-4 shows the definite rounding of the fiber tips produced by this procedure and this hemispherical pin tip shape was emission tested (described in Section V).

Alternate methods of producing hemispherical W pin tips were explored using annealing treatments on UO_2 -W samples with exposed pins. The initial annealing treatments were performed at 1600°C using samples with both cylindrical and pointed pin tips. Annealing was accomplished inside an induction heated Mo tube using a H_2 atmosphere and employed approximately two hours to both heat and cool the samples. Figure III-5 shows a sample which initially had cylindrical shaped pins after the 1600°C annealing for 15 minutes. The pin tip rounding appears uniform; however, the tip radius has

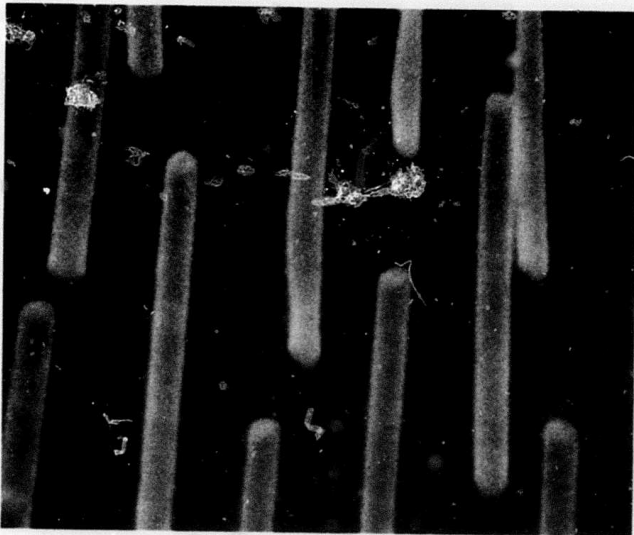


Figure III-3. Blunt Tip Shapes Obtained in UO_2 -W Composite by Etching of Holes with $K_3Fe(CN)_6$ -NaOH etchant. Scanning Electron Micrograph, X10,600.

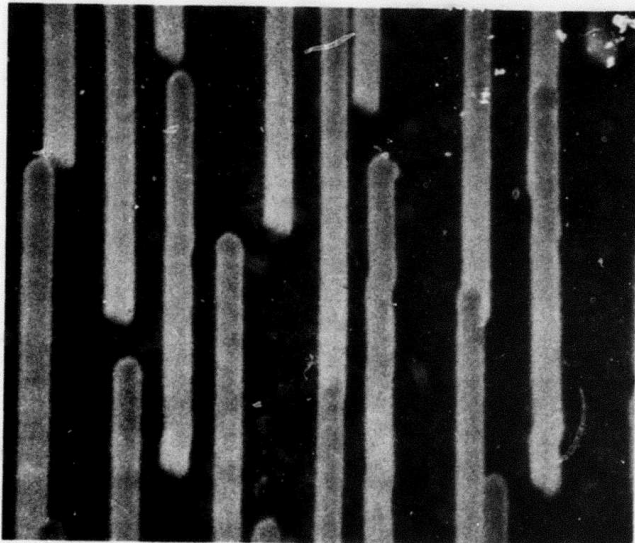


Figure III-4. Rounded Tip Shapes Obtained by Annealing of UO_2 -W Composite in Which W Has Been Selectively Removed by $K_3Fe(CN)_6$ -NaOH Etchant. Scanning Electron Micrograph, X10,900.

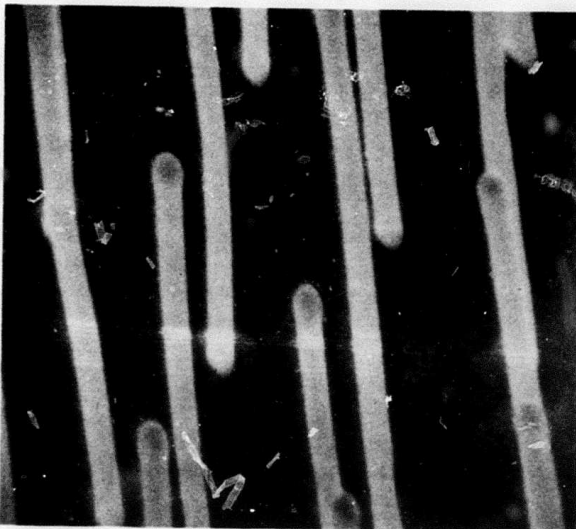


Figure III-5. Initially Cylindrical, Unpointed W Pins in UO_2 -W Composite after Annealing at $1600^{\circ}C$ for 15 minutes. Scanning Electron Micrograph, X10,000.

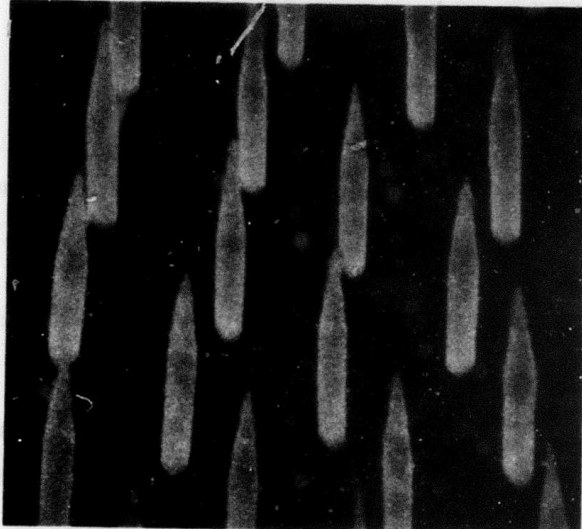


Figure III-6. Pointed W Pins in UO_2 -W Composite As Etched. Scanning Electron Micrograph, X11,200.

increased to yield a "bulbous" shape. Comparison of the pin tip shape of this sample with the geometry of the pins resulting from annealing with the pins recessed in the matrix (Figure III-4) indicates the matrix effectively constrained the surface forces and maintained a uniform pin tip radius.

In an effort to produce rounded tips of smaller diameter, samples initially treated to produce pointed fibers (as shown in Figure III-6) were also annealed at various temperatures for different times (the etching procedures used to obtain this pin geometry were described previously²).

A variety of etching times and temperatures were investigated and two UO_2 -W samples treated at $1600^{\circ}C$ for 15 minutes and at $1400^{\circ}C$ for 25 minutes are shown in Figures III-7 and III-8. These results suggest the $1400^{\circ}C$ annealing is nearly ideal for producing pin tip geometries which approach prolate spheroids. Unfortunately, the annealing of samples with initially sharpened pins was performed late in the contract period and the electron emission characteristics of this geometry were not experimentally checked.

Another area which was investigated in the course of the work to determine the rate of W removal to produce holes was the determination of an accurate rate of removal of the UO_2 matrix material. As noted previously², an etchant

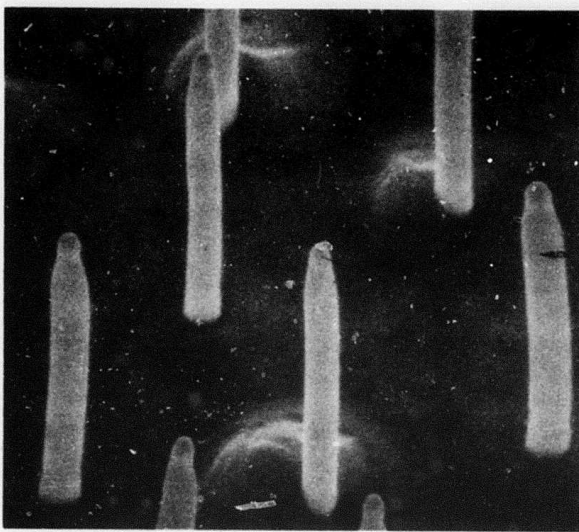


Figure III-7. Rounding of Initially Pointed W Pins in UO_2 -W Composite Produced by Annealing at 1600°C for 15 Minutes. Scanning Electron Micrograph, X11,500.

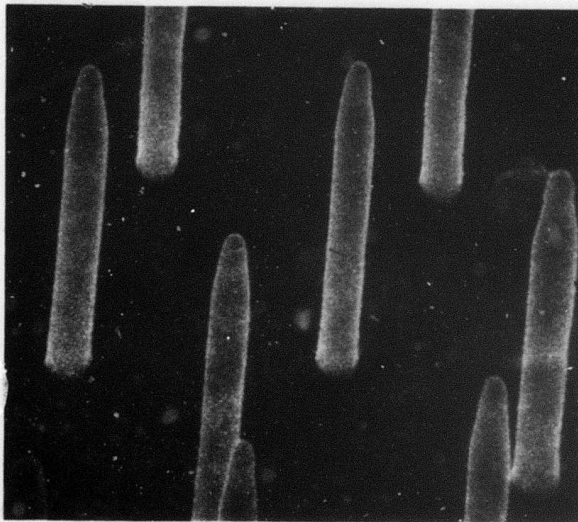


Figure III-8. Rounding of W Pins in UO_2 -W Composite Produced by Annealing of Pins at 1400°C for 25 Minutes. Scanning Electron Micrograph, X10,500.

composition was developed which attacked the matrix without affecting the W pins. This composition is:

20 ml	glacial acetic acid	matrix removal etchant
40 ml	saturated aqueous CrO_3 solutions	
6 ml	concentrated HNO_3	
4 ml	concentrated HF	

Initially a fresh batch of this etchant was carefully prepared and a UO_2 -W sample was etched for 30 minutes at 20 rpm at an etchant temperature of 22°C . The sample was prepared for etching by polishing on $1\mu\text{m}$ diamond and ultrasonic cleaning in acetone. A fiber length of $8-9\mu\text{m}$ was determined using the metallograph method described previously in this section. Four etchings in a period of eight hours using this same etchant batch gave nearly identical fiber lengths. Twenty-four hours later a fifth etching was performed using this same batch of etchant and virtually identical results were obtained.

Even after storage for eight days in a covered Teflon beaker at room temperature treating a sample with this batch of etchant produced exposed fibers 8 to $9\mu\text{m}$ in length. A few small areas in this sample had longer fibers up to $10\mu\text{m}$ long. A second batch of this etchant gave very similar results after storage for five days.

This set of experiments yielded two valuable pieces of information. First, it showed that the matrix removal etchant remained usable over longer periods of time than

previously suspected and that repeated use does not seem to affect the etching properties. Second, a UO_2 removal rate of $8-9\mu\text{m}$ per 30 minutes of treatment was established and used for the previously reported experiments in which the W removal rates were determined.

B. Gd_2O_3 -Mo EMITTING ARRAYS

During the past year the formation of optimum emitting arrays in the system CeO_2 doped Gd_2O_3 -Mo was studied. Work was conducted to expose and lengthen the Mo fibers, and to shape the fiber tips using chemical and thermal annealing techniques. The selective removal of Mo to form holes in the Gd_2O_3 matrix was accomplished, and the formation of recessed pin geometries was attempted. A notable result of this work was the determination of the relationship between fiber length, hole depth, and pin tip shape versus time of etching or annealing. These relations make possible the formation of many desirable geometries when certain parameters such as fiber length are specified.

In the selective removal of the Gd_2O_3 matrix to expose the molybdenum fibers, it was found that annealing samples prior to etching improved the uniformity of the etching and the smoothness of the oxide matrix. The high thermal gradients inherent in the zone melting technique appear to leave significant residual stresses in the matrix and annealing to 1800°C in a N_2 - H_2 atmosphere followed by slow cooling helped to remove

these imperfections and improve the uniformity of the etched samples. An unannealed Gd_2O_3 -Mo composite etched to expose the fibers is shown in Figure III-9 and the rough matrix is readily evident. This etching behavior can be compared with the subsequent pictures of the Gd_2O_3 -Mo samples all of which have been annealed prior to etching.

The etching of the CeO_2 -doped Gd_2O_3 -Mo components to expose and lengthen the Mo fibers was studied initially. Previous work¹ had shown that H_2SO_4 or a mixture of H_2SO_4 -12% methyl alcohol produced a relatively smooth oxide matrix with little if any attack of the Mo fibers. It was established that fibers $8\mu\text{m}$ long were formed by etching for 20 minutes, in reagent grade concentrated H_2SO_4 . A series of etching experiments were performed for time periods less than 20 minutes to determine the rate of oxide removal with time. In this work a single sample was reground and polished in the standard manner before each separate etch run, and fresh acid was used for each different time period. This was done to eliminate any etching variations due to sample differences and to limit the possibility of forming catalysts or inhibitors by reaction of the Gd_2O_3 and H_2SO_4 which might affect the etching rate in the subsequent tests. The height of the resulting fibers was determined by the metallograph method described previously. In making these measurements only a $0.5\mu\text{m}$ difference in fiber heights was found across the surface;

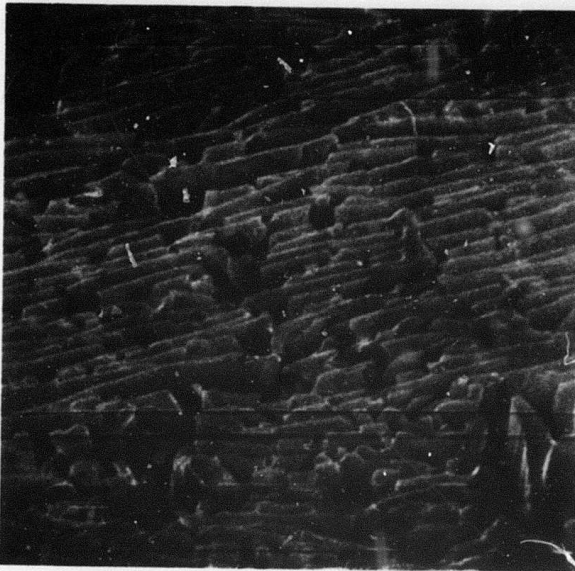


Figure III-9. Unannealed Gd_2O_3 -Mo Composite Etched to Expose Fibers. Scanning Electron Micrograph, X4,800.

the value for the fiber height was taken as the average of the maximum and minimum height values. Figure III-10 is a plot of fiber height versus etching time. A PDP-8e minicomputer was used to run a straight line and a parabolic regression on the data points. Data obtained from this analysis indicated that the rate of etching of Gd_2O_3 to expose Mo fibers more closely approximated a parabola than a straight line. This parabolic relationship, which deviates only slightly from a linear one, is considered accurate because of a "shielding" effect. As etching proceeded the fiber lengths increased, and the openings between the fine, closely spaced fibers begin to appear as tiny "channels" to the etchant. Fresh etchant must be transported down these channels to the oxide matrix and the spent etchant transported away for etching to continue at a steady rate. Reaction products formed by the reaction between the H_2SO_4 and the Gd_2O_3 become trapped at the bottom of the channels, retarding the etching by shielding the oxide surface from fresh etchants; this effect would become more pronounced as fiber length increased, resulting in a steadily decreasing etching rate. The same behavior was observed during the etching of holes (to be described later).

Two methods were investigated for shaping the molybdenum fiber tips to produce geometries suitable for electron emission testing. The first area studied the factors influencing the chemical pointing of the fibers and the second, the formation of hemispheres using annealing treatments.

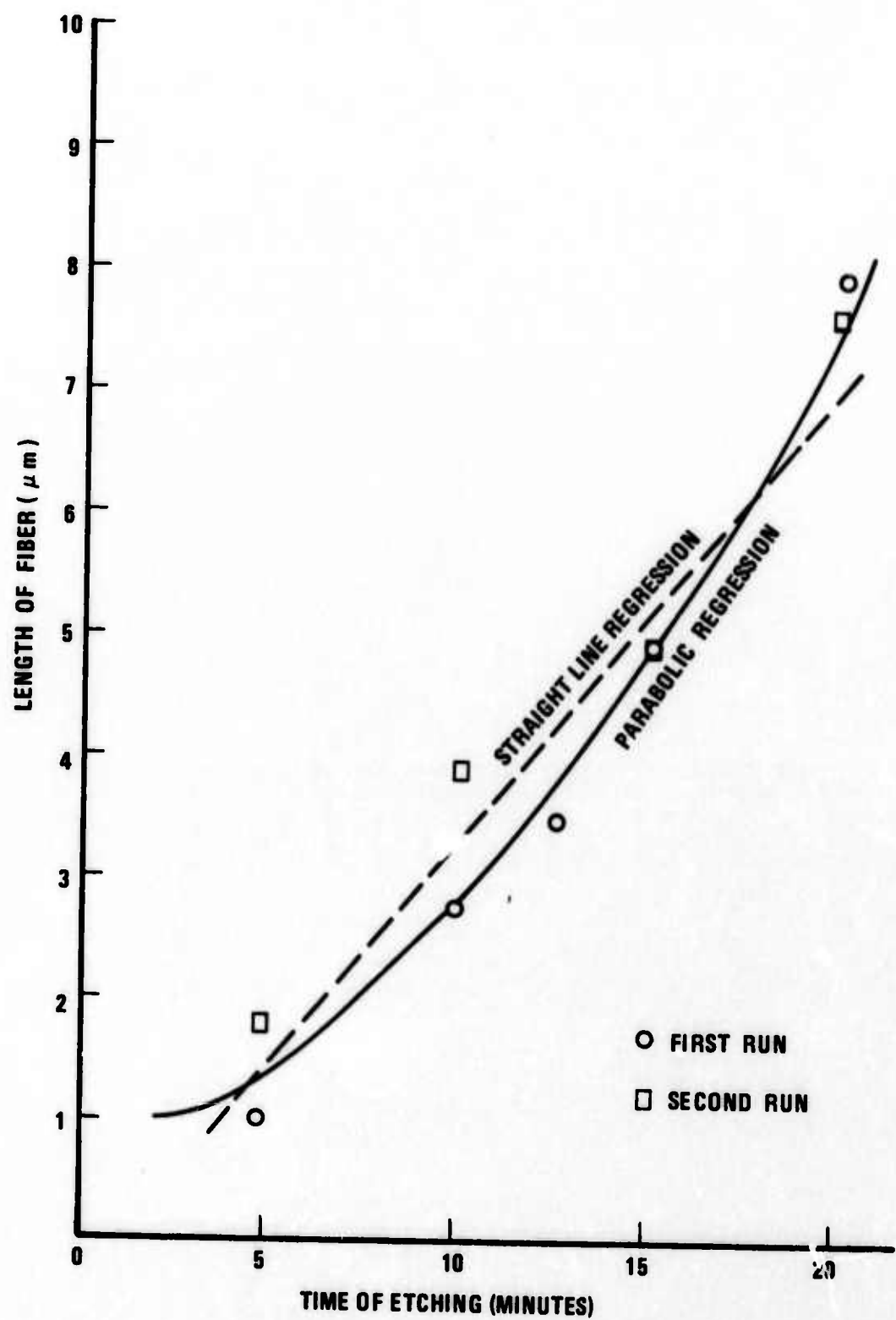


Figure III-10. Plot of Exposed Fiber Length vs. Etching Time for Gd_2O_3 -Mo Composite in H_2SO_4 -12% Methyl Alcohol Etchant.

Previous attempts to chemically point the Mo fibers¹ employed combinations of acids which attacked Mo; however, these etchants generally yielded poor, non-uniform structures. Additional etching work this reporting period centered around ammonia-based salt additions to H_2SO_4 and it was discovered that NH_4NO_3 additions produced exposed pointed Mo fibers. Figure III-11 shows a CeO_2 doped Gd_2O_3 -Mo sample etched by rotating at 20 rpm for 8 minutes in a solution consisting of 4 grams of NH_4NO_3 in 100 ml H_2SO_4 . In order to further improve pointing, a SONAC* device was employed to increase the etchant agitation beyond that obtained by routine sample rotation at 20 rpm. A Gd_2O_3 -Mo sample etched in the 4 gm NH_4NO_3 solution for 8 minutes, utilizing SONAC agitation in conjunction with rotation at 20 rpm is shown in Figure III-12. The overall improvement of fiber and matrix geometry is readily visible. The fibers are well pointed and uniform, and the matrix is generally quite smooth; the pin geometries were very uniform across the surface of the sample.

The effect of the addition of various quantities of NH_4NO_3 to 100 ml of sulfuric acid was also studied. It was found that the degree of pin pointing increased with the amount of NH_4NO_3 added. The matrix was rougher, however, as the NH_4NO_3 content increased. A solution of 5 grams of NH_4NO_3 in 100 ml of sulfuric acid was selected as an optimum pointing

*SONAC is the trade name of a small device marketed for the cleaning of dentures by electrosonic agitation.

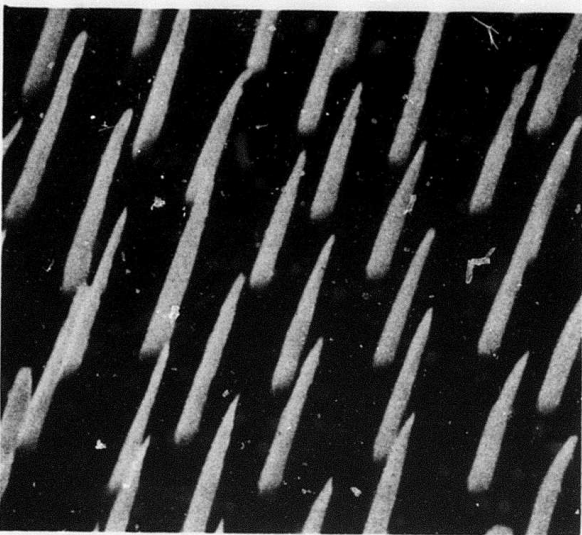


Figure III-11. Gd_2O_3 -Mo Composite Displaying Pointed Fibers Resulting from NH_4NO_3 Addition to H_2SO_4 Etchant. Etched by rotation at 20 rpm. Electron Micrograph, X11,700.

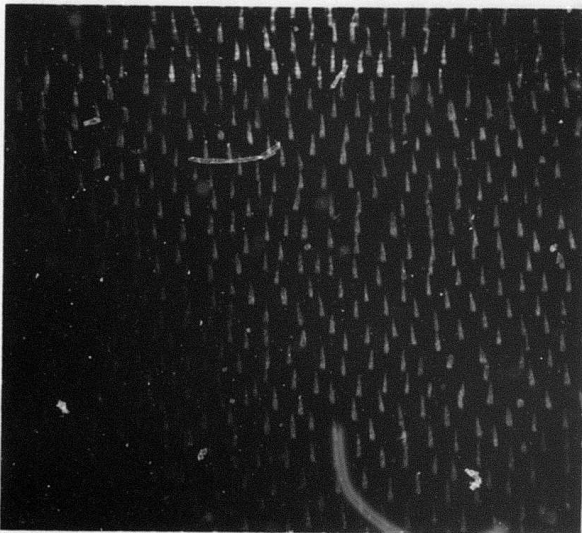


Figure III-12. Gd_2O_3 -Mo Composite Etched in NH_4NO_3 - H_2SO_4 Etchant Utilizing Rotation and Electrosonic Agitation. Scanning Electron Micrograph, X2,350.

etchant because it produced well pointed pins and an acceptably smooth matrix.

The second area of pin tip shaping studied the effect of various annealing treatments on exposed fibers in Gd_2O_3 -Mo samples. This study was concerned with finding the effects of both temperature and time on the shape of the fiber tips. Four of the better Gd_2O_3 -Mo specimens were selected as samples and the fibers were pointed in a solution containing 5 grams of NH_4NO_3 in 100 ml of H_2SO_4 by the ultrasonic-rotational method, followed by lengthening in concentrated sulfuric acid. The fibers approximated the shape of right circular cylinders with pointed tips. The overall length of the exposed fibers was about 5 μ m. Samples were induction heated to 1200 and 1600°C and held for 15 and 25 minutes in a H_2 atmosphere. The four samples were heated and cooled at identical rates and examined for pin tip shaping. The results indicated that a temperature of 1200°C for 25 minutes produced the best pin tip rounding (see Figure III-13). Annealing treatments conducted at 1600°C resulted in melting of the Mo fibers and deterioration of the oxide matrix surface.

The selective removal of the Mo fibers from the Gd_2O_3 -Mo samples to form holes was accomplished using an etchant composed of 75 grams $K_3Fe(CN)_6$, 25 grams NaOH, and 250 ml distilled water. The samples were suspended in the ultrasonic cleaner during etching to help force fresh etchant into the

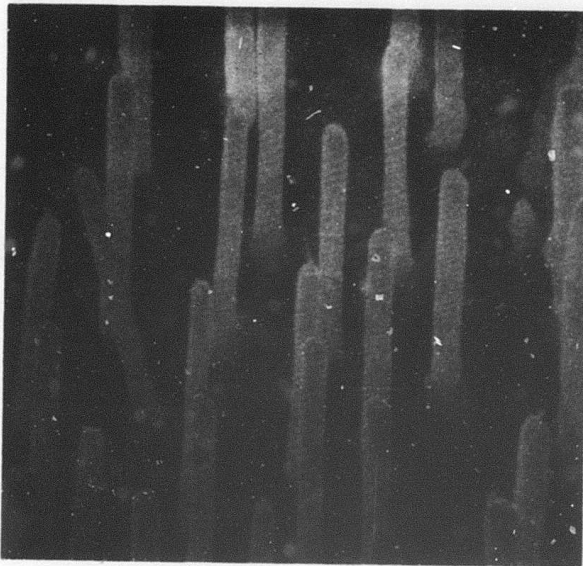


Figure III-13. Rounded Tip Shapes in Gd_2O_3 -Mo Composite
Produced by Annealing of Initially Pointed
Mo Pins at 1200°C for 25 Minutes. Scanning
Electron Micrograph, X12,200.

small holes and obtain increased hole depth. The rate of Mo removal to yield holes was determined using ultrasonic agitation and the known rate of Gd_2O_3 removal in H_2SO_4 (Figure III-10) by the procedure previously described in this section. A sample treated to form holes was placed in the standard fiber lengthening etchant to expose the fibers by removing a known amount of the gadolinia matrix. After cleaning, the length of the exposed fibers was measured. The depth of the hole was then the amount of Gd_2O_3 removed, in microns, (as determined from the etching time) minus the height of the exposed fibers. The results of this brief study are shown in Figure III-14.

The data shown in Figure III-14 was reduced in the same manner as the fiber length (matrix etching rate) data. Linear and parabolic regressions were run on the PDP-8e minicomputer. The linear fit had a correlation index of 0.994255. This indicated a good fit, but the parabolic fit had an index of 0.999875. This indicated that the relationship of hole depth to ultrasonic etching time was almost perfectly parabolic. The shape of the parabola indicated that the rate of etching slowed down with time. This behavior suggests there was difficulty getting fresh etchant into the holes; as the etching time increased and the holes got deeper the etching rate slowed down.

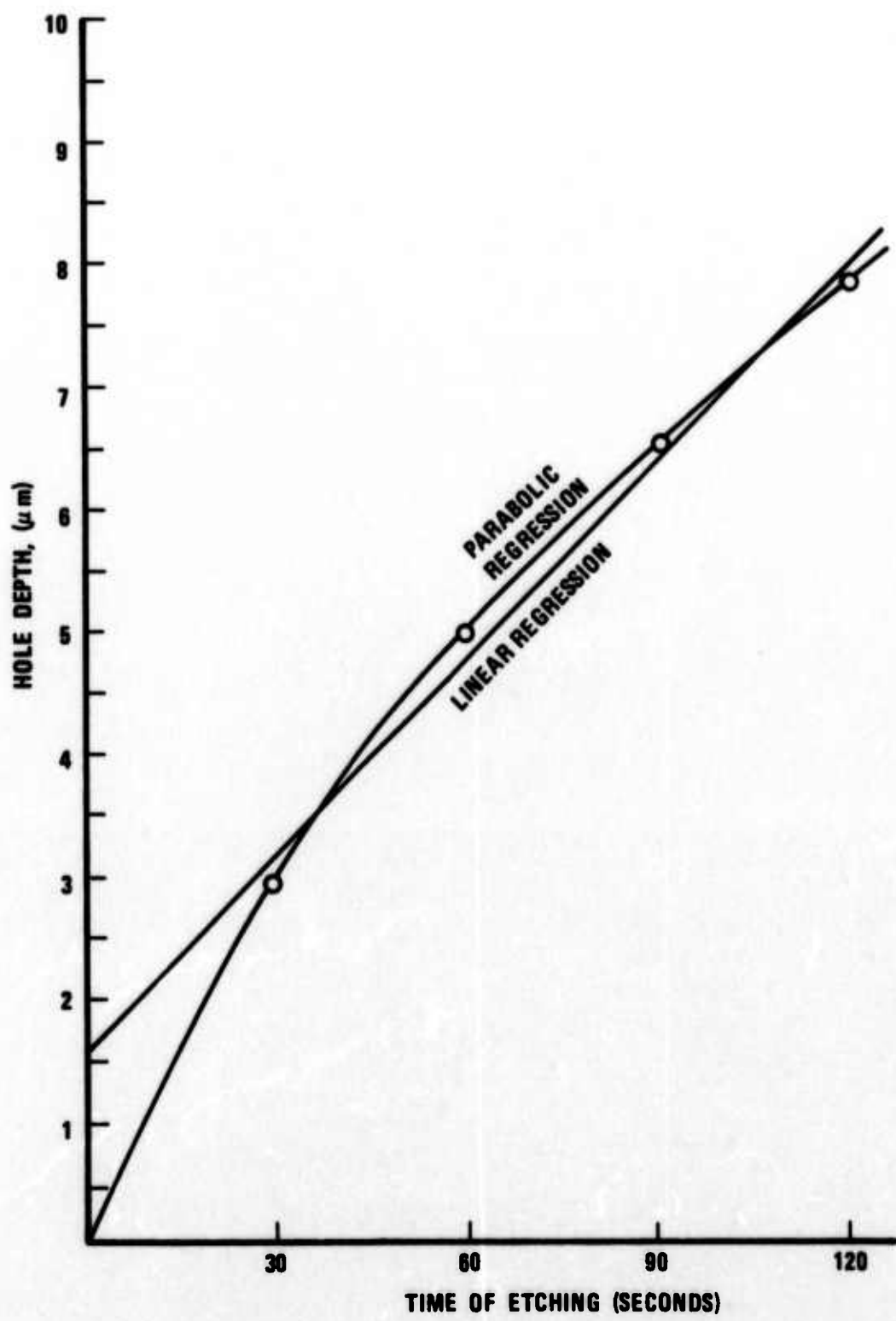


Figure III-14. Plot of Hole Depth vs. Etching Time for Gd_2O_3 -Mo Composite in $\text{K}_3\text{Fe}(\text{CN})_6$ -NaOH Etchant.

The etching of CeO_2 doped Gd_2O_3 -Mo samples to form pointed fibers recessed in holes was attempted using a two-step process. In the first step, shallow 2-3 μm deep holes were etched in the sample using the $\text{K}_3\text{Fe}(\text{CN})_6$ -NaOH solution. In the second step the pointing etch, composed of 100 ml H_2SO_4 and 5 grams NH_4NO_3 , was used in hope of pointing the fibers while only slightly etching the matrix. Initial experiments were performed with the time of hole formation and tip pointing equal to one another. Figure III-15 shows a sample prepared by this two step etch process. The holes are clearly visible, and some fibers are apparent in a few of the holes. The majority of the fibers do not appear to be pointed and structural uniformity is an obvious problem. Exposed fibers between holes are a result of matrix removal from around the originally recessed pins during the second etching. Holes which were initially deeper remain as depressions of various depths around the other pins. It is obvious that further work is required in this area to form recessed pin Gd_2O_3 -Mo samples suitable for electron emission testing.



Figure III-15. Gd_2O_3 -Mo Sample Showing Pointed Pins Recessed in Holes Produced by Two-Step Etching Process. Scanning Electron Micrograph, X1,000.

SECTION IV

OXIDE METAL COMPOSITE PROPERTIES

In previous reports^{1,2}, the objectives of this section have been (a) determination of fiber continuity and (b) establishment of electrical contact to the oxide-metal composites. Electrical resistivity measurements have been used to indicate degree of electrical contact and electrodeposits have provided estimates of fiber continuity. A summary of various electrical contact techniques and electrical resistivities will be reviewed in Section IV A. In addition, estimates of oxide-matrix resistivities will be presented.

From electrodeposits of copper, SEM micrographs showed that roughly 70% of the fibers in the oxide-metal composites are continuous with the discontinuities occurring¹ in the region of cell boundaries. Correlation of fiber continuity to electron emission was demonstrated using electrodeposits.¹

Thin films of various types have been deposited using an ion beam coater.* The arrival of the coater allowed investigation of the effect of front surface conductive coatings, and back surface resistive coatings on field effect electron emission. Details of the ion beam apparatus and coatings will be reported in Section IV B.

*Ion Beam Coater (A modified IMMI III), Commonwealth Scientific, Arlington, Virginia.

A. ELECTRICAL RESISTIVITIES

During the initial stages of testing the field effect emission of UO_2 -W composites, electrical contact to the composite was provided with silver paste.^{3,4,5} Electrical resistivities of oxide-metal composites utilizing silver paste contact were of the order of 10^3 ohm-cm, indicating little contact to the individual metal fibers as this value is representative of the UO_2 matrix.² In an effort to improve electrical contact, metal vapor deposits, silver solder, and brazes of platinum and copper have been investigated.^{1,2} The resistivities measureable with the various contact methods are presented in chronological order in Table IV-I. Details of measurement techniques have been reported previously.¹ It should be noted that the resistivities were calculated on the basis of the volume of metal in the composites and the lowest obtainable resistivities is that of the metal or 6×10^{-6} ohm-cm. Since it was shown that 30% of the fibers are discontinuous, the lowest measureable value would be 8.5×10^{-6} .

Note from the chronological order of the contact methods in Table I that contact has consistently improved as indicated by decreasing resistivities. It is significant that emission electron current density has also greatly increased as contact improved. Electrical contact is not the only factor for improved emission density but certainly is a contributing one. Indium and mercury electrical contacts were used for resistance

TABLE IV-I

SUMMARY OF LOWEST OXIDE-METAL COMPOSITE RESISTIVITIES
PRODUCED BY VARIOUS CONTACT METHODS

Contact Method	Composite Material	Lowest Resistivity (ohm-cm)
Silver Paste	UO_2 -W	10^3
Indium	UO_2 -W	10^{-4}
Mercury	UO_2 -W	Not Reproducible
Gold Vapor Deposit	ZrO_2 -W	1.4×10^{-3}
Silver Solder Braze	UO_2 -W	6.0×10^{-4}
	Gd_2O_3 -Mo	2.6×10^{-3}
Copper Braze	UO_2 -W	1×10^{-4}
	Gd_2O_3 -Mo	2.2×10^{-4}

measurements only as their vapor pressures prohibit use in electron emission testing.

For low voltage electron emission using a sample geometry of recessed pins with a conductive front surface coating, a high resistance matrix is desirable. To estimate the resistance of the matrix, a series of experiments were conducted on the same UO_2 -W composite (Sample No. 31-12-2/20-24). The initial sample geometry of an exposed cylindrical pin composite, copper brazed to a molybdenum pin, was coated with gold in the ion beam coater. When measured with indium contact to the front surface gold coating, the sample has a resistivity of 1.2×10^{-4} ohm-cm based on tungsten content, Table IV-II. The sample was polished flat and pins were recessed 3-5 microns below the surface. With indium contact to the front surface, the resistance was 2.5 ohms. Assuming the hole depth to be 5 microns and the total resistance drop was across the 5 microns of UO_2 between the top of the pins and the indium, the matrix had a resistivity of 1.4×10^3 ohm-cm. This is a reasonable value for nonstoichiometric UO_2 . When pressure was applied to make contact, the indium flowed into cracks on the sample surface and possibly into the holes left by the removed pins. After gold coating this sample in the ion beam coater and remeasuring the resistance, the resistance dropped from the previous value of 2.5 ohms to 4.8×10^{-1} ohms. The drop may have resulted from gold deposited in the holes.

TABLE IV-II
COMPOSITE MATRIX RESISTANCE MEASUREMENTS

Sample	Geometry	R (ohms)	ρ (ohm-cm)
UO ₂ -W	Exposed Pin-Gold Coated	6 x 10 ⁻³	1.2 x 10 ⁻⁴ a
	Recessed Pin	2.5	1.4 x 10 ⁺³
	Recessed Pin-Gold Coated	4.8 x 10 ⁻¹	2.7 x 10 ⁻² b
		Slice No.	Slice No.
		(4)	(5)
		(4)	(5)
$(Gd_2O_3-20\%)$ (CeO_2-Mo)	Exposed Pin	3.0 x 10 ⁻³	2.2 x 10 ⁻⁴ c
	Recessed Pin	5	23.6 1.2 x 10 ³ d
			5.8 x 10 ³ d

a = calculated on basis of tungsten present

b = calculated on basis of 5 microns UO₂ thickness

c = calculated on basis of molybdenum present

d = calculated on basis of 8 microns Gd₂O₃ thickness

However, there is the possibility that indium flowed further into the cracks on remeasurement and established contact with more of the tungsten fibers. SEM examination of the gold surface showed no evidence of holes, indicating either gold had bridged open holes or indium had been forced into them during resistance measurements.

A similar series of resistance measurements was conducted on Gd_2O_3 -20% CeO_2 -Mo composite, Sample No. 22-89/30-18/20-26, slices 4 and 5. The initial resistivity of both slices was 2.2×10^{-4} ohm-cm, Table IV-II. After the Mo fibers had been recessed to 8 microns below the surface, the resistivity of the matrix between the end of the pins and the indium contact was calculated to be 1.2×10^3 and 5.8×10^3 ohm-cm for slices 4 and 5 respectively. Thus, the resistivity of the Gd_2O_3 -20% CeO_2 matrix appears to be approximately the same as that of the UO_2 matrix. Once again, the matrix was cracked and the resistance values must be viewed with caution. It is believed that a crack-free matrix would exhibit a much higher resistivity, since any electrical contact through a crack would change the resistance orders of magnitude.

B. THIN FILMS

Ion beam sputtering has been used to deposit thin films of both metals and oxides on the UO_2 -W and Gd_2O_3 -Mo composites. Using a beam of ions, an atom or small group of atoms is removed from a selected target material and collected on a substrate near the target. If the ion source is an inert gas such as

argon, a metal or alloy may be deposited. Reactive sputtering may be accomplished through the use of an active gas such as oxygen. For example, using copper as the target material, copper metal can be deposited with argon and cupric oxide can be deposited using oxygen.

After receiving an ion beam coater in January 1973, several modifications were made to improve control over deposition rate and uniformity of film thickness. These modifications will be described in the Apparatus and Calibration Section.

Using the ion-beam coater, thin films of Pt, Au, Mo, W and amorphous $\text{Al}_x\text{Si}_y\text{O}_z$ have been deposited on the composites to serve at different times as electrical contact on the back side of emitters, as a continuous metallic coating on the front side, and as a series resistor on the back side of emission test samples. The thin films and their morphologies will be discussed in the Coating Studies Section.

1. Apparatus and Calibration

The ion beam coater consists of an ion gun focused on a target in a vacuum chamber operating between 1×10^{-4} and 5×10^{-4} torr. The ion current was initially measured by inserting a probe approximately 1 cm in front of the ion gun. Ions impinge on the target removing atoms or groups

of atoms and the deposit atoms are collected below the target on a desired substrate, Figure IV-1. Up to six different targets may be utilized sequentially in a hexagonal rotatable target holder. Ion currents up to 500 μ a have been achieved at gun voltages between 6 and 10 KV. Rotation and translation of the sample stage was provided to allow uniform deposition over a 3 cm diameter area.

Initial studies with the ion beam coater were made to estimate deposition rates at constant ion-beam currents and ionization voltages. Molybdenum was deposited using argon as the ionized gas at a pressure of $4-5 \times 10^{-4}$ torr, and film thickness was determined using x-ray absorption. Molybdenum deposition rates on polycrystalline alumina substrates were not reproducible for these tests, Table IV-III. Variations in deposition rates under constant conditions is now thought to have been due to a charge build up on the molybdenum target as explained below. Variations were also produced by changing beam currents during deposition.

Some causes of the deposition rate variations were discovered when reactive sputtering was attempted using oxygen as the ionized gas. Using a copper target, it was anticipated that copper oxide would be deposited on a 5 mil platinum sheet. A black film (presumed to be some form of copper oxide) was deposited initially and as deposition

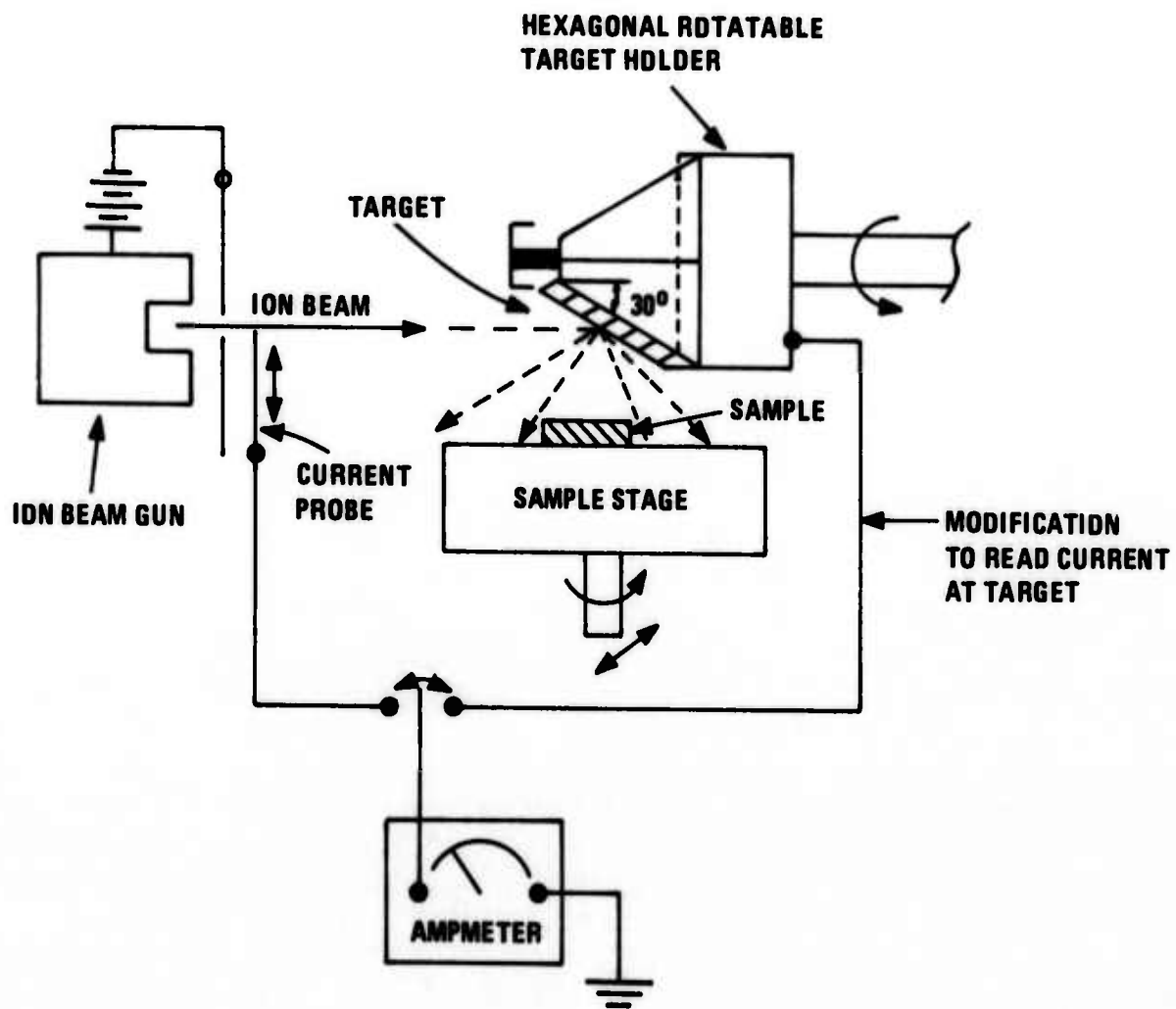


Figure IV-1. Schematic of Ion Beam Coater

TABLE IV-III

MOLYBDENUM DEPOSITION RATES PRIOR TO
MODIFICATION OF THE ION-BEAM COATER

<u>Deposition Time, min.</u>	<u>Ion Beam Current (Microamperes)</u>	<u>Ionizing Potential (KV)</u>	<u>Coating Thickness Å</u>	<u>Deposition Rate Å/min.</u>
5	100	6	34	6.8
60	100	6	820	13.7
120	100	6	750	6.2
120	200	9	2790	23.2

proceeded, copper metal appeared. During deposition the gun current varied considerably and the current was seen (visually, by looking at the beam) to decrease when the current measurement probe was removed from the beam. Thus, the ion current during deposition was not known and since the deposit seemed to vary in stoichiometry with time, it was thought that the ion beam was charging the copper target which changed operating conditions as a function of time. It was discovered that the target holder was electrically insulated, allowing charging of the target. The target was grounded by connecting the holder to a microampmeter (in addition to the current probe micrometer). This not only grounded the target but provided a continuous reliable reading of the ion-beam current at the target. With this new arrangement, beam current became more easily controlled and remained steady over long periods of time. A run was made using oxygen with a copper target and the deposited coating (on platinum) was black and proved to be cupric oxide.

To allow monitoring of coating thickness as deposition occurs, a new sample stage was constructed with a Sloan Vibrating Quartz Crystal thickness monitor head serving as the center of rotation for the stage, Figure IV-2. An eccentric cam provided rotation and translation of the stage perpendicular to the ion beam of 5/8". Four samples

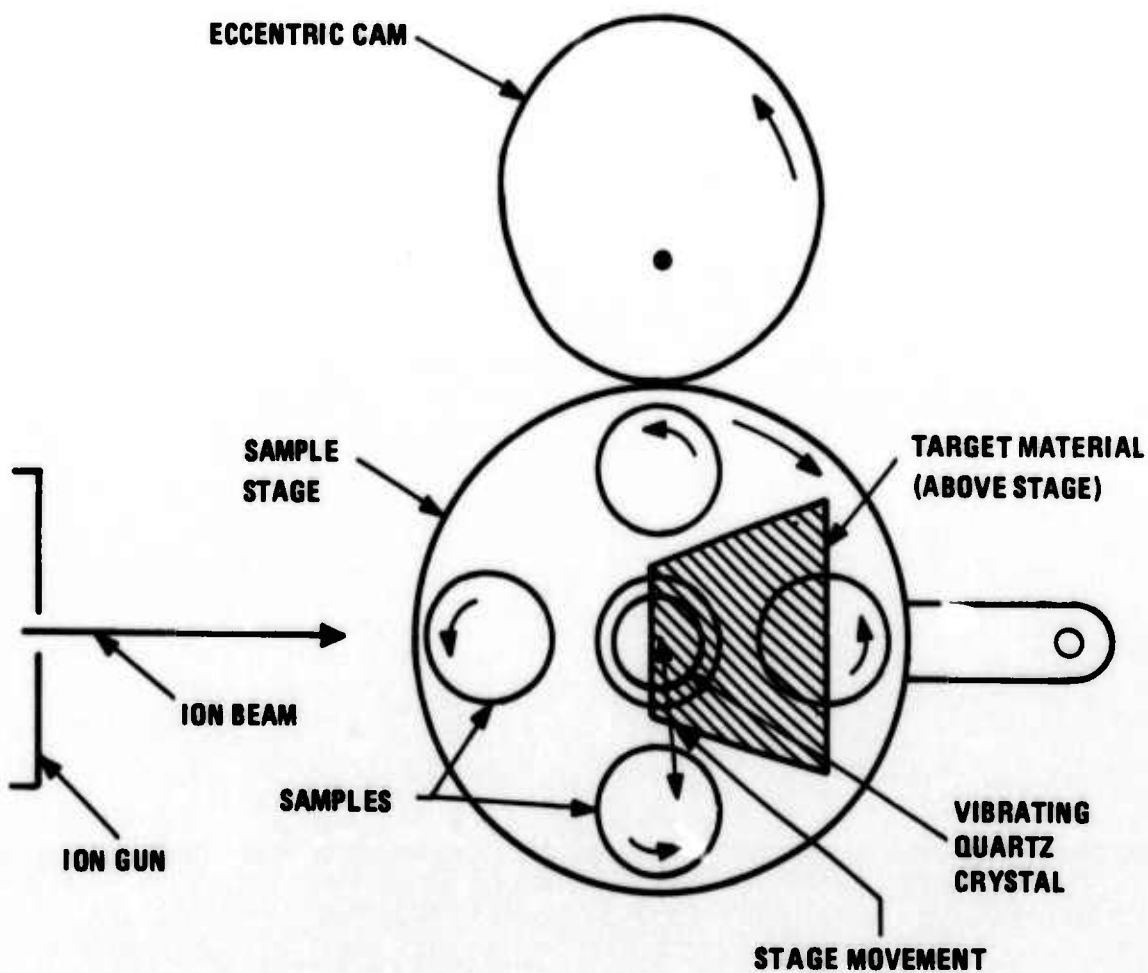


Figure IV-2. Diagram of Ion Beam Coater Stage Utilizing Vibrating Quartz Crystal Thickness Monitor.

could be positioned on a concentric circle about the quartz crystal. In addition, each sample rotated on its own axis with respect to the stage. The various motions allowed uniform deposition since samples "viewed" the depositing material at a wide variety of angles.

To calibrate the frequency change of the quartz crystal as a function of deposit thickness at the sample position, tungsten was deposited on two pieces of Al_2O_3 substrate. At an ion beam current of 50 μa and ionization voltage of 9 KV, the frequency of the quartz crystal varied linearly with time. After two hours, the film thickness on the two alumina samples was $800 \text{ \AA} \pm 10\%$ as measured by x-ray transmission. During deposition a frequency change for the quartz crystal of 14,000 Hertz was recorded. The thickness monitor manufacturer stated that deposit thickness may be approximated by $T = \Delta f / \rho$, where T is the thickness in anstroms, Δf is the frequency change in Hertz during deposition and ρ is the density of the deposit in gm/cm^3 . Thus, using a density of 19.3 for tungsten, the calculated thickness was 725 \AA or within the accuracy of the measurements made by x-ray transmission.

The dependence of deposition rate on ion beam current and ionization voltage was investigated and it was found that the deposition rate was strongly dependent on ion beam current and less affected by voltage. Results of this investigation are shown graphically in Figure IV-3. At a voltage of 9 KV the deposition rate (in Hz/min at the crystal)

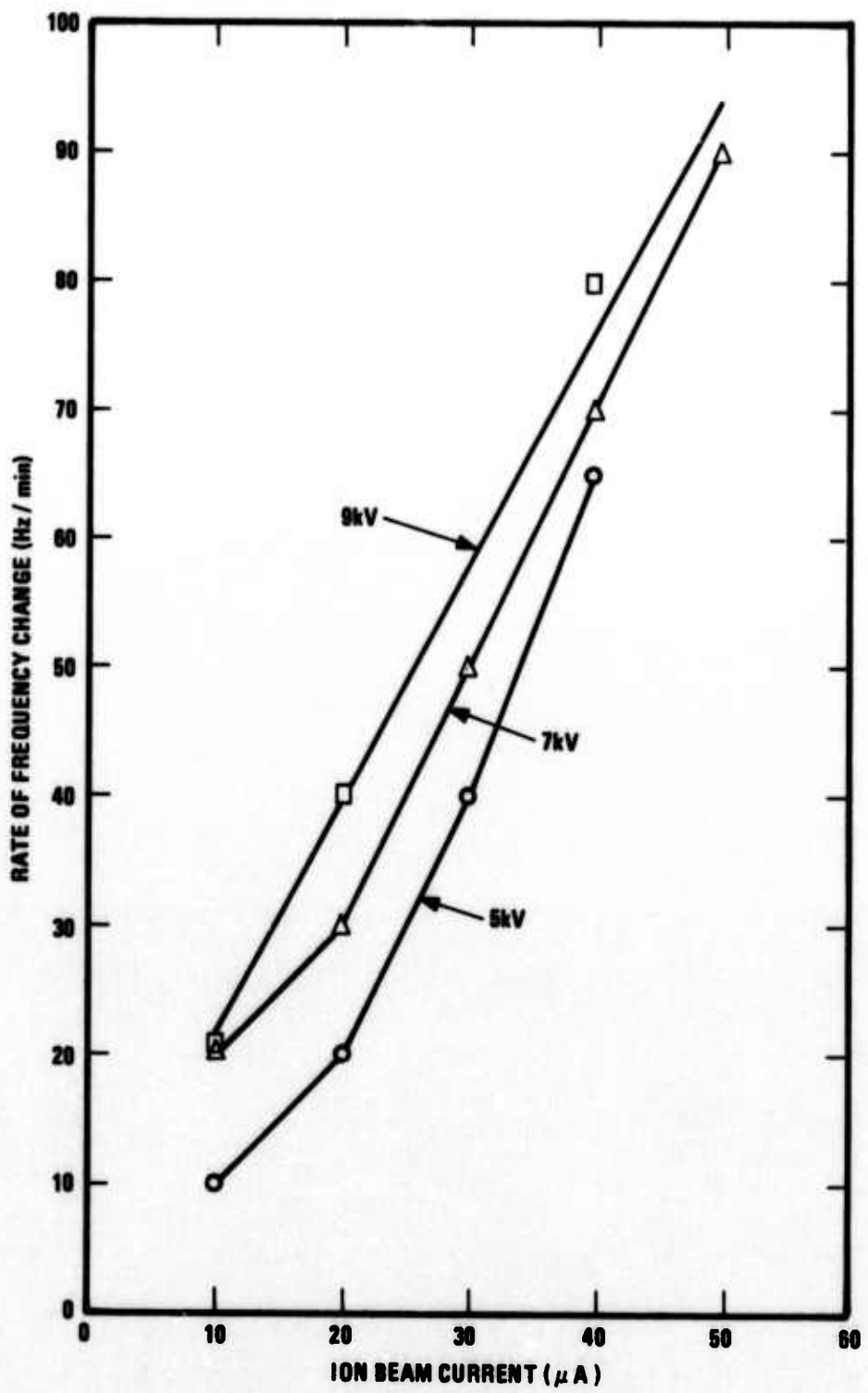


Figure IV-3. Effect of Ion Beam Current and Accelerating Potential on Deposition Rate of Molybdenum

was 20 Hz/min at 10 μ a and increased to 80 Hz/min at 40 μ a. At 30 μ a the deposition rate varied from 20 Hz/min to 40 Hz/min as the voltage was increased from 5 KV to 9 KV. These deposition rates are relative only, as the stage was stationary.

2. Coating Studies

a) Front Surface Contact

Previous evidence suggested emission current was probably produced by a relatively small percentage of the metallic pins operating at any given time.^{1,2,3} In an effort to increase emission current uniformity and density, front surface metallic coatings were deposited on exposed pin composite samples to provide equivalent electrical contact to all pins.

An initial 1000 \AA thick gold coating was deposited on UO_2 -W composite, Sample No. 31-12-1, Figure IV-4. Good uniformity and smoothness of the gold over the entire sample surface was encouraging. The sample was rotated as usual and deposition occurred at a wide variety of angles. Interestingly, the pins that were initially cylindrical exhibited a conical geometry after deposition, with the base diameter larger than the end diameter. This behavior suggested that ion beam deposition might be used to taper and uniformly round pin tips.

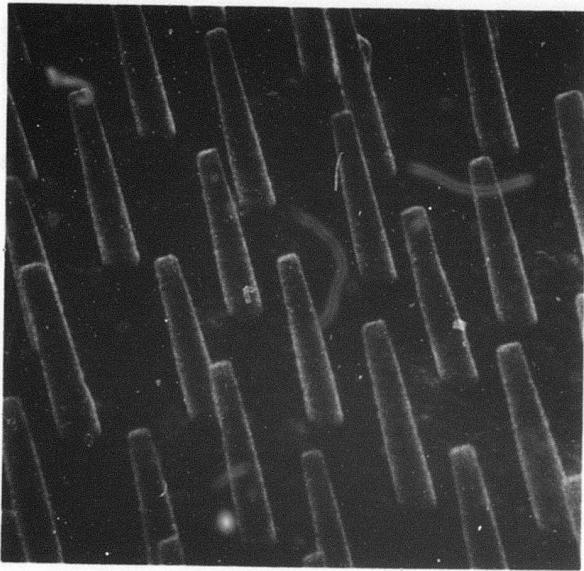


Figure IV-4. Scanning Electron Micrograph of 1000 \AA°
Gold Deposit on $\text{UO}_2\text{-W}$ Sample No. 31-12-1,
X6,400.

On UO_2 -W Sample, No. 25-59-10/23-43b, a 1000 \AA film of Mo was deposited which showed even more rounding of pin tips than was seen in Sample No. 31-12-1 (Figure IV-4). A micrograph of the sample prior to deposition is shown in Figure IV-5 and micrographs after deposition are shown in Figures IV-6, 7 and 8. By comparison with the gold coating, the Mo deposit tapered the pins near the tips and rounded the ends. Several unusual effects were seen. In some areas of the sample, the deposit formed "collars" approximately in the middle of the fiber lengths, Figure IV-7, and in other areas, flat sheets of molybdenum branched out from the fiber tips, in some cases forming a bridge connecting the fibers, Figure IV-8.

Due to the success of applying smooth front surface metallic coatings to composite samples with exposed pins, two coated UO_2 -W samples were emission tested. The first sample (No. 25-66-7/113-31Y/58) was initially emission tested without any front surface coating and, after coating with gold, the measured emission current increased two orders of magnitude at low applied voltages. Post emission examination of the gold coated pins showed areas where the gold had been vaporized or removed from the pins and the more stable (lower vapor pressure) metal Mo was selected for the next sample. The second UO_2 -W sample (No. 31-39-8/30/20-33/62) was coated with 1000 \AA of Mo. The coating was uniform, Figure IV-9, and

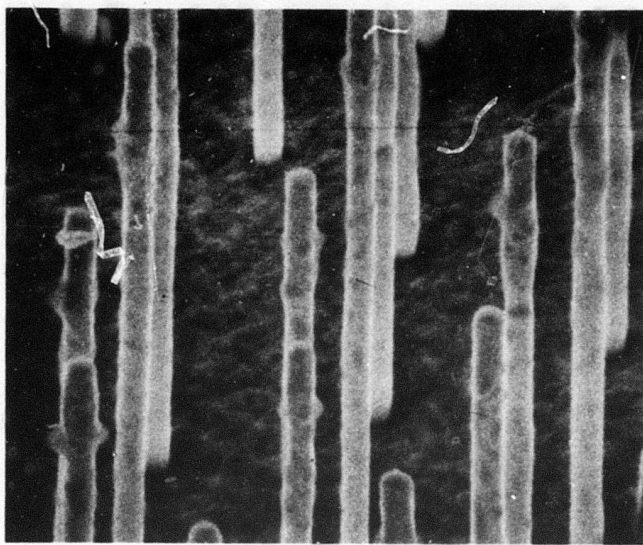


Figure IV-5. Scanning Electron Micrograph of UO_2 -W
Sample No. 25-59-10 Prior to Molybdenum
Deposition, X10,000.

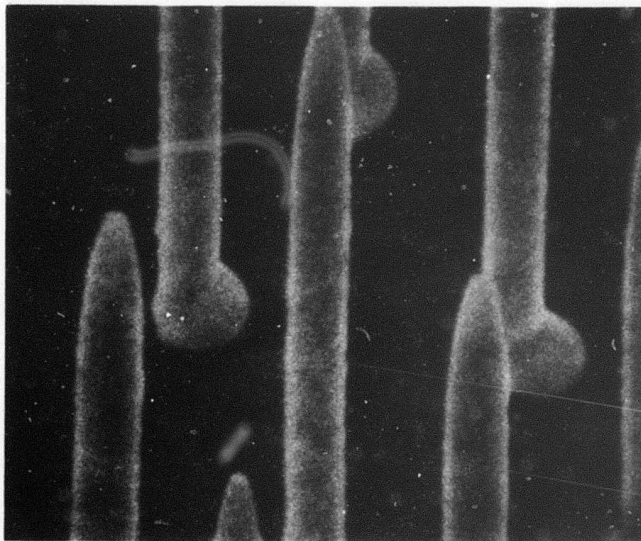


Figure IV-6. Scanning Electron Micrograph of UO_2 -W
Sample No. 25-59-10 Coated with 1000 Å
of Molybdenum Showing Rounded Pin Tips,
X11,000.

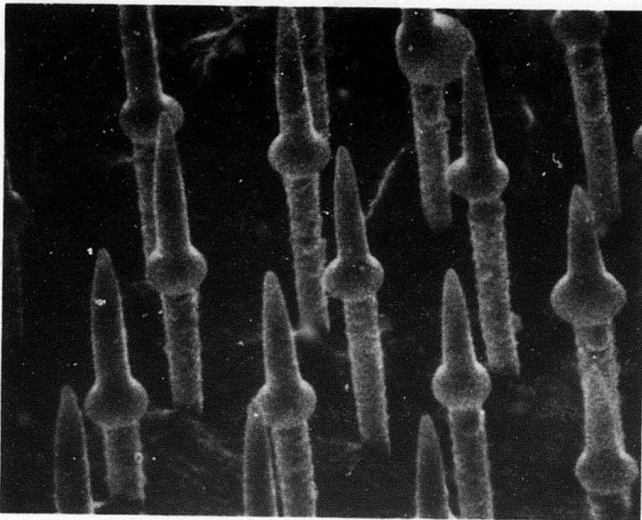


Figure IV-7. Scanning Electron Micrograph of $\text{UO}_2\text{-W}$ Sample No. 25-59-10 Coated with 1000 \AA of Molybdenum Showing "Collar" Deposits, X5,700.

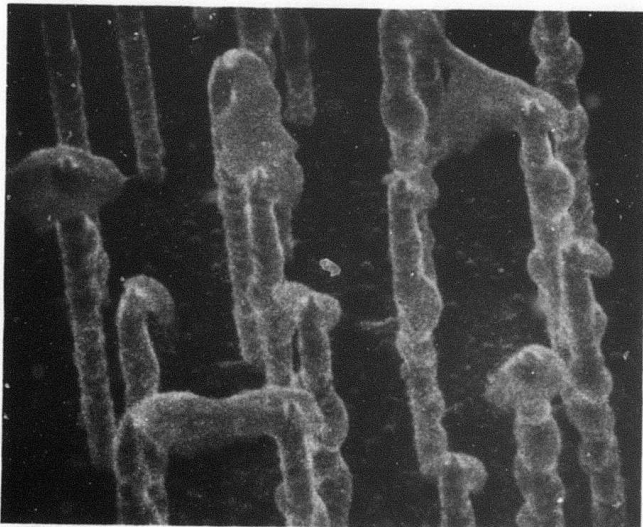


Figure IV-8. Scanning Electron Micrograph of $\text{UO}_2\text{-W}$ Sample No. 25-59-10 Coated with 1000 \AA of Molybdenum Showing Deposit Sheets On Fiber Ends, X5,700.



Figure IV-9. Scanning Electron Micrograph of UO_2 -W
Sample No. 31-39-8/30/20-33/62 Coated
with 1000 Å of Mo Prior to Emission
Testing, X25,500.

emission testing resulted in a high gross current but modest current density because of the large sample area. The details of the emission testing of these samples are presented in Section V-B-1 of this report.

b) Front Surface Anode

To determine if a metallic coating would fill holes in a composite sample with recessed pins or if only the matrix would be coated leaving open holes, a platinum coating was deposited on a recessed pin UO_2 -W composite, Sample No. 25-61-3/11-66/23-29 (sample geometries of this type are desirable for low-voltage electron emission, with the coating acting as the accelerating anode). Prior to deposition, half the sample was masked with copper foil to have a direct comparison of the platinum coated surface with the uncoated surface. After two hours of deposition using argon as the ion beam, the Pt coating partially separated from the composite substrate on removal from the ion beam coater. SEM examination showed the coating to be $\approx 1800 \text{ \AA}^{\circ}$ in thickness and to contain holes slightly smaller than the holes in the uncoated matrix, (Figure IV-10). Thus, such a technique might be useable to produce a front surface anode. However, to effectively use such an anode, a composite with a high resistance matrix would have to be developed.

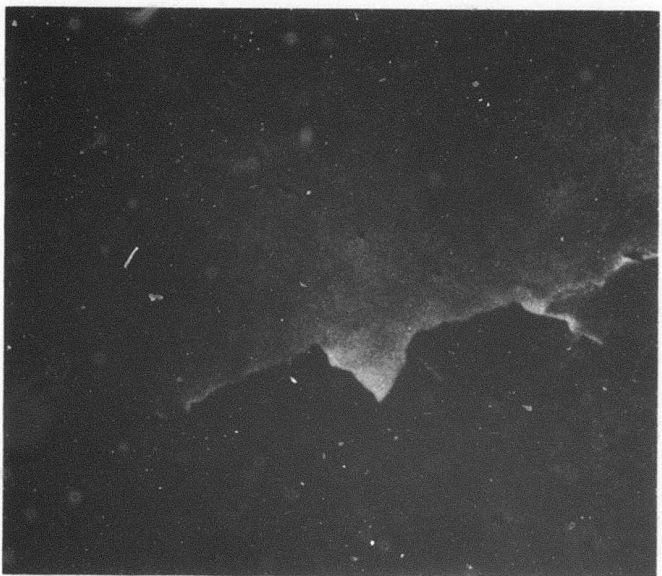


Figure IV-10. Scanning Electron Micrograph of 1800 Å Platinum Coating Deposited on Recessed Pin Composite Showing Holes Remaining After Deposition, X5,150.

c) Back Surface Series Resistors

In a previous report² the advantages of a resistance in series with each pin was discussed as a means of improving the emission per pin characteristic of the composite samples. In an effort to experimentally verify this behavior, a semiconductor oxide film was deposited on the back of a sample to produce a series resistor for each pin of 10^8 - 10^{10} ohms. Such a resistor should give a uniform resistance for each continuous pin and limit the emission current of each pin, thereby reducing the probability of a pin "burning out."

An aluminum alloy (6061 - = 96% Al + Si, Mg, Mn, Cr, Au, Zn, Ti) was bombarded with ionized oxygen to produce optically transparent films between 1000 and 2000 \AA thick on various substrates. To determine the resistivities of the $\text{Al}_x\text{Mg}_y\text{Si}_z\text{O}_n$ films, 0.5 inch discs of duminum were polished to a 1 μm diamond finish and coated with the amorphous "alumina" films. On top of the alumina films, a 0.2 μm by 0.25 inch diameter circle of gold was deposited for electrical contact and to define the conducting area of the alumina. Resistance was measured using indium contact to the gold. The resistivities of a 1000 \AA thick $\text{Al}_x\text{Mg}_y\text{Si}_z\text{O}_n$ film deposited on two aluminum discs were 2.2×10^5 and 3.5×10^5 ohm-cm. Using a resistivity of 2.9×10^5 ohm-cm, a resistor 2000 \AA thick with a diameter of 0.3 μm (typical of the tungsten fibers) would have a resistance of 8.3×10^9 ohms.

For emission testing, an exposed fiber UO_2 -W composite was coated on the back surface with 2000 \AA° on the alumina resistor, over coated with 2000 \AA° of gold 0.25 inches in diameter, and silver pasted to a 0.375 inch diameter molybdenum pin. The sample was emission tested (as reported in Section V) and displayed better stability than typical samples but the hoped for current characteristics were not observed.

SECTION V

EXPERIMENTAL EMISSION MEASUREMENTS

This section discussed the experimentally observed high field electron emission characteristics of the oxide-metal composite materials. The main emphasis of experimental work accomplished during the present period was directed toward the evaluation of various overcoating techniques, unusual emitter geometries, and the effect of pin height and shape on the emission. For the most part, this work was accomplished using the water cooled test diode described previously.¹ In addition a demountable ¹ diode was in continuous operation and a second long-term diode was constructed.

In order that this Final Report be as complete as possible, a short summary of the most significant results previously presented is given along with a detailed description of the work performed since the last report. A description of new experimental apparatus is given and the most significant of the experimental results are discussed.

A. SUMMARY OF PREVIOUS EXPERIMENTAL WORK

During the three year term of this program, approximately fifty different oxide-metal composite emitters have been electrically tested in over sixty experiments. The majority

of these experiments were performed with emitter test diodes mounted in a cross-shaped vacuum chamber. This vacuum system, which has been described previously in detail⁴, operates with a base pressure of less than 10^{-9} Torr. Test diode configurations utilized with the chamber included: (1) fixed spacing radiation cooled diode⁵, (2) variable spacing conduction cooled diode⁴, (3) segmental collector radiation cooled diode³, and (4) water cooled fixed spacing diode.¹ Each of the diodes was constructed so as to be mounted interchangably in the vacuum system. A Sorensen model 2012-250 power supply was used for dc emission tests, a plate transformer for 60 Hz ac tests and a 3kV hard tube pulser for pulsed measurements. During continuous duty testing, a series resistance of 10^4 - 10^7 ohms was usually employed to limit peak current through the emitter should a breakdown occur.

Initial emission measurements were made with the fixed spacing radiation cooled diode and the variable spacing conduction cooled diode. Current densities of 50 - 100 mA/cm² were obtained. A silver paste material was used to attach the emitter wafer to the cathode support structure. Scanning electron microscope analyses of the post-emission emitter wafers revealed areas of localized pin melt down, often single isolated pins being destroyed. By the use of the variable spacing diode, the relationship between the emitted current J and the interelectrode

spacing L ,

$$J = C_1/L^2 \exp(-C_2 L),$$

where C_1 and C_2 are constant, was empirically verified.⁴

The segmental collector diode established that areas of high emission from a wafer were strongly correlated with good wafer morphology and perturbations such as slightly non-parallel electrodes were of a second order nature.³ Consequently, efforts were directed toward the production of the best possible emitter morphology and verification of such with pre-emission scanning electron micrographs.

Most of the early emission samples were produced from the UO_2 -W composite materials with exposed emitter pins. The variable spacing diode was used to examine the relative performance of emitters having exposed and flush pins.³ It was found that flush pin emitters produced several orders of magnitude less emission current for the same anode potential as did the exposed pins. In addition to flush pins, other unique geometries were tested including wafers with recessed pins and slightly exposed pins. Other composites including ZrO_2 -W and Gd_2O_3 -Mo were investigated and found to have certain advantages such as higher resistivity matrix and ease of handling, but gave emission inferior to that obtained with the UO_2 -W materials.

Concern over possible discontinuities in the emitter pins led to the development of an electrochemical plating technique which revealed the extent of pin continuity.² It was found that areas of good pin continuity tended to coincide with those areas having higher emission. After this investigation, electrical resistivity of wafers was measured and verified to be low (indicating good pin continuity) before initiation of electron emission tests.

As indicated above, a silver paste material was initially used to fasten the emitter wafers to a cathode support structure. This practice was followed for about the first third of the experiments. After that time, a braze, usually copper, was utilized in sample mounting. The use of this braze provided improved contact with the emitter pins and improved emission. Greatly enhanced reproducibility of emission data and a general increase in average emission current was attributed to the braze. About this same time the bakable, water cooled diode was first used. This diode had precisely controlled spacing and was water cooled. It eliminated the problems encountered previously due to electrode heating and attendant changes in interelectrode spacing.

The demountable diode utilized in the long-term test program was described in the last report.¹ Briefly, it is a glass and stainless steel structure pumped with an ion pump and operating with pressures in the low 10^{-9} range. Data from this diode are given in the present report.

B. ELECTRON EMISSION MEASUREMENTS

A chronological summary of the emission data together with important emitter characteristics for all samples tested since the last report is given in Table V-I. Experiments undertaken in this period have generally been more complex and sophisticated than those previously attempted. All but several specialized tests were performed using the water cooled constant spacing diode assembly. Attachment of the samples to the cathode assemblies was done with a copper braze or silver paste. The samples employing silver paste were first coated with gold. Such procedures provided reliable contact between the emitter pins and the cathode support.

Experiments conducted during this period can be divided into seven categories: (1) use of metallic overcoatings to change and enhance emission; (2) use of annealing to improve pin tip geometry; (3) construction of low-voltage electron gun assemblies; (4) long-term emission life testing; (5) continued development of high current emitters; (6) emission experiments with composites other than UO_2 -W; and (7) application of resistive coatings to improve emission stability. Material relevant to each of these groupings will now be discussed.

TABLE V-1
CHRONOLOGICAL SUMMARY OF EMISSION EXPERIMENTS

Installation Date	Pumpdown No.	Sample Designation	Type of Composite	Emitter Configuration	Maximum Current Density ma/cm ²	Active Emitter Area cm ²	Remarks
12-18-72	47	25-49-8/113-19/47	UO ₂ -W	Short pins with sharpened fiber tips.	10	0.3	Testing terminated by Power Failure
1-6-73	48	22-47/48,49	Gd ₂ O ₃ -Mo	Re-etched sample of Pumpdown No. 46 Short, blunt Pins	-	0.3	
1-13-73	49	Same as Pumpdown 48			20	0.3	Short pins, high density
1-26-73	50	113-25/23-29/50	UO ₂ -W	Pointed pin tips - high pin density	-	0.28	Pieces of emitter matrix broke off and lodged between electrodes.
2-5-73	51	25-59-9/11-58/23-33/51, 52	UO ₂ -W	Long fibers with sharpened tips	1	0.28	No blunting of pin tips observed.
2-19-73	52	Same as Pumpdown 51			32	0.28	Pulsed and D.C. testing used; good agreement between pulsed and D.C. results.

TABLE V-I (continued)

CHRONOLOGICAL SUMMARY OF EMISSION EXPERIMENTS

Installation Date	Pumpdown No.	Sample Designation	Type of Composite	Emitter Configuration	Maximum Current Density ma/cm ²	Active Emitter Area cm ²	Remarks
3-12-73	53	22-81/113-29/11-60/53	Gd ₂ O ₃ -Mo	Fibers recessed ~ 5um below a 1000 Å Au-Coated surface	-	0.3	Unsuccessful first attempt at producing low-energy field-emitted electrons. Fibers shorted to gold coating.
4-2-73	54	25-66-7/113-31Y/54,56,57,58	UO ₂ -W	Fibers kept at a distance of ~ 10um from collector by mica support. Fiber height ~ 10um Sharpened tip fibers	-	0.3	Second attempt to produce low-energy field-emitted electrons. Short circuit occurred.
4-9-73	55	25-99-4/11-67/55	UO ₂ -W	Sharpened tips flush with matrix	0.6	0.3	Produced 0.6 mA/cm ² Low-energy electrons for a few hours.
4-17-73	56	25-66-7/113-31Y/54,56,57,58	UO ₂ -W	Same as for Pumpdown No. 54	-	0.3	Unsuccessful attempt to produce low-energy electrons.

TABLE V-I (continued)

CHRONOLOGICAL SUMMARY OF EMISSION EXPERIMENTS

Installation Date	Pumpdown No.	Sample Designation	Type of Composite	Emitter Configuration	Maximum Current Density ma/cm ²	Active Emitter Area cm ²	Remarks
4-22-73	57			Same as Pumpdown 56			
5-14-73	58	25-66-7/113-31Y/54,56,57,58	UO ₂ -W	Gold coated sample of pumpdown No. 54	120	0.15	Produced rather large currents (~ 20 mA) for about 300 hours. Stable emission.
6-5-73	59	31-12-2/11-71/59,60	UO ₂ -W	Long fibers with hemispherical tips	140	0.15	<u>Very stable emission.</u> Large electrode separation employed - could not produce more than 140 mA/cm ² with available voltage.
6-27-73	60	31-12-2/11-71/59,60	UO ₂ -W	Long fibers with hemispherical tips Electrode separation ~ 1/2 that of Pumpdown No. 59.	120	0.15	Emission unstable. Testing terminated by lodging of piece of emitter matrix between electrodes. Virtually all pins destroyed.
7-9-73	61	22-89-4/30-33/61	Gd ₂ O ₃ -Mo	Short fibers with hemispherical tips.	-	0.3	Very poor, erratic emission performance.

TABLE V-I (continued)

CHRONOLOGICAL SUMMARY OF EMISSION EXPERIMENTS

Installation Date	Pumpdown No.	Sample Designation	Type of Composite	Emitter Configuration	Maximum Current Density mA/cm ²	Active Emitter Area cm ²	Remarks
7-18-73	62	31-39-8/30/ 20-33/62	UO ₂ -W	short fibers with rounded tips. Sample coated with 1000 Å of Mo to electrically connect all fibers	48	0.5	24 mA of stable emission produced for 106 hours.
8-7-73	63	25-59/11-79/ 63	UO ₂ -W	Very long fibers with chiseled tips. Sample attached to SEM pin with silver paste	750	0.022	Maximum current density of 750 mA/cm ² was of short duration. Sample produced ~500 mA/cm ² for about 200 hours.
8-29-73	64	25-59-1/11- 81/23-53/64	UO ₂ -W	Short fibers with hemispherical tips.	450	0.020	Produced stable emission of ~450 mA/cm ² for about 80 hours. Pulsed 60 Hz current approached 1 A.
9-14-73	65	28-89/122-3/ 65	Gd ₂ O ₃ -Mo	Long pins- very high pin density - Mo overcoating	10	0.1	High pin density (35x10 ⁶).

TABLE V-I (continued)

CHRONOLOGICAL SUMMARY OF EMISSION EXPERIMENTS

Installation Date	Pumpdown No.	Sample Designation	Type of Composite	Emitter Configuration	Maximum Current Density ma/cm ²	Active Emitter Area cm ²	Remarks
9-24-73	66	31-39-5/20-37/11-88/66	UO ₂ -W	Long pins with hemispherical tips. Resistive coating on back of sample to give each pin its own repair	20	0.3	No definite effect of resistance observed.
2/23/73	Separate vacuum system	113-25/23-28B/2P	UO ₂ -W	Pointed pins with large cone angle	4	0.1	Long-term emission sample operated for more than 1000 hours.

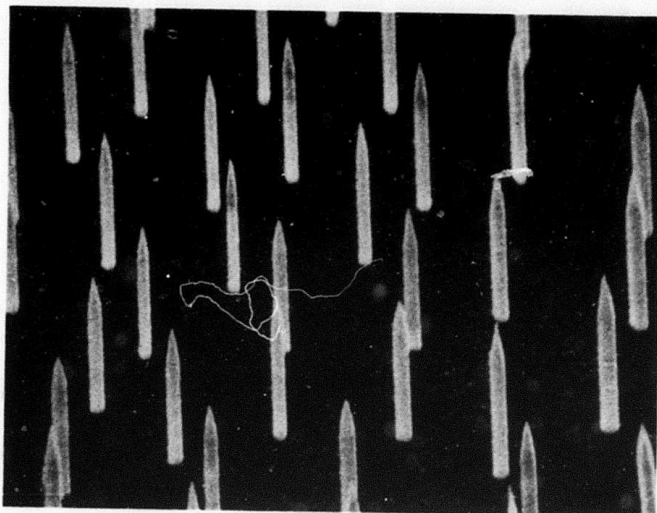
1. Metallic Overcoatings

Metallic overcoating of emitters is potentially attractive as a means of ensuring a good electrical connection to all pins as well as offering the possibility of controlling pin diameter-to-spacing ratio. Another possibility is that of changing the basic material work function by use of the appropriate overcoating. Efforts made during this period were devoted to improving pin-matrix electrical connection and to observe the effects on pin shape and emission by the coating process. Gold was initially employed as the coating material. When SEM post-emission micrographs showed what was an apparent "burning off" of the gold deposition, the coating material was changed to Mo. The Mo coated sample produced good, stable emission and showed no damage to the coating. These particular samples are discussed in detail below.

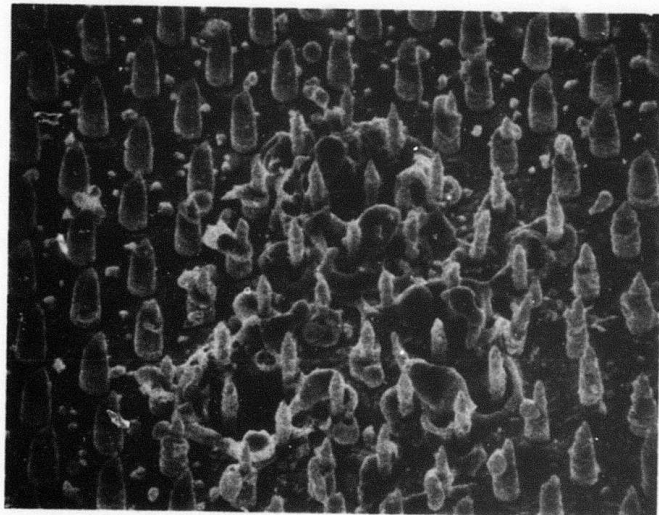
Test sample 25-66-7/113-31Y/54,56,57,58 was overcoated with a layer of gold by sputtering. This particular sample had a previous history of emission testing and thus provided a basis to evaluate the effects of the overcoating. Prior to coating, the sample had operated in a conventional diode giving current densities of about 125 mA/cm^2 for a period of 150 hours and was also used in one of the low voltage diode experiments. Figure V-1a shows the sample prior to emission testing and overcoating. The pins have been selectively

etched to provide sharp conical tips. After being emission tested in the uncoated configuration the pin tips were essentially unchanged. Vapor overcoating resulted in a buildup on the matrix surface and pins. No micrograph was made after overcoating and prior to testing, but Figure V-1b shows an area of the sample after emission testing. Several observations can be made from the photographs. First, the pins have assumed a conical shape with mid diameter about $1.6\mu\text{m}$ and the matrix is coated with gold to a depth of about $1\mu\text{m}$. Several of the pins show areas near the tip where the gold coating either did not adhere to the pin or it has been vaporized by electrical heating. The three areas of damage appear similar to those observed previously near the sites of vacuum arcs, however, no completely destroyed pins can be observed. The arcs could have been supported by the gold coating. When emission tested for 350 hours, this sample produced a maximum current density of about 120 mA/cm^2 , a value comparable to that obtained before overcoating. However, initially, the gold coated sample produced a greater current for the same applied anode potential. The current decreased with time until behavior was nearly the same as before coating.

The reason for this behavior is not entirely established, but a possible explanation is due to the lower work function of the gold coating. It could be possible that the gold coating on the pin tips reduced the effective work function



a) Pre-Emission View of Sample Before Coating with Au. X6350; 45°



b) Post-Emission View of Overcoated Sample Showing Possible Arc Damage. X2500; 30°.

Figure V-1. Pre- and Post-Emission Scanning Electron Micrographs of Sample No. 25-66-7/113-31Y/54,56,57,58.

of the pins thus leading to enhanced emission. After a period of operation, the gold could have been sputtered or vaporized from the tips causing them to revert to the previous uncoated value.

In order to provide a crude test of the above hypothesis, another emitter sample was overcoated with Mo. Such a coating should interconnect all emitter pins but not be as susceptable to removal as was the gold. The UO_2 -W sample, 31-39-8/30/20-33/62, was overcoated with a 1000 \AA° layer of Mo and subjected to emission test. Emission testing produced a current density of about 48 mA/cm^2 with 6.0 kV anode potential. The emission was very stable and operation was continued for a period of 106 hours. At this time, although the capabilities of the power supply were not exhausted, the sample was removed from the test diode. This was done in order to evaluate the effects of operation at this moderate current density, (but large gross current because of the large sample area of 0.5 cm^2) on the emitter morphology. Examination using optical microscopy showed no areas of damage. It is therefore tentatively concluded that metallic overcoating may lead to improved stability of emission by properly interconnecting all pins and smoothing out variations in tip geometry. However, it is likely that only refractory materials can provide the necessary thermal stability.

2. Annealed Tips

Effective operation of a field emitter array requires a very high degree of uniformity of pin tip radii. It has been recognized that tip shaping by surface migration offers a potentially attractive mechanism for achieving uniform emitter tips.^{12,13} When a pointed emitter tip is heated, surface tension forces cause a net migration of atoms from the emitter tip toward the shank and the tip dulls as the tip recedes. It can be shown that the rate of increase of the tip radius is not uniform but decreases rapidly with increasing radius. Therefore, initially sharp but nonuniform tip radii will tend upon heat to asymptotically approach approximately the same radius. It is important to note that the above situation prevails only if there is no large electric field gradient present when the tips are heated. When an electric field is present the additional electrostatic forces must be considered.⁶

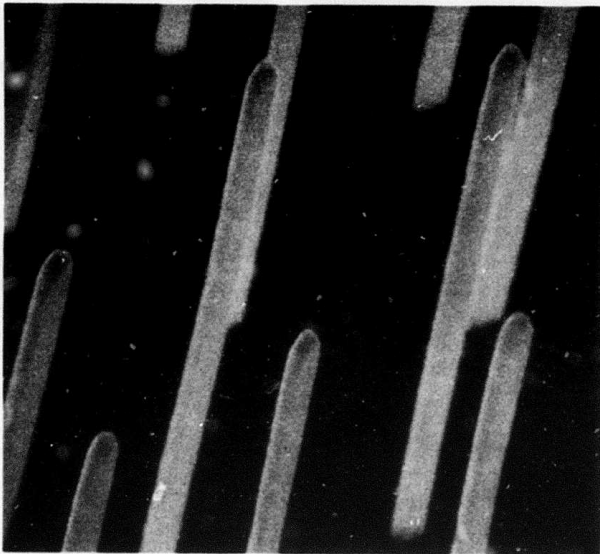
Sample 31-12-2/11-71/59 was fabricated in an effort to apply the rounding technique to the present composites. The pins were initially recessed, rounded by heating, and then re-exposed by etching as described in Section III. Figure V-2a shows a pre-emission scanning electron micrograph of this sample. The pins appear to have reasonably uniform radii and hemispherical tips. There is perhaps some evidence of faceting visible in the photographs.

Emission testing of this sample produced a current density of only 140 mA/cm^2 , but with extremely good

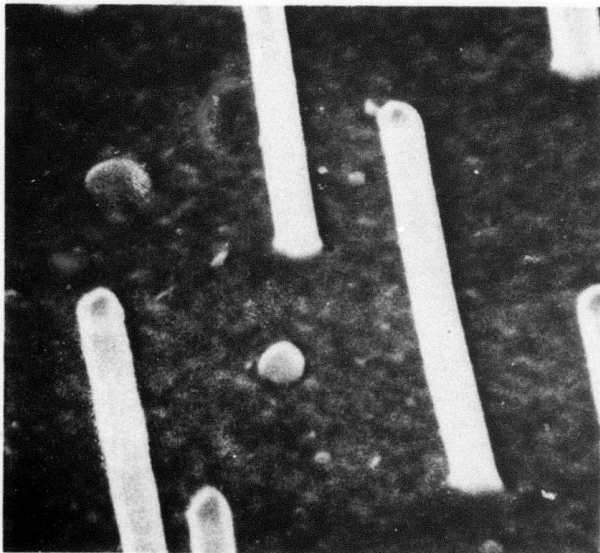
stability of emission. The superior stability was possibly a reflection of the more nearly uniform pins while the low emission current could be explained by the relatively large pin tip radius. After initial emission testing, the sample was removed and subjected to SEM analysis. A post-emission scanning electron micrograph is shown in Figure V-2b. The figure shows what is perhaps some change in the pin tips as well as a few destroyed pins. Overall views of the wafer indicated damage to approximately 5% of the sample area.

In an effort to achieve greater emission, the sample was replaced in the test diode but with a reduced interelectrode spacing. Unfortunately, the emission test did not produce increased current. The observed emission was unstable and several indications of arcing were noted. Eventually, a short circuit developed between the anode and cathode which terminated the emission testing. The cause of the short circuit was found to be a small piece of emitter matrix which had become dislodged from an area in the sample near a grain boundary. Post-emission SEM analysis revealed severe destruction of emitter pins.

The reasons for the poor performance of the sample upon second installation are unclear. A plausible explanation is related to the removal of small portions of the cracked matrix. It is possible that such small particles, perhaps aided in their removal by the high electric field, were vaporized in the interelectrode space thus leading to breakdown. This hypothesis is somewhat supported by the SEM micrographs which



a) Pre-Emission View of Annealed Sample. X12800.



b) Post-Emission View of Annealed Sample. X13000

Figure V-2. Pre- and Post-Emission Scanning Electron Micrographs of Heat Treated UO_2 -W Sample No. 31-12-2/11-71/59.

show not only the characteristic individual pin craters characteristic of the usual vacuum breakdown, but large areas in which the pins are simply knocked down or broken off. Such damage on a more macroscopic scale would accompany arcs caused by material in the interelectrode space.

3. Low Voltage Electron Guns

One of the greatest disadvantages of the usual field emitter is the requirement for a very high electric field which necessitates a large applied voltage. Recently, however, through the use of vapor deposition and photolithographic techniques a family of low voltage field emitters was developed.^{14,15} Such emitters rely on a very short anode-to-cathode spacing in order to achieve the required electric field with moderate potentials. A similar configuration is possible with the oxide-metal composite field emitters. Figure V-3 shows a possible emitter configuration. The W pins were etched below the matrix surface and overcoated with metallic film. The same selective etch and annealing methods were used to shape the pins within their individual holes as was employed with the exposed arrays.

Sample 22-18/113-29/11-60/53 was produced by recessing Mo pins 5 μ m in a Gd_2O_3 matrix and overcoating with Au. The experimental apparatus used to test this low voltage electron gun assembly is shown in Figure V-4. When initially operated

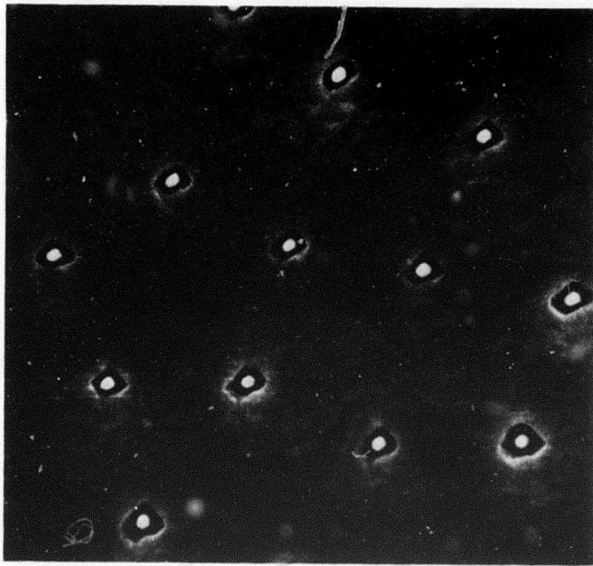


Figure V-3. Scanning Electron Micrograph Showing Type of Recessed Pin Geometry Used In Low Voltage Electron Gun Experiments. UO_2 -W Sample No. 25-99-4/11-67/55 Not Overcoated. X5,270. 0° View.

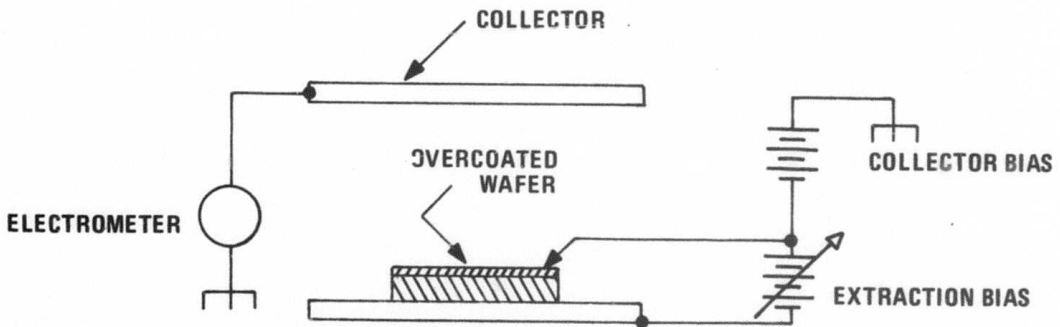


Figure V-4. Schematic Diagram of Gold-Overcoated Low Energy Electron Gun.

measurements indicated a resistance of only about 40 ohms between the accelerating coating and the rear surface of the emitter. However, since the only detrimental effect of the low resistance should be to increase the extraction current requirements, the sample was tested. In operation, no definite emission could be detected from the array. When the extraction potential was increased in an attempt to obtain emission, the gold front coating melted at the point of contact and terminated the experiment.

Subsequent examination of the emitter wafer indicated that the most probable reason for the lack of significant emission was that the pins were too deeply recessed. Such a situation would not only result in a lower than anticipated electric field, but would allow substantial numbers of electrons to be captured by the matrix and thus fail to exit from the material. In order to obtain a more definitive check upon the basic idea, an emitter having a more precisely controlled but comparable pin tip to anode spacing was devised.

Figure V-5 shows the second low voltage emitter configuration tested. The experimental arrangement was basically that used in the usual emission testing except that the interelectrode spacing was held fixed at about $10\mu\text{m}$ by a mica spacer. The anode assembly was vented to permit pumping. The emitter designated 25-99-4/11-67/55, was of the UO_2 -W type having sharpened pins flush with the matrix. An applied voltage of only 280 volts yielded a

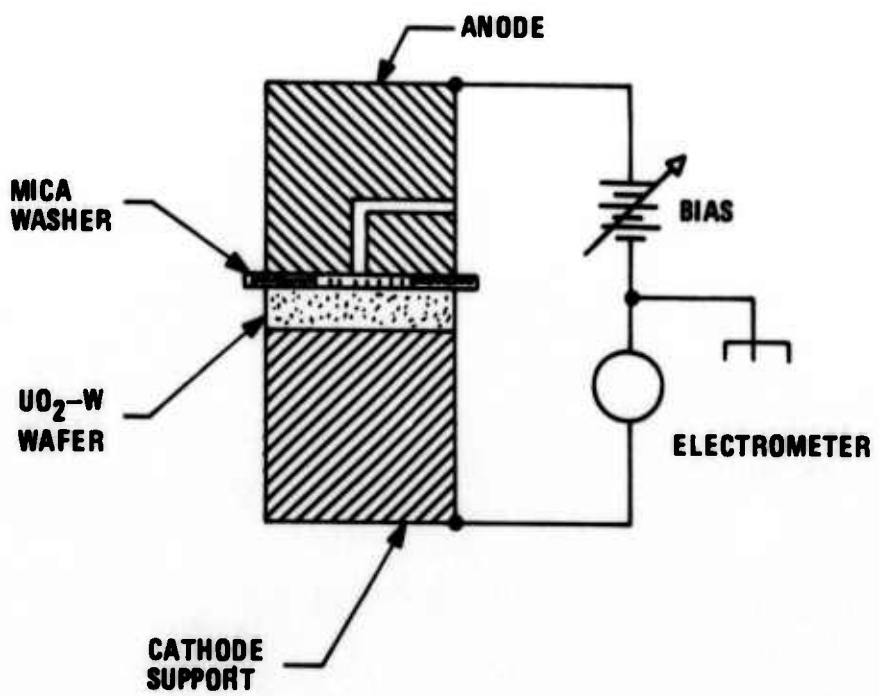


Figure V-5. Conventional Test Diode Modified For Low Voltage Emission

current density of about 0.6 mA/cm^2 for a few hours, after which the emission decayed rapidly. Examination in the SEM revealed little change in the sample due to the emission testing. There was a suggestion that the emitter pin tips might have become slightly blunted as a result of the emission test. Such a change in shape could account for the rapidly decreasing emission current. One possible source of blunting could have been due to ion bombardment of the emitter pins as a result of the relatively high gas pressure within the confined interelectrode region. Such high pressure was probably present as a consequence of the poor pumping conductance between the interelectrode region and the vacuum chamber. The performance of the two low voltage electron emitters was sufficiently encouraging to warrant the production of a third. This also employed the vented anode and mica spacer. In this sample, 25-66-7-113-31Y/56,57, the pins were allowed to protrude $10\mu\text{m}$ above the matrix and a $20\mu\text{m}$ spacer employed to set the interelectrode spacing to about $10\mu\text{m}$ above the pins. Special polishing techniques were used on the anode to reduce the degree of surface irregularity. Unfortunately, successful emission was not achieved with this sample due to a breakdown in the mica spacer resulting in an anode-cathode short circuit. The necessity to continue with other aspects of the research program precluded expenditure of additional effort on the

low voltage emitters. However, it is believed that the general feasibility of the approach was demonstrated. Improvements in etch and coating techniques will undoubtedly contribute to the viability of this emitter configuration. The effects of low resistivity matrices might be eliminated by the application of a layer of insulating material such as alumina prior to overcoating with the conductive anode layer. The optimum shape for such recessed pin geometries received theoretical consideration and is summarized in Section VI of this report.

4. Emission Life-Time Testing

Long-term emission testing was accomplished with the demountable diode structure previously described.¹ This diode, made from pyrex glass and stainless steel, operated with a pressure typically in the neighborhood of 3×10^{-9} Torr. The vacuum system was of the ultra-clean type employing an ion pump together with appropriate ultrahigh vacuum valve and a sorption type roughing pump. Operating procedure called for baking the diode assembly at about 300°C during the pumpdown period of about a week.

The first attempt to test a sample in the long-term diode was terminated when a short circuit developed between the anode and cathode within the diode. The short circuit was caused by a small piece of UO_2 matrix material which had become detached from the emitter. This test was also plagued

by an initial contact between the anode and cathode during bakeout that was a result of the differential thermal expansion between the electrodes and the glass envelope. The maximum current density achieved with this sample was about 10^{-5} A/cm².

The above sample was removed and replaced by UO_2 -W type emitter 113-25/23-28B/2P, a scanning electron micrograph of which is shown in Figure V-6. As can be seen from the figure, the emitter pins were shaped to sharp conical points with a large cone angle. The emitter was placed in the test diode with a spacing sufficient to eliminate the occurrence of a short circuit during bakeout.

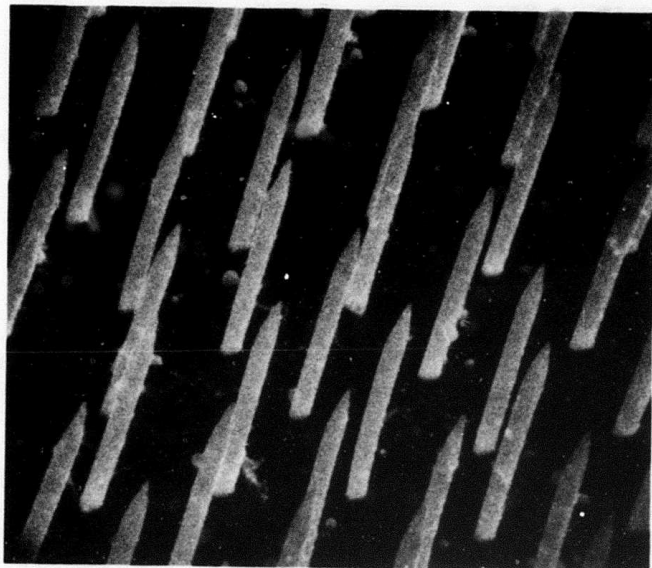
The initial value of current density obtained from the emitter was 4 mA/cm² with 9 kV anode potential. Several interesting phenomena were visible within the glass envelope diode. Several areas of faint, light-blue glow were visible on the anode surface. These areas appeared to vary in size and intensity directly with emission current. The total area covered by the glow was initially estimated to be only about 30 to 50 percent of the cathode. The glowing areas were not stable and appeared to jump about occasionally on the anode surface as well as tend to systematically decrease in intensity and size with time. After a few hundred hours of operation the blue glow was no longer visible at the same anode potential, but could be produced if the anode potential was increased. Such glowing spots have been observed by others.¹⁶



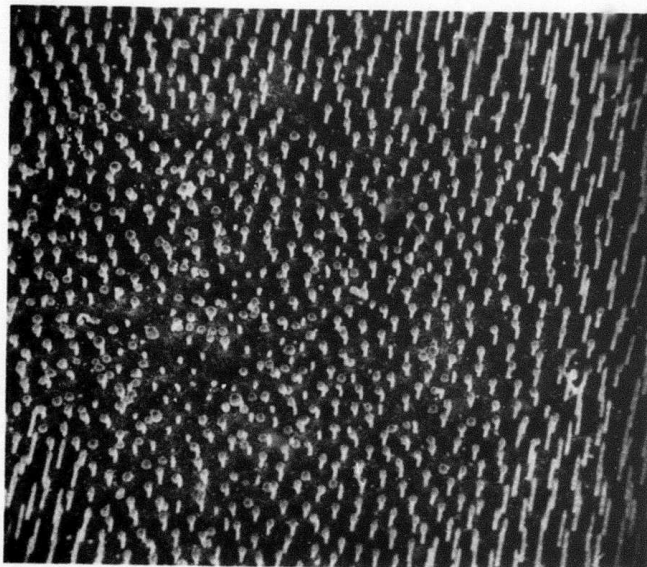
Figure V-6. Scanning Electron Micrograph of Long-Term
UO₂-W Emission Sample No. 113-25/23-28B/P1.
Pre-Emission. X5,695.

Also visible in the diode was a brownish deposit on the glass envelope from the cathode end up to the edge of the anode. Beyond the anode edge, the glass was clear. The sharply defined boundary of the deposit leads to the tentative conclusion that it might be material that was electron sputtered from the anode. An attempt made to analyze the deposit by physical means was unsuccessful due to the scarcity of material.

This second experimental diode operated for a total period of greater than 1000 hours. The total period under vacuum was actually longer since several power supply failures interrupted the test. After the completion of the 1000 hour test period, the sample was removed and subjected to analyses with the SEM. The results of this investigation are seen in Figure 7. Damage was evident in only about 10% of the total sample area. The damage seen in Figure V-7b was of a localized nature. No evidence of large arced areas existed. Note also that the pins were not melted down into the matrix. This behavior may be possibly due to the limited energy capability of the power supply used in the long-term tests. In any case the relatively slight damage to the sample is reflected in the comparatively small change in V-I characteristics taken over the test period.



a) Condition of
90% of Sample
Surface. X7100.



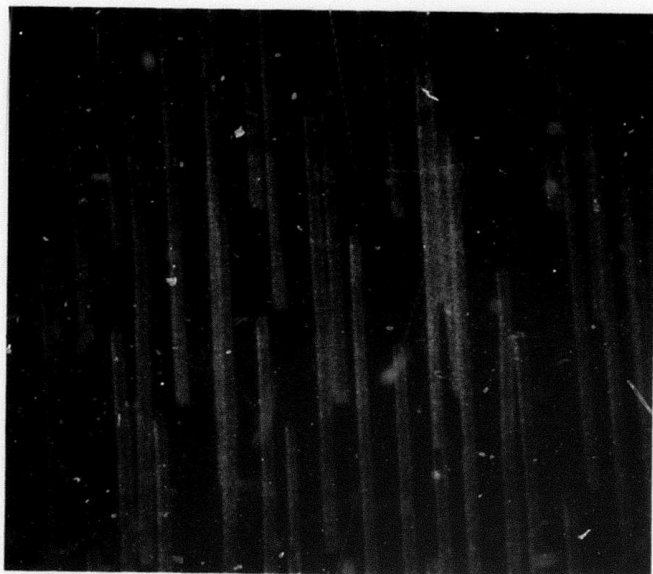
b) Typical Damaged
Areas. X1420.

Post Emission

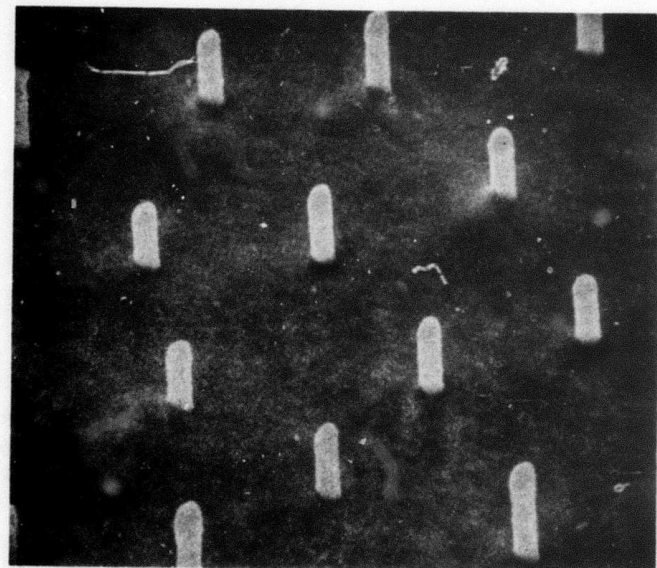
Figure V-7. Scanning Electron Micrographs of Long-Term
 UO_2 -W Sample No. 113-25/23-28B/P2.

5. High Current Density Emitters

As part of the continuing high current electron emitter development program, Samples 25-59/11-79 and 25-59-1/11-81/23-53/64 were prepared and tested. The emitters were produced from the same unidirectionally solidified melt and thus had similar growth characteristics. Preparation was varied so as to evaluate the effects of pin height on emission. Scanning electron micrographs of these samples are shown in Figure V-8. Sample 25-59/11-79 was etched to expose 35 μ m of tip, vapor coated on the back side with Au, and fastened to the Mo cathode support with silver paste. It was necessary to use the silver paste since the sample could not be brazed after application of the Au coating. Both samples were annealed to form hemispherical pin tips; however, during the long etching period required to expose the long length of pin, the etch solution partially attacked the pin material causing a chisel-shaped point to develop. Sample 25-59-1/11-81/23-53/64 was prepared in a similar fashion except the tips were exposed to a length of only about 2.2 μ m. Data showing a comparison of emission current densities are given in Table V-II.



a) Long Pin Sample
X5600



b) Short Pin Sample
X8100

Figure V-8. Pre-Emission Scanning Electron Micrograph of UO_2 -W Annealed Samples No. 25-59/11-79/63 and 25-59-1/11-81/23-53/64.

Table V-II
Comparison of Emission Capability of Samples
Having Short and Long Tungsten Pins

<u>Pin Type</u>	Anode Voltage to Give	
	<u>1 mA</u>	<u>100 mA</u>
short ($2.2\mu\text{m}$)	2.4 kV	6.2 kV
long ($35\mu\text{m}$)	4.8 kV	7.3 kV

These data indicate that a given current density required a substantially greater voltage for the short pin samples. Total current density performance of the two samples was quite similar. The long-pin geometry provided current densities of $300-500 \text{ mA/cm}^2$ during a 100 hour test period with relatively good stability. The voltage required to achieve the maximum current density increased by about 10% during this period. Towards the very last of the test period, efforts to increase the emission current resulted in a temporary increase followed by an immediate decrease. During this increase/decrease process the voltage necessary to produce the original current increased.

The short pin sample provided lower initial current, but eventually with increasing anode potential actually surpassed the other sample. The diode current was increased progressively until it reached about 400 mA/cm^2 at which point it was held for about two days. Voltage required to maintain the current density had not changed by more than

about 5% over this period. At that time, the dc high voltage supply was removed and replaced by an ac supply. A peak current density of about 700 mA/cm^2 was obtained for about one hour, at which time the voltage was increased to obtain a current density of about 1 A/cm^2 . This large value of current density lasted for several minutes until a short circuit developed which terminated the experiment. Subsequent disassembly of the test diode revealed that a small portion of the UO_2 matrix material had broken away and had become lodged in the interelectrode gap thus causing the short circuit.

Post-emission damage to the long pin wafer is quite extensive as can be seen from Figure V-9. Approximately 90% of the pins were destroyed, but no large arced areas are visible. All damage seems to be confined to the destruction of individual pins with the pin usually being melted down below the surface of the substrate. It is likely that destruction of the pins was due to vacuum arcs occurring at individual pin sites.

In contrast to the long pin sample, the UO_2 -W sample with the short pins revealed during SEM post emission examination that 90 to 95% of the pins were unaffected, except for a small area in the corner of the sample where the piece of the composite was dislodged and initiated the major arc. The characteristic geometry of the damaged

individual short pins is shown in Figure V-10. A very shallow crater was formed in the oxide matrix as a result of the arcs. The less extensive matrix damage displayed by the short pin sample may have resulted because of the reduced quantity of metal available to "feed-the-arc" associated with the short as compared to long pins. Cause of these arcs and the failure modes of the composite material emitters in general is discussed later.

6. Other Composite Materials

In addition to the UO_2 -W-type composites, work was continued with other materials, particularly Gd_2O_3 -Mo. Performance of the Gd_2O_3 -Mo type emitters was definitely inferior to the UO_2 -W types. The sample (22-89/122-3 shown in Figure V-11) tested was of a high fiber density ($35 \times 10^6/cm^2$) and had pins of moderate length (3.3 μ m). To ensure electrical contact of all pins, the entire wafer was overcoated with Mo. In electrical emission tests, a maximum emission current density of only 0.3 mA/cm^2 could be obtained. Such low emission current was initially attributed to the poor pin shape coupled with the high pin density. The pin density alone accounted for a reduction in field intensity by a factor of about 3.5 over a similar emitter having pins of the same height and shape, but different densities. Hence as a first approximation, nearly 3.5 times larger voltage would

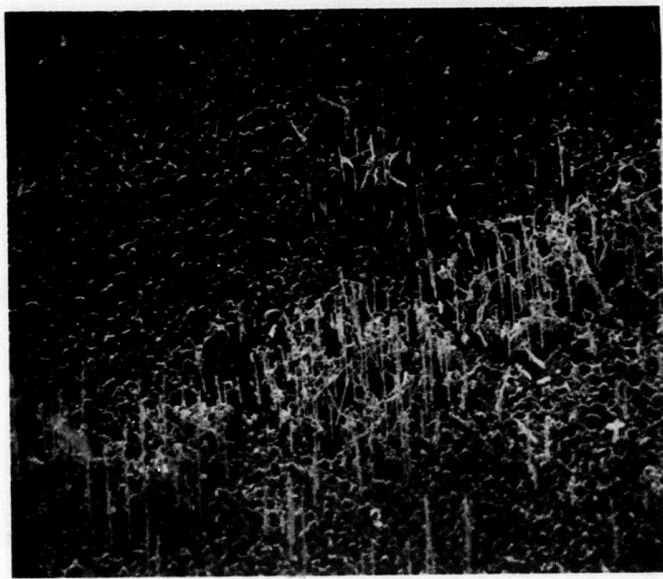


Figure V-9. Post-Emission Scanning Electron Micrograph of UO_2 -W Sample No. 25-59/11-79/63. X800.

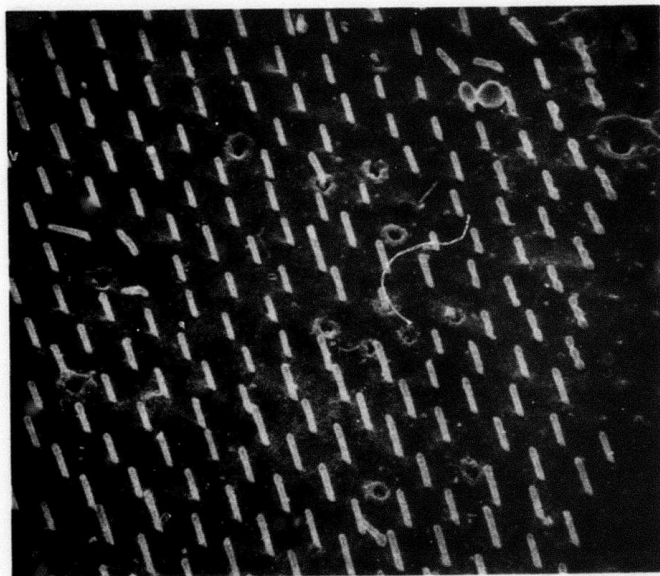
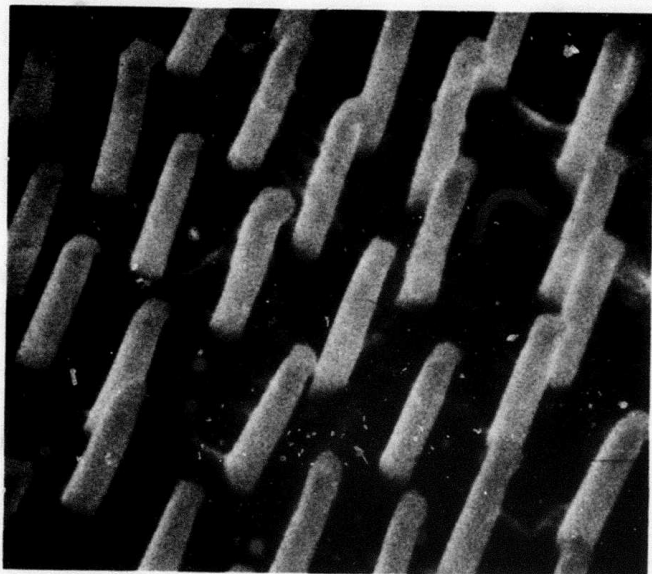


Figure V-10. Post-Emission Scanning Electron Micrograph of UO_2 -W Sample No. 25-59-1/11-81/23-53/64.



Pre-Emission

Figure V-11. Scanning Electron Micrograph of Gd₂O₃-Mo
Sample No. 22-89/122-3. X12,100.

need to be employed. Thus the current obtained with the Gd_2O_3 -Mo sample at a voltage of 7 kV could be obtained from a UO_2 -W type emitter of comparable pin shape at 2 kV.

This situation was observed to be approximately true.

Since an analysis using the simplified theory⁴⁻⁷ shows the density of pins on the UO_2 -W emitters to be greater than optimum, it would seem that the higher density Gd_2O_3 -Mo composites cannot compete with the UO_2 -W types having equivalent pin geometry.

7. Resistive Coated Samples

Previously, it was postulated that resistive coatings could be applied to an emitter in such a manner as to equalize the emission current per pin.² An attempt to experimentally achieve this configuration was made with sample 31-39-5/20-37/11-88/66. The resistive layer was provided by a 2000 \AA film of Al_2O_3 sputtered onto the back surface of the UO_2 -W type emitter. Contact was facilitated by a layer of gold over the Al_2O_3 . The wafer was fastened to the cathode support structure with silver paste.

The theoretical effect of an inserted resistance on the emission is seen in Figure V-12. When the series resistance is properly sized, the maximum emission current is effectively limited thus hopefully precluding destruction of emitter pins. There was no experimental evidence to indicate that such a "break" occurred in the actual V-I

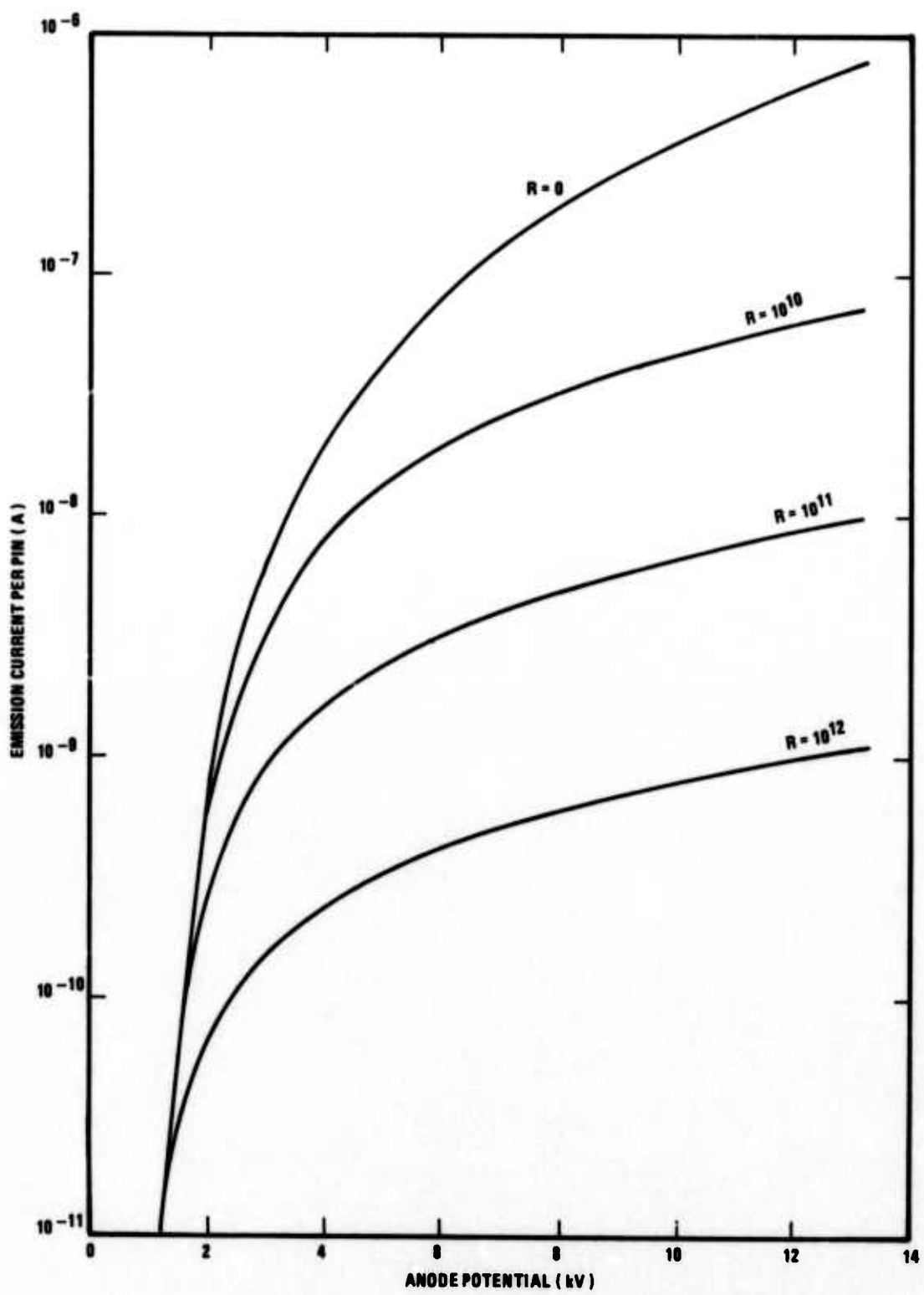


Figure V-12. Predicted Effect of an Individual-Pin Series Resistance Upon Emission Current.

characteristic as predicted by Figure V-12. The feature either did not occur, or was masked in the usual variations in emission current. It is also possible that the effective resistance per pin was sufficiently low so that operating conditions never reached the current limiting regime. The observed short-term stability of the emitter was much better than average, a fact that might be attributed to the resistive coating.

C. ANALYSIS OF EMITTER FAILURE

Data in this and previous reports have represented the termination or reduction of useful electron emission from the oxide-metal composites as being due to the destruction of the emitter pins. While emission could be reduced due to "poisoning" of the pin surface¹⁸, this phenomenon has not been unambiguously observed to occur. The only observed failures have been due to emitter pin destruction. Since the emission is a very strong function of the surface properties, it is quite possible that degradation of emission was due to poisoning, but catastrophic failures were due to the occurrence of pin-destroying arcs. The possible role of localized impurities in electrical breakdown is discussed elsewhere.¹⁹

It is worthwhile to examine a number of post-emission SEM micrographs in an effort to pinpoint common failure

characteristics. When data contained in this and earlier reports are examined, several important characteristics of failures are apparent. These are: (1) destruction usually occurs to individual pins with neighboring pins surviving; (2) large arced areas suggesting the simultaneous melt-down of several pins are rare; (3) pins may be completely destroyed down into the matrix or occasionally only melted down near the tips; (4) a few emitter samples have shown almost complete destruction of the pins, but apparently as a result of a one-by-one sequence. Other observations relevant to emitter failure include: (1) emitters initially operated with a large series resistance limiting the power supply current showed considerably better performance and less damage than did emitters with a lower or zero resistance; (2) emitter failure was not related to the magnitude of the applied anode-cathode voltage; (3) within limits, no dependence of emitter life upon system pressure was observed.

Since examination of post-emission samples indicated destruction by melt-down of the pins, it is appropriate to examine the various potential causes of pin destruction. Suggested modes of pin destruction include: (1) arc damage initiated by bombardment of the emitter tips by positive ions formed in the interelectrode space; (2) high pressure arcs caused by outgassing of the anode structure; (3) vacuum

arcs initiated by resistive heating of the emitter pin followed by vaporization and ionization of the cathode material. The applicability of these three theories to the arc damage occurring in the oxide-metal composites will now be considered.

Ionic bombardment of emitter tips results in energy transfer to surface atoms. In the absence of great electric field, blunting and faceting of the tips will occur. When a large electric field is present, atoms made mobile by energy transfer from the bombarding ions can be extruded so as to form a sharpened emitter tip.¹³ The effects of ionic bombardment should approximate that of thermal heating in these effects. As a result of the extrusion process, the emitter may become sharp enough to initiate extremely high localized emission and subsequent vaporization of material leading to a vacuum arc. Since the energy transferred by bombarding ions is proportional to the anode potential, emitter life should depend upon this potential. This dependence has, however, not been observed and the available experimental evidence does not support the ion-initiated breakdown.

For some time the initiation of vacuum breakdown due to the dislodgement of anode particles has been considered. Early explanations of breakdown between plane electrodes used the "clump" theory.²⁰ This largely empirical formula was later put on a more formal basis.²¹ In essence, the

theory states that the electron beam impinges on the anode causing vaporization of anode material when the power flux at bombarded anode sites reaches a critical value. The value of this critical power flux is $\sim 10^8 \text{ W/cm}^2$. Assuming that the beam size at impact is equal to the pin area, this power flux would require an emission of 10^{-2} A/pin . For a pointed pin an equal flux could be obtained with 10^{-4} A/pin . In both cases the current density per pin is $\sim 10^8 \text{ A/cm}^2$. Examination of various polished anodes has not revealed the existence of small craters such as would be associated with vaporization of material. Other results²¹ indicated that the expansion ratio of electron beams emitted from points 10^{-6} cm in diameter is ~ 300 . This would give an anode diameter of $2 \mu\text{m}$ and is comparable with the usual pin spacing ($4 \mu\text{m}$). Thus it could be reasonably expected that arcs initiated by a single pin could encompass several neighboring pins. This is not usually observed to be true. Hence, a tentative conclusion is that mode for the composite structures is not attributable to vaporization of anode material.

It has also been suggested that breakdown is due to gas being present in the interelectrode gap. This hypothesis is unreasonable since; (1) moderate variation of the vacuum chamber pressure has no effect on breakdown behavior; and (2) gaseous breakdown would not produce the area limited single-pin modes of destruction that occur.

The most likely hypothesis appears to be that breakdown is initiated by resistive heating of the emitter tip, and subsequent vaporization and ionization of tip material.²²⁻²⁵ Upon initial vaporization and ionization a polarized plasma exists above the tip which further enhances the local pin tip electric field.²⁴ This results in cumulative destruction of the individual pin tips, but not the surrounding pins. This tentative hypothesis is reinforced by several observations: (1) isolated individual pins are often destroyed; (2) pins can be melted down into the matrix thus indicating that once destruction is initiated it usually proceeds immediately to completion (if not the initially rounded pin would not produce sufficient current to undergo additional damage).

Previous experimental and theoretical results showed that destruction of emitting pins due to joule heating was likely for emission current densities of the order of 10^7 - 10^8 A/cm².²² This corresponds to a temperature rise $\approx 1000^{\circ}\text{C}$. Evidence obtained in the course of the present research indicates that modifications to pin tip geometry can occur at temperatures considerably lower than predicted by bulk properties. Hence it is likely that onset of tip damage could occur when temperatures were somewhat lower than 1000°C . A problem with this failure analysis is the lack of any exact estimation of the emitted current per pin. The current is certainly not simply the total current divided by the number of pins. While early experimental work³ showed that areas

of good growth correspond to areas of good emission, resolution of the experiment did not extend down to single pins. From data presented in the following chapter, it is seen that the field enhancement factor is extremely dependent upon pin radius. Thus it is possible that initially only a few pins, perhaps ten percent are carrying most of the current. Some of these pins carry sufficient current to cause vaporization of the tip which is then ionized by the electron beam. Additional field enhancement takes place due to the presence of a cloud of positive ions leading to eventual destruction in a vacuum arc. When a very large series resistance is employed, sufficient current to start pin destruction can still be obtained, but destruction is less violent. It is possible for destruction to be initiated but be extinguished when the required peak currents cannot be supplied. This may explain the presence of partially melted pins in samples which were tested with a high value of series resistance. There is considerable evidence showing that the more violent destruction is associated with a low power supply impedance. It is likely that the "conditioning"² that is obtained when emitters are slowly increased in voltage and current, while in series with a large resistance, is due to the initial blunting of highly pointed pins associated with the onset of heating/vaporization. As mentioned earlier, the success of this process

depends upon a careful balancing of the temperature and electric field.¹³

It is possible that selective destruction of a few emitter pins actually enhances the likelihood that neighboring pins will also be destroyed. This could be due to a larger field strength available when the pin density is reduced. Data in this and other reports³ show that the usual pin density of the UO_2 -W emitters is still too great for greatest field enhancement. Hence, when pins situated about a particular test pin are destroyed, the test pin may experience an increase in current. This could cause the test pin to be destroyed and perhaps result in cumulative destruction of several adjacent pins. This phenomenon might also help to explain why the observed total current from an array could actually increase following the destruction of a fraction of its emitter sites.

The above failure analysis while not completely definitive, is an adequate beginning. The main thrust of this effort was to achieve gross current densities with field emission comparable to those obtained with thermionic emitters. Thus, a great number of emitters were investigated, but no single one intensively. A more in-depth analysis should encompass only a single type of emitter. An aid to such a study would be an array of few pins since statistical effects would not be present. These studies will have to wait until arrays of a few pins can be successfully produced.

D. SUMMARY

During this three year program approximately fifty different oxide-metal composite electron emitters were tested in over sixty experiments. A variety of emitter configurations including recessed pin, exposed pin, and shaped pin geometries of various composites were evaluated. Several diode structures were used in the accomplishment of continuous, pulsed and ac emission tests. Current densities of several hundred mA/cm^2 were routinely obtained and current densities of approximately 1 A/cm^2 were observed. A long-term test diode was successfully operated for a period of about 1000 hours with little damage to the emitter pins. The use of metallic overcoatings and resistive layers were investigated as means to obtain more stable emission. Initial efforts to develop a low-voltage ($\sim 100\text{V}$) field effect electron guns met with positive, but limited, success. The effect of pin tip shape and height upon emission were experimentally determined to be in qualitative agreement with available theory. Efforts to isolate the cause of emitter-pin failure resulted in several hypotheses, the most likely being that failure is produced by resistive heating of the pin followed by vaporization, ionization and a vacuum arc. Final experimental data were adequate to outline development programs required to implement specific engineering applications of the composite emitters.

SECTION VI

THEORETICAL ANALYSIS OF ELECTRON EMITTING ARRAYS

A. INTRODUCTION

A theoretical analysis of the field emission current anticipated from a planar array of conducting metallic pins uniformly embedded in an insulating dielectric substrate was undertaken. The potential distribution within the interelectrode space of the device was developed as a function of its geometrical and electrical parameters including the pin height, the pin cross-sectional area, the pin spacing, the pin/anode spacing, and the applied boundary potentials. The electric field strength in the neighborhood of each individual pin was calculated by taking the negative gradient (negative directional derivative normal to the pin surface) of the potential function. The electric field strength at the surface of the pins and the work function of the metal were used in the quantum mechanical field emission equation to obtain the microscopic electric current density, which was integrated over the pin surface to obtain the total current emitted per pin. The total macroscopic current was obtained by summing the individual currents of the several pins.

Previously, the potential distribution in the neighborhood of the pin tips was calculated by analytical methods only; now, however, due to the complexity of the geometry being considered,

purely numerical approaches were also considered. It was observed in the previous studies that the analysis was complicated by the periodicity of the structure and by the closeness of the planar anode structure above the pins. The solution to the Laplace equation for a device with non-periodic spacings of the pins or with pins of a geometry for which the Laplace equation is inseparable, is very complicated if not impossible to solve; and, at best, will produce a solution in the form of a slowly converging infinite series. An alternate approach to this problem was to solve the Laplace equation by purely numerical-type methods and to implement these solutions on a high speed computer.

The research during the present contract period was directed toward the creation of better analytical models and the generation of purely numerical-type solutions to the field emission problem. Since the determination of the electrostatic potential was the most difficult portion of the calculation, initial research was concentrated in this area. Results of both the analytical and numerical solutions are reported here.

The emission characteristics of an isolated pin were first studied. On the basis of the potential distribution in the neighborhood of an isolated pin, an estimation was made of the field enhancement and collection efficiency of an array of pins. Only regular arrays were considered

in this report. The results obtained from the three-dimensional solution of Laplace's equation, together with the several analytical procedures developed, were used to calculate the field emission current. The current density was studied as a function of pin height, pin cross sectional area, pin tip geometry, pin base geometry, pin spacing and pin-anode spacing. The effects of pin-tip radius distributions and unusual interelectrode geometries, e.g., recessed and flush were also investigated.

B. MODEL

A theoretical model of the actual device was developed based on a SEM picture of a typical pin geometry taken at X22,000 showing one of the possible growth modes available. (See Figure VI-1).

The array consisted of brush-like protrusions of needle-shaped conducting metallic pins imbedded in an insulating dielectric substrate. Each pin was characterized by its physical parameters, i.e., by its height, cross sectional area, and shape; the array was characterized by its packing density. (See Figure VI-2).

In terms of a rectangular coordinate system, the array of pins was orientated in the x-y plane with the pins alined in the z direction. The pins were embedded in a dielectric substrate whose upper surface was planar and parallel to the x-y plane. The pin distribution was assumed to be uniform with a spacing x_0 , y_0 . A grounded planar anode was assumed

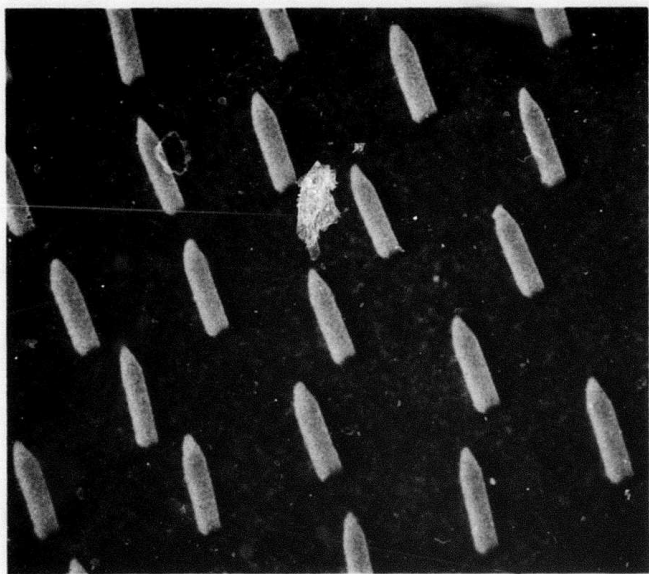


Figure VI-1. Typical Geometry of a Planar Array of Conducting Metallic Pins Embedded In An Insulating Dielectric Substrate.

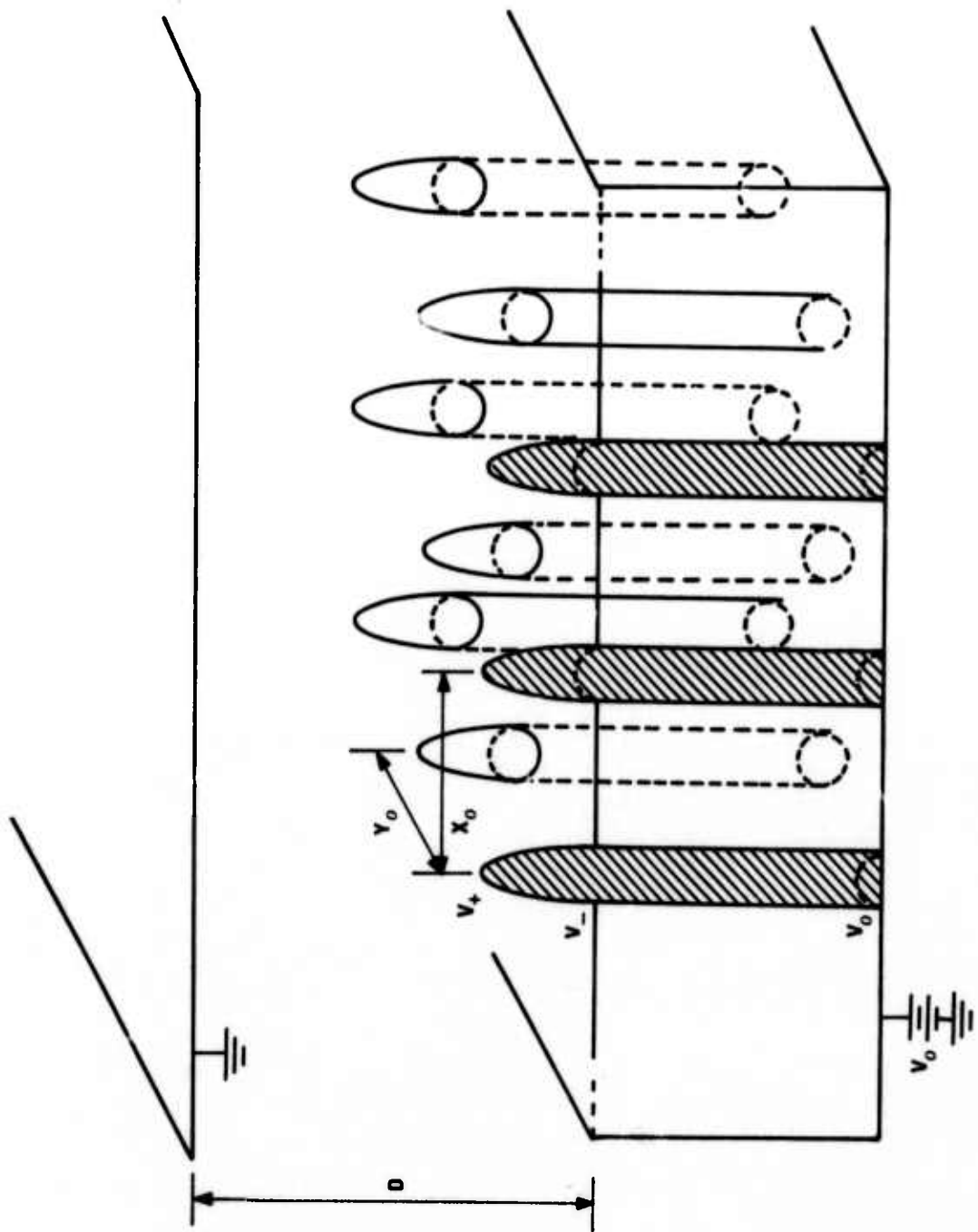


Figure VI-2. Uniform Pin Geometry for the Spheroidal Models.

to be a distance d above and parallel to the x-y plane. The pins and the anode were assumed to be good conductors; the dielectric substrate was assumed to be a poor conductor.

Notice that the boundary potential V_0 was applied to the backside of the dielectric substrate. When the pins drew current, the potential of the pin tips V_+ was reduced somewhat below the steady state value V_0 . Similarly, the potential of the dielectric substrate V_- was also reduced somewhat below the steady state value V_0 .

Each individual pin was modeled by an appropriately oriented and adjusted prolate spheroid. During emission, the major axis of each spheroid was perpendicular to the plane of the substrate and the minor axis of each spheroid was in the plane of the substrate.

If arcing occurred, the geometries of some of the pins no longer fitted a prolate spheroidal model, since the pin had been melted down somewhat, and the pin height was usually no longer greater than the pin radius, which was the assumption for a prolate spheroidal coordinate system; however, the pin geometries then fitted an oblate spheroidal model, in which it was assumed that the pin height was less than the pin radius.

After arcing, each individual pin was modeled by an appropriately oriented and adjusted oblate spheroid. The minor axis of each spheroid was perpendicular to the insulating substrate matrix and the major axis of each spheroid was in the plane of the substrate.

The parameters varied in these models were the height of the pin above the plane of the substrate and the cross sectional area of the pin, i.e., the major and minor axis of the spheroids. Various realistic pin shapes were approximated by these models.

C. NUMERICAL ANALYSIS

A numerical method was developed to solve the Laplace equation for any three-dimensional geometry. This method can be used to calculate the electrostatic potential inside a closed volume with known boundary conditions on the surface enclosing the volume. Inside this region there may be no free charges; however, there may be numerous conducting obstacles, such as emitting pins.

This program was written in FORTRAN V for the UNIVAC 1108 computer. This program was initially limited to the available active core memory of the computer. In order to use this program for multiple pin geometries, a larger grid was required to approximate the curvature of the pin surfaces so that exact derivatives in the field strength calculations could be obtained. Therefore, it was necessary to enlarge the core space available to the program. This necessitated the use of a virtual memory device such as a mass-storage drum. The virtual memory of this device proved to present large input/output times to the program due to the overhead of several routines associated with transfer error tests on

every read or write command. The actual processor time, therefore, was quite large.

In order to check the accuracy of the numerical algorithm, a test run was made with a simple geometry for which the exact solution was known analytically. Good convergence was obtained in the test case as reported earlier.

With the present state of the program, the speed of convergence and the virtual memory available for the array storage is sufficient to allow computational use of the program for arrays which are not too large.

As an application, the program was used to determine the optimum emitting shape of a single conducting pin embedded in an insulating dielectric substrate. The bottom surface of the substrate was grounded; a conducting planar anode was suspended equidistantly above the top surface of the substrate and was held at a fixed positive potential with respect to the ground. It was assumed that the potential applied to the anode was large enough to draw electrons out of the tip of the conducting pin. The conducting pin was assumed to have a cylindrical body with a prolate spheroidal tip. The geometry of the pin tip was varied from that of a prolate spheroid to the special case of a hemisphere. In each case, the area of the base and the total height of the pin were held constant, so that any variation in the resulting current emitted from the device would be due to the shape of the pin tip only. The geometry of the emitting device considered is shown in Figure VI-3.

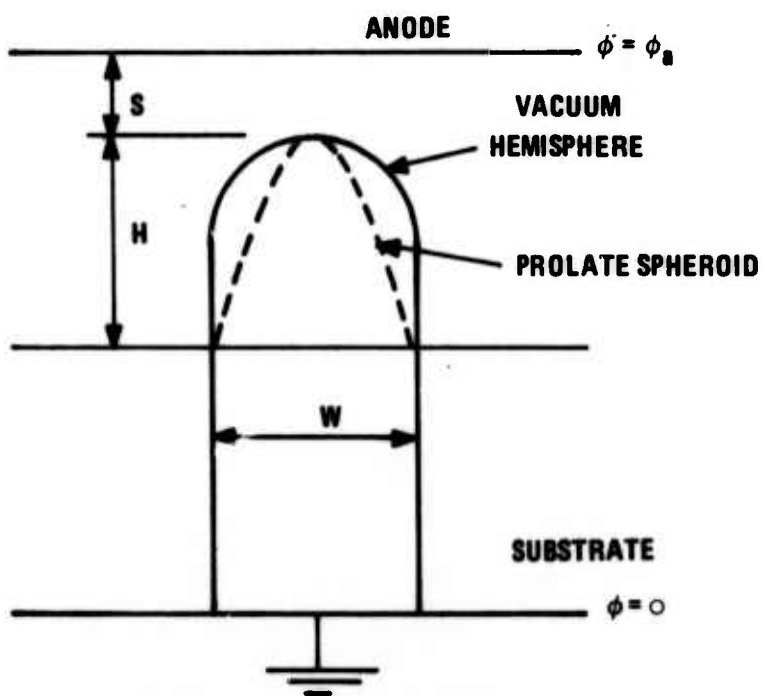


Figure VI-3. Cross-Sectional Geometry of the Exposed-Pin Emitting Device.

To best simulate the conditions found in an actual device, the parameters of the model were chosen to be

$$s = 1\mu\text{m}$$

$$w = \frac{1}{4}\mu\text{m}$$

$$h = 1\mu\text{m}$$

$$\phi_a = 1000 \text{ v}$$

To determine the sensitivity of the total emitted current to the shape of the pin tip, the geometry of the pin tip was varied from that of a prolate spheroid with a height to base ratio of 2 to 1 to the special case of a hemisphere with a height to base ratio of 1 to 1, while keeping the area of the base and the total height of the pin constant. The current produced was not too sensitive to the pin shape; but, the current did increase monotonically with increasing tip height to base ratio. This effect was a result of the increasing potential gradient at the pin tip, where most of the emission occurs, due mainly to the smaller radius of curvature in the intermediate vicinity of the pin tip for the prolate spheroidal case.

Therefore, the optimum emitting shape for the pin tip is a sharp prolate spheroid, however, a hemispherical shape of the pin tip will produce a sufficient emission current.

As an application, the program was also used to determine the optimum position of a single conducting pin embedded inside a hollow cylindrical channel running through an insulating dielectric substrate. The bottom of the substrate was grounded; the top of the substrate was coated with a conducting metal and was held at a fixed positive potential with respect to the ground. A conducting planar anode was suspended equidistantly above the top surface of the substrate and was held at a fixed positive potential with respect to the ground. It was assumed that the potential applied to the anode was much greater than the potential applied to the conducting substrate coating. The conducting pin was assumed to have a cylindrical body with a prolate spheroidal tip. The geometry of the emitting device considered is shown in Figure VI-4.

To best simulate the conditions found in an actual device, the parameters of the model were chosen to be:

$$t = 1/10 \mu m$$

$$w = 1/50 \mu m$$

$$h = 1 \mu m$$

$$\phi_a = 1000 v$$

$$\phi_c = 10 v$$

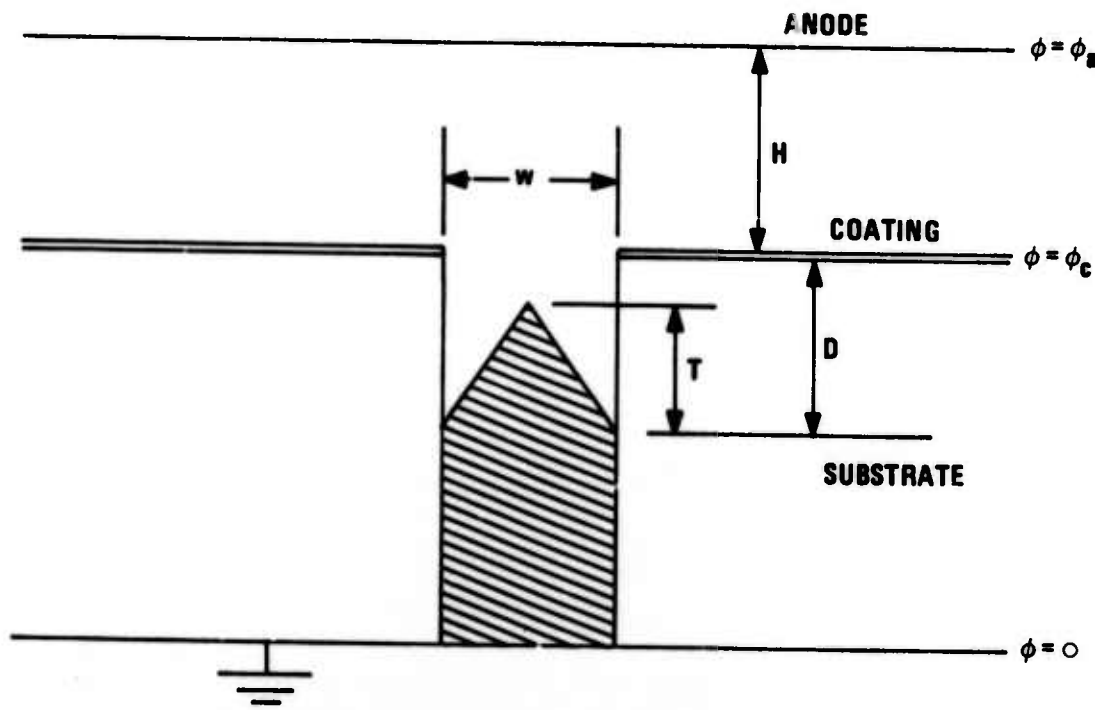


Figure VI-4. Cross Sectional Geometry of the Recessed-Pin Emitting Device.

and

$$t < d \leq 5t$$

The depth of the pin tip below the substrate coating was carried between one and five pin tip dimensions to determine the sensitivity of the total emitted current to the position of the pin within the cylindrical hole through the substrate. The current produced was not too sensitive to position; but, it did decrease monotonically with increasing depth below the substrate coating. This effect is due mainly to the increasing distance of the pin tip, where most of the emission occurs, from the anode surface and the intermediate substrate coating. Also, this effect is due to a decrease in the field gradient in the intermediate vicinity of the pin tip surface due to conductive losses in the dielectric substrate.

Therefore, the optimum position for the pin in the cylindrical hole is such that the tip of the pin is in the plane of the substrate coating.

D. ANALYTICAL ANALYSIS

The prolate spheroidal model and the oblate spheroidal model are now used to model the field emission current for an actual electron emitting array.

Referring to Figure VI-5, let 2ℓ be the length of the major axis of the spheroid. If z_0 is the height of the top half of the spheroid above the xy plane and if ρ_0 is the radius of the cross-section of the spheroid at the xy plane, then

$$\ell = \sqrt{z_0^2 - \rho_0^2} \quad z_0 > \rho_0$$

Also, if the distance from the upper and lower foci of the spheroid to the point r on the surface of the spheroid are denoted by r_+ , and r_- , respectively, then the following definitions are made:

$$u \equiv \frac{r_+ + r_-}{2\ell} \equiv \cosh \zeta \quad u \geq 1$$

$$v \equiv \frac{r_+ + r_-}{2\ell} \equiv \cos \eta \quad |v| \leq 1$$

It follows that

$$\begin{aligned} z &= \ell \cosh \zeta \cos \eta &= \ell uv \\ \rho &= \ell \sinh \zeta \sin \eta &= \ell \sqrt{u^2 - 1} \sqrt{1 - v^2} \\ x &= \ell \sinh \zeta \sin \eta \cos \varphi &= \ell \sqrt{u^2 - 1} \sqrt{1 - v^2} \cos \varphi \\ y &= \ell \sinh \zeta \sin \eta \sin \varphi &= \ell \sqrt{u^2 - 1} \sqrt{1 - v^2} \sin \varphi \end{aligned}$$

and that

$$\left(\frac{z}{\cosh \zeta} \right)^2 + \left(\frac{\rho}{\sinh \zeta} \right)^2 = \ell^2$$

$$\left(\frac{z}{\cos \eta} \right)^2 - \left(\frac{\rho}{\sin \eta} \right)^2 = \ell^2$$

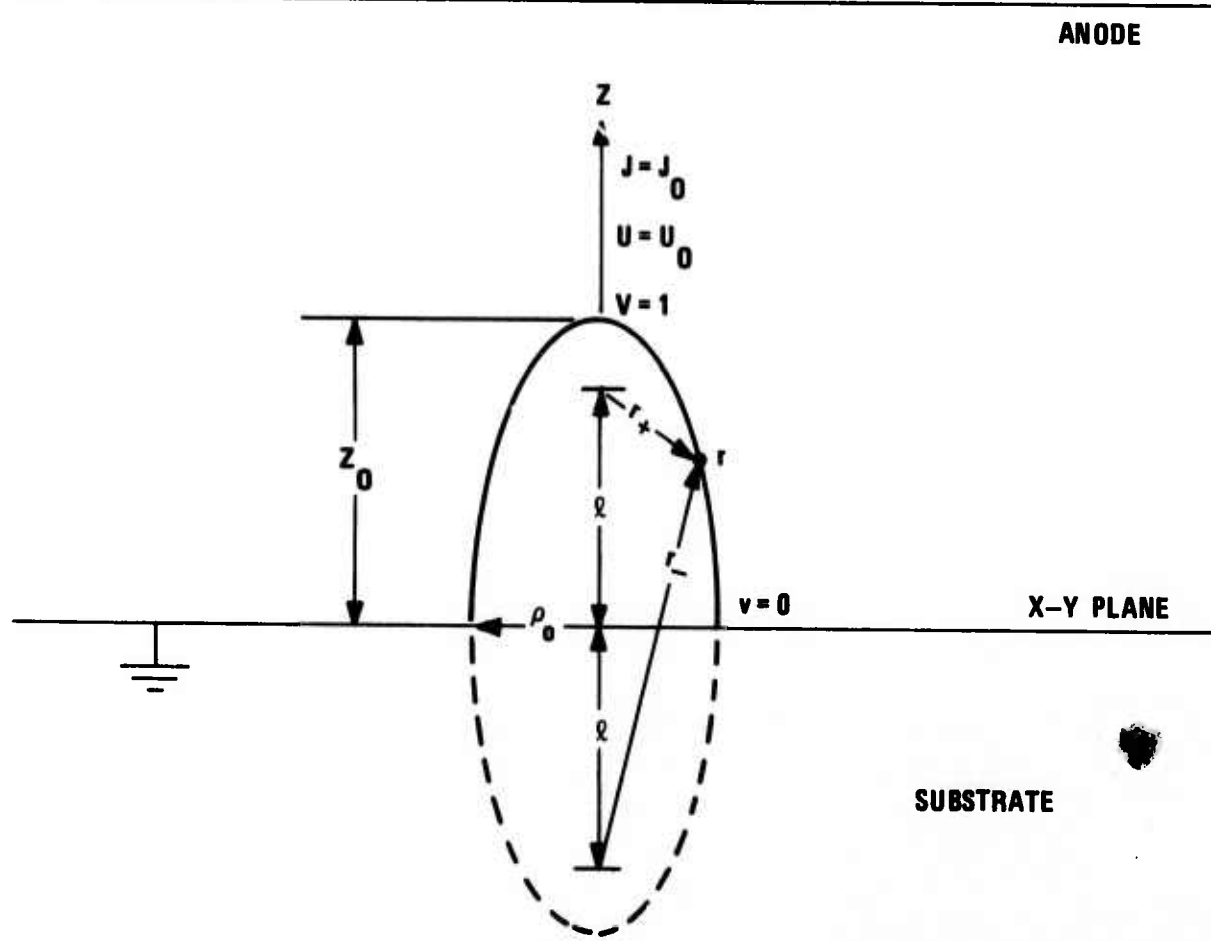


Figure VI-5. Prolate Spheroidal Model; Single Pin Cross-Section

Therefore, $\zeta = \text{constant}$ curves are ellipses and the $\eta = \text{constant}$ curves are hyperbolas. The metrical coefficients are

$$h_u = \ell \sqrt{\frac{u^2 - v^2}{u^2 - 1}}$$

$$h_v = \ell \sqrt{\frac{u^2 - v^2}{1 - v^2}}$$

$$h_\phi = \ell \sqrt{u^2 - 1} \sqrt{1 - v^2}$$

It is assumed that the potential Φ satisfies the Laplace equation everywhere within the electrode space, i.e., let

$$\nabla^2 \Phi = 0$$

where

$$\nabla^2 \equiv \frac{1}{\ell^2(u^2 - v^2)} \left[-\frac{\partial}{\partial u} (1 - u^2) \frac{\partial}{\partial u} + \frac{\partial}{\partial v} (1 - v^2) \frac{\partial}{\partial v} - \frac{u^2 - v^2}{(1 - u^2)(1 - v^2)} \frac{\partial^2}{\partial \phi^2} \right]$$

Fortunately, the Laplace equation is separable in a prolate spheroidal coordinate system. Therefore, let

$$\Phi = UV\phi$$

where U, V, ϕ are functions of u, v, φ alone, respectively.

When the separated Φ is substituted into the Laplace equation and after the variables are separated, there results three uncoupled ordinary differential equations

$$\left[\frac{\partial^2}{\partial \varphi^2} + n^2 \right] \phi = 0$$

$$\left[\frac{\partial}{\partial u} (1 - u^2) \frac{\partial}{\partial u} - \frac{u^2}{1 - u^2} + m(m + 1) \right] U = 0$$

$$\left[\frac{\partial}{\partial v} (1 - v^2) \frac{\partial}{\partial v} - \frac{v^2}{1 - v^2} + m(m + 1) \right] V = 0$$

The solutions of these equations are

$$U_{mn} = a_1 P_m^n (\cosh \zeta) + a_2 Q_m^n (\cosh \zeta)$$

$$V_{mn} = b_1 P_m^n (\cos \eta) + b_2 Q_m^n (\cos \eta)$$

$$\phi_n = c_1 \cos n\varphi + c_2 \sin n\varphi$$

where P_m^n and Q_m^n are the associated Legendre Polynomials of the 1st and 2nd kinds and m and n are integers.

A suitable form of the solution is a linear combination of the product functions, i.e., let

$$\Phi = \sum_{m=0}^{\infty} \sum_{n=-m}^{n=m} c_{mn} U_{mn} V_{mn} \phi_n$$

The constants C_{mn} are found by applying the boundary conditions to the potential

$$\Phi = V_0 = E_0 z \quad z \gg 1$$

$$\Phi = 0 \quad z = 0 \quad \text{or} \begin{cases} u \geq u_0 \\ v = 0 \end{cases}$$

$$\Phi = 0 \quad u = u_0 \quad 0 \leq v \leq 1$$

After the boundary conditions are applied to the solution, the potential ϕ reduces to

$$\phi = E_\infty z \left[1 - \frac{\sigma^+(u)}{\sigma^+(u_0)} \right] = E_\infty z \left[1 - \frac{\sigma^+(\cosh \zeta)}{\sigma^+(\cosh \zeta_0)} \right]$$

where

$$\sigma^+(x) = \coth^{-1} x - \frac{1}{x}$$

and

$$u_0 = \frac{z_0}{\sqrt{z_0^2 - \rho_0^2}}$$

$$\zeta_0 = \cosh^{-1} \frac{z_0}{\sqrt{z_0^2 - \rho_0^2}}$$

The electric field intensity is determined by taking the negative gradient of the potential distribution, i.e., let

$$\underline{E} = -\underline{\nabla} \Phi = - \left(\hat{u} \frac{1}{\zeta} \sqrt{\frac{u^2 - 1}{u^2 - v^2}} \frac{\partial}{\partial u} + \hat{v} \frac{1}{\zeta} \sqrt{\frac{1 - v^2}{u^2 - v^2}} \frac{\partial}{\partial v} + \hat{\phi} \frac{1}{\zeta \sqrt{u^2 - 1} \sqrt{1 - v^2}} \frac{\partial}{\partial \phi} \right) \Phi$$

$$\hat{u} = \frac{1}{\sqrt{u^2 - v^2}} (\hat{\rho} u \sqrt{1 - v^2} + \hat{z} v \sqrt{u^2 - 1})$$

$$\hat{v} = \frac{1}{\sqrt{u^2 - v^2}} (\hat{\rho} v \sqrt{u^2 - 1} + \hat{z} u \sqrt{1 - v^2})$$

$$\hat{\phi} = \hat{\psi}$$

The non-zero components of the electric field are

$$E_u = E_\infty \sqrt{\frac{u^2 - 1}{u^2 - v^2}} v \left[1 - \frac{\tau^+(u)}{\sigma^+(u_0)} \right] = - E_\infty \frac{\sinh \zeta \cos \eta}{\sqrt{\cosh^2 \zeta - \cos^2 \eta}} \left[1 - \frac{\tau^+(\cosh \zeta)}{\sigma^+(\cosh \zeta_0)} \right]$$

$$E_v = E_\infty \sqrt{\frac{1 - u^2}{u^2 - v^2}} u \left[1 - \frac{\sigma^+(u)}{\sigma^+(u_0)} \right] = - E_\infty \frac{\sin \eta \cosh \zeta}{\sqrt{\cosh^2 \zeta - \cos^2 \eta}} \left[1 - \frac{\sigma^+(\cosh \zeta)}{\sigma^+(\cosh \zeta_0)} \right]$$

where

$$\tau^+(x) = \coth^{-1} x - \frac{x}{x^2 - 1}$$

On the surface of the spheroid, the only non-zero component of the electric field is

$$E_u \Big|_{\substack{u=u_0 \\ \zeta=\zeta_0}} = -E_\infty \sqrt{\frac{u_0^2 - 1}{u_0^2 - v^2}} v \left[1 - \frac{\tau^+(u_0)}{\sigma^+(u_0)} \right] = -E_\infty \frac{\sinh \zeta_0 \cos \eta}{\sqrt{\cosh^2 \zeta_0 - \cos^2 \eta}} \left[1 - \frac{\tau^+(\cosh \zeta_0)}{\sigma^+(\cosh \zeta_0)} \right]$$

On the surface of the substrate, the only non-zero component of the electric field is

$$E_v \Big|_{\substack{v=0 \\ u=\frac{\pi}{2}}} = -E_\infty \left[1 - \frac{\sigma^+(u)}{\sigma^+(u_0)} \right] = -E_\infty \left[1 - \frac{\sigma^+(\cosh \zeta)}{\sigma^+(\cosh \zeta_0)} \right]$$

Referring to Figure VI-6, let 2ℓ be the length of the major axis of the spheroid. If z_0 is the height of the top half of the spheroid above the xy plane and if ρ_0 is the radius of the cross section of the spheroid at the xy plane, then

$$\ell = \sqrt{\rho_0^2 - z_0^2} \quad \rho_0 > z_0$$

Also, if the distances from the right and left foci of the spheroid to the point r on the surface of the spheroid are denoted by r_+ and r_- , respectively, then the following definitions can be made:

$$u \equiv \frac{r_+ + r_-}{2\ell} \equiv \cosh \zeta \quad u \geq 1$$

$$v \equiv \frac{r_+ - r_-}{2\ell} \equiv \cos \eta \quad |v| \leq 1$$

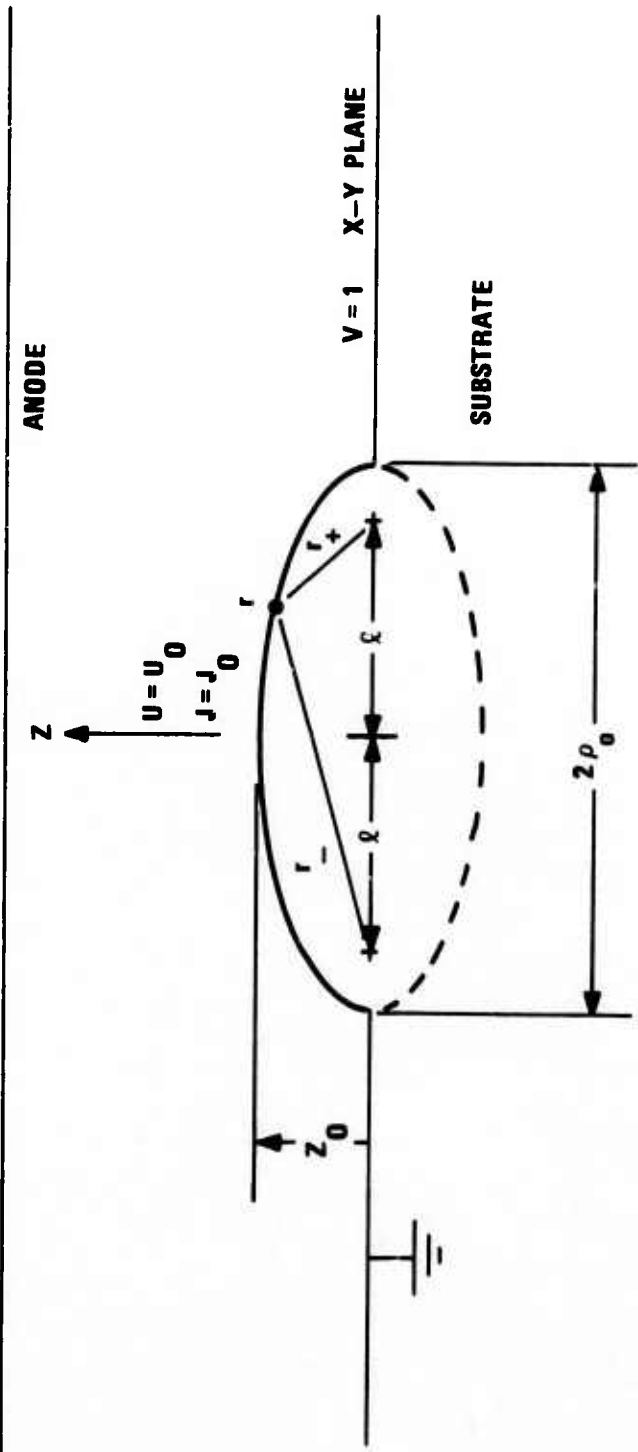


Figure VI-6. Oblate Spheroidal Model; Single Pin Cross-Section

It can be shown that

$$z = \ell \sinh \zeta \sin \eta = \ell \sqrt{u^2 - 1} \sqrt{1 - v^2}$$

$$\rho = \ell \cosh \zeta \cos \eta = \ell uv$$

$$x = \ell \cosh \zeta \cos \eta \cos \varphi = \ell uv \cos \varphi$$

$$y = \ell \cosh \zeta \cos \eta \sin \varphi = \ell uv \sin \varphi$$

and

$$\left(\frac{\rho}{\cosh \zeta} \right)^2 + \left(\frac{z}{\sinh \zeta} \right)^2 = \ell^2$$

$$\left(\frac{\rho}{\cos \eta} \right)^2 + \left(\frac{z}{\sin \eta} \right)^2 = \ell^2$$

Therefore, ζ = constant curves are ellipses, and η = constant curves are hyperbolas. The metrical coefficients are

$$h_u = \ell \sqrt{\frac{u^2 - v^2}{u^2 - 1}}$$

$$h_v = \ell \sqrt{\frac{u^2 - v^2}{1 - v^2}}$$

$$h_\varphi = \ell uv$$

It is assumed that the potential Φ satisfies the Laplace equation everywhere within the interelectrode space, i.e., let $\nabla^2 \Phi = 0$

where

$$\nabla^2 = \frac{1}{\epsilon^2(u^2 - v^2)} \left[\frac{\sqrt{u^2 - 1}}{u} \frac{\partial}{\partial u} u \sqrt{u^2 - 1} \frac{\partial}{\partial u} + \sqrt{\frac{1 - v^2}{v}} \frac{\partial}{\partial v} v \sqrt{1 - v^2} \frac{\partial}{\partial v} + \frac{u^2 - v^2}{u^2 v^2} \frac{\partial^2}{\partial \phi^2} \right]$$

Fortunately, the Laplace equation is separable in a prolate spheroidal coordinate system.

Therefore, let

$$\Phi = UV\phi$$

where U, V, ϕ are functions of u, v, ϕ alone, respectively.

When the separated ϕ is substituted into the Laplace equation and after the variables are separated, there results three uncoupled ordinary differential equations

$$\left[\frac{\partial^2}{\partial \phi^2} + n^2 \right] \phi = 0$$

$$\left[\frac{\sqrt{u^2 - 1}}{u} \frac{\partial}{\partial u} u \sqrt{u^2 - 1} \frac{\partial}{\partial u} + \frac{n^2}{u^2} - m(m + 1) \right] U = 0$$

$$\left[\frac{\sqrt{1 - v^2}}{v} \frac{\partial}{\partial v} v \sqrt{1 - v^2} \frac{\partial}{\partial v} - \frac{n^2}{v^2} + m(m + 1) \right] V = 0$$

To simplify the equations in U and V , let

$$u' \equiv i \sqrt{u^2 - 1}$$

$$v' \equiv \sqrt{1 - v^2}$$

After making this change of variables, the equations in U and V become

$$\left[\frac{\partial}{\partial u'} (1 - u'^2) \frac{\partial}{\partial u'} - \frac{n^2}{1 - u'^2} + m(m+1) \right] U = 0$$

$$\left[\frac{\partial}{\partial v'} (1 - v'^2) \frac{\partial}{\partial v'} - \frac{n^2}{1 - v'^2} + m(m+1) \right] V = 0$$

The solutions of these equations are

$$U_{mn} = a_1 P_m^n(u') + a_2 Q_m^n(u')$$

$$V_{mn} = b_1 P_m^n(v') + b_2 Q_m^n(v')$$

$$\phi_n = c_1 \cos n\varphi + c_2 \sin n\varphi$$

where P_m^n and Q_m^n are the associated Legendre Polynomials of the 1st and 2nd kinds, and m and n are integers.

In terms of u and v or ζ and η :

$$U_{mn} = a_1 P_m^n(i \sqrt{u^2 - 1}) + a_2 Q_m^n(i \sqrt{u^2 - 1}) = a_1 P_m^n(i \sinh \zeta) + a_2 Q_m^n(i \sinh \zeta)$$

$$V_{mn} = b_1 P_m^n(\sqrt{1 - v^2}) + b_2 Q_m^n(\sqrt{1 - v^2}) = b_1 P_m^n(\sin \eta) + b_2 Q_m^n(\sin \eta)$$

$$\phi_n = c_1 \cos n\varphi + c_2 \sin n\varphi$$

A suitable form of the solution is a linear combination of the product functions, i.e., let

$$\Phi = \sum_{m=0}^{\infty} \sum_{n=-m}^{n+m} C_{mn} U_{mn} V_{mn} \phi_n$$

The constants C_{mn} are found by applying the boundary conditions to the potential

$$\Phi = V_o = E_o z \quad z \gg 1$$

$$\Phi = 0 \quad z = 0 \quad \text{or} \quad \begin{cases} u \geq u_o \\ v = 0 \end{cases}$$

$$\dot{\Phi} = 0 \quad u = u_o \quad 0 \leq v \leq 1$$

After the boundary conditions are applied to the solution the potential ϕ reduces to

$$\phi = E_o z \left[1 - \frac{\sigma^-(u)}{\sigma^-(u_o)} \right] = E_o z \left[1 - \frac{\sigma^-(\sinh \zeta)}{\sigma^-(\sinh \zeta_o)} \right]$$

where

$$\sigma^-(x) \equiv \cot^{-1} x - \frac{1}{x}$$

and

$$u_o = \frac{\rho_o}{\sqrt{\rho_o^2 - z_o^2}}$$

$$\zeta_o = \cosh^{-1} \frac{\rho_o}{\sqrt{\rho_o^2 - z_o^2}}$$

The electric field intensity is determined by taking the negative gradient of the potential distribution, i.e., let

$$\mathbf{E} = -\nabla \Phi = -\left(\hat{u} \frac{1}{\ell} \sqrt{\frac{u^2 - 1}{u^2 - v^2}} \frac{\partial}{\partial u} + v \frac{1}{\ell} \sqrt{\frac{1 - v^2}{u^2 - v^2}} \frac{\partial}{\partial v} + \hat{\Phi} \frac{1}{\ell u v} \frac{\partial}{\partial \Phi} \right) \Phi$$

where

$$\hat{u} = \frac{1}{\sqrt{u^2 - v^2}} \left(\hat{\rho} v \sqrt{u^2 - 1} + \hat{z} u \sqrt{1 - v^2} \right)$$

$$\hat{v} = \frac{1}{\sqrt{u^2 - v^2}} \left(-\hat{\rho} u \sqrt{1 - v^2} + \hat{z} v \sqrt{u^2 - 1} \right)$$

$$\hat{\Phi} = \hat{\Phi}$$

The non-zero components of the electric field are

$$E_u = -E_\infty \sqrt{\frac{1 - v^2}{u^2 - v^2}} u \left[1 - \frac{\tau(u)}{\sigma(u_0)} \right] = -E_\infty \frac{\cosh \zeta \sin \eta}{\sqrt{\cosh^2 \zeta - \cos^2 \eta}} \left[1 - \frac{\tau(\sinh \zeta)}{\sigma(\sinh \zeta_0)} \right]$$

$$E_v = -E_\infty \sqrt{\frac{u^2 - 1}{u^2 - v^2}} v \left[1 - \frac{\sigma(u)}{\sigma(u_0)} \right] = -E_\infty \frac{\cos \eta \sinh \zeta}{\sqrt{\cosh^2 \zeta - \cos^2 \eta}} \left[1 - \frac{\sigma(\sinh \zeta)}{\sigma(\sinh \zeta_0)} \right]$$

where

$$\tau(x) = \cot^{-1} x - \frac{x}{x^2 - 1}$$

On the surface of the spheroid, the only non-zero component of the electric field is

$$E_u \Big|_{\substack{u=u_0 \\ \zeta=\zeta_0}} = -E_\infty \sqrt{\frac{1-v^2}{u_0^2-v^2}} u_0 \left[1 - \frac{\tau(u_0)}{\sigma(u_0)} \right] = -E_\infty \frac{\cosh \zeta_0 \sin \eta}{\sqrt{\cosh^2 \zeta_0 - \cos^2 \eta}} \left[1 - \frac{\tau(\sinh \zeta_0)}{\sigma(\sinh \zeta_0)} \right]$$

On the surface of the substrate, the only non-zero component of the electric field is

$$E_v \Big|_{\substack{v=1 \\ \eta=0}} = -E_\infty \left[1 - \frac{\sigma(u)}{\sigma(u_0)} \right] = -E_\infty \left[1 - \frac{\sigma(\sinh \zeta)}{\sigma(\sinh \zeta_0)} \right]$$

E. FIELD EMISSION EQUATIONS

If the pin is at absolute zero temperature, then the electron current density J_o emitted per unit surface area of the emitter is determined by

$$J_o = \frac{e^3 |E|^2}{8\pi h t^2(x) \phi} e^{-\frac{4\sqrt{2m}\sqrt{\phi^3}}{3he|E|} v(x)} \quad (A/cm^2)$$

e = magnitude of the charge on an electron

$|E|$ = the magnitude of the electric field intensity at the surface of the emitter

ϕ = the work function of the emitter

m = the mass of an electron

h = Plank's constant

and

$t(x)$ and $v(x)$ are slowly varying, tabulated functions of (see Table VI-1).

$$x \equiv \frac{\sqrt{e^3 |E|}}{\phi}$$

If the temperature of the emitter is raised to T , ($^{\circ}$ K), then the electron current density J emitted per unit surface area of the emitter is determined by

$$J = J_0 \frac{\pi \tau}{\sin \pi \tau} \quad (\text{A/cm}^2) \quad T \leq T_{\max}$$

where

$$\tau \equiv \frac{T}{T_{\max}}$$

and

$$T_{\max} \equiv \frac{1}{k} \frac{\hbar e |E|}{2 \sqrt{2m\phi} t(x)} \quad (\text{eV})$$

k = Boltzmann's constant $(\text{eV}/{}^{\circ}\text{K})$

TABLE VI-I
VALUES OF THE FUNCTIONS $v(x)$ AND $t(x)$

<u>x</u>	<u>v(x)</u>	<u>t(x)</u>
0	1.0000	1.0000
0.05	0.9948	1.0011
0.1	0.9817	1.0036
0.15	0.9622	1.0070
0.2	0.9370	1.0111
0.25	0.9068	1.0157
0.3	0.8718	1.0207
0.35	0.8323	1.0262
0.4	0.7888	1.0319
0.45	0.7413	1.0378
0.5	0.6900	1.0439
0.55	0.6351	1.0502
0.6	0.5768	1.0565
0.65	0.5152	1.0631
0.7	0.4504	1.0697
0.75	0.3825	1.0765
0.8	0.3117	1.0832
0.85	0.2379	1.0900
0.9	0.0613	1.0969
0.95	0.0820	1.1037
1	0	1.1107

F. THE FOWLER-NORDHEIM PLOT

Let $E = \xi V$ where ξ is the field enhancement factor of the pin and assume that $T \approx 0$, $v(x)$ and $t(x)$ are approximately constants. The field emission equation then takes the form

$$\ln \frac{J}{V^2} = \alpha + \beta \frac{1}{V}$$

A Fowler-Nordheim plot of the field emission equation is constructed by choosing the left-hand side of the above equation as the ordinate, and $1/V$ as the abscissa, then, the resulting Fowler-Nordheim plot of the equation is a straight line (see Figure VI-7). The slope of this line is related to the field enhancement factor ξ and the work function ϕ . When $T \neq 0$, the Fowler-Nordheim plot of the field emission equation is no longer a straight line (see Figure VI-8).

G. PACKING EFFECT

As an example, consider a tungsten pin, with a $2\mu\text{m}$ height on a $1\mu\text{m}$ base radius, placed under a 10,000 V anode separated $10\mu\text{m}$ from the base of the pin. The electric field intensity on the surface of the pin is plotted in Figure VI-9 as a function of the variable $v(0 \leq v \leq 1)$ of a prolate spherical coordinate system. The peak electric field intensity of the pin tips is $2.88 \times 10^7 \text{ V/cm}$. Therefore, the current density emitted from a

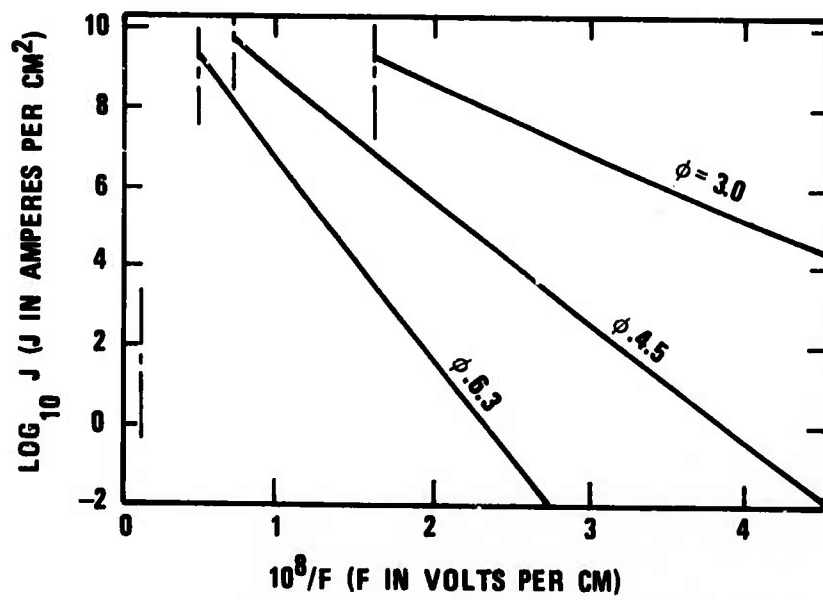


Figure VI-7. Graphs of the Modified Fowler-Nordheim Relation, Showing Field-Current Density J as a Function of the Applied Surface Electric Field E , for Several Values of the Work Function ϕ in ev, at a Temperature of 0°K .

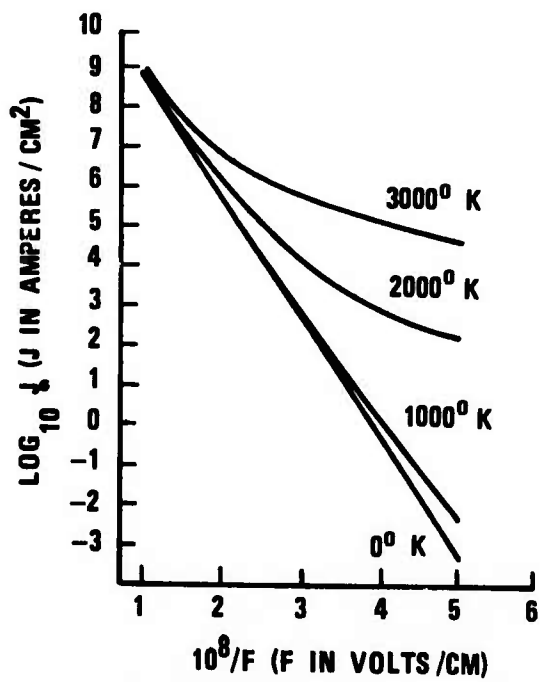


Figure VI-8. Graphs of the Modified Fowler-Nordheim Relation, Showing Field-Current Density J as a Function of the Applied Surface Electric Field E , for Several Values of the Temperature T , for a Work Function of 4.5 ev.

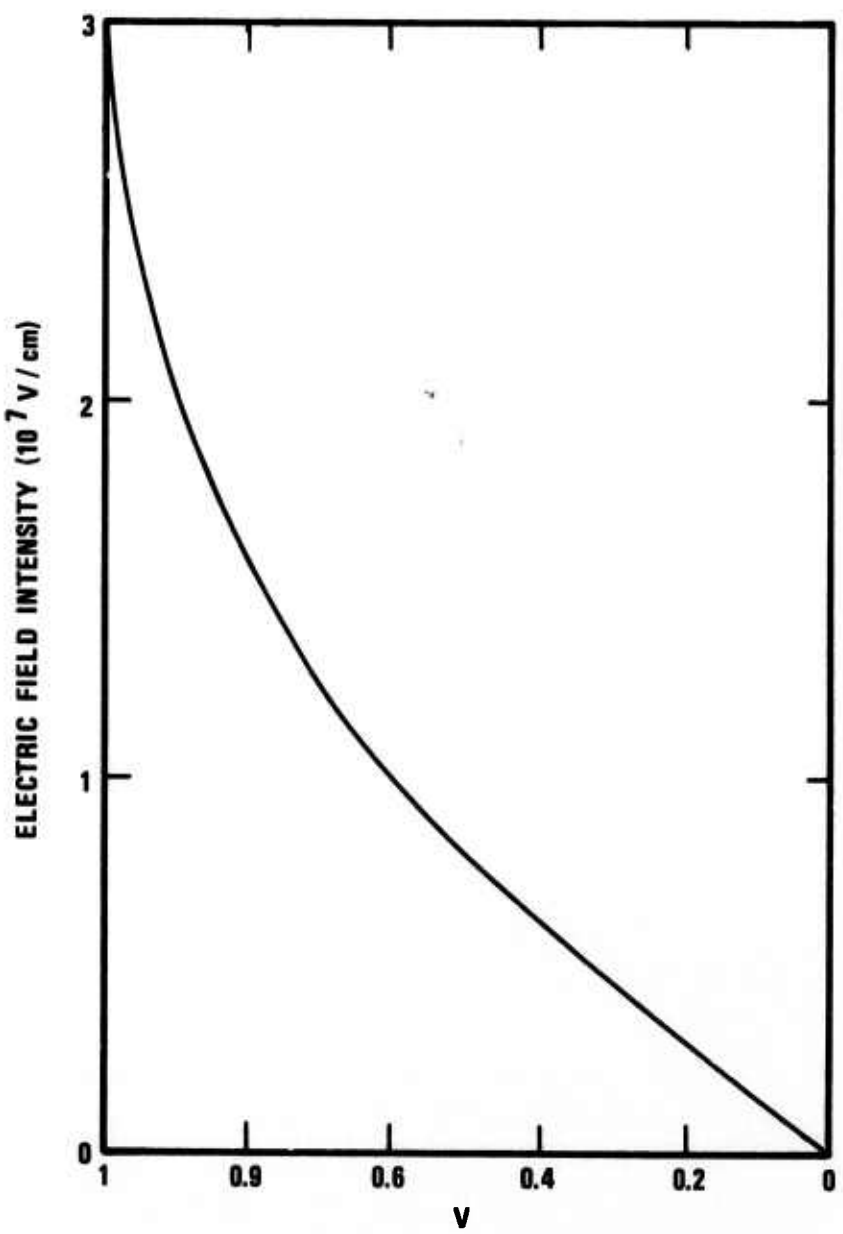


Figure VI-9. Electric Field Intensity on the Pin Surface as a Function of v . Anode Voltage 10 kV; Anode Spacing 10 μ m; Pin Height 2 μ m; Pin Base Radius 1 μ m.

tungsten pin with a work function of 4.5 ev at room temperature of 293 °K is plotted in Figure VI-10 as a function of the variable v ($0 \leq v \leq 1$) of a prolate spheroidal coordinate system. The peak current density at the pin tip is 15.2 A/cm^2 .

Instead of determining the potential distribution over a periodic array of pins, a simple consideration for the packing effect is added.

Consider a pin cathode of total area A across which n pins are regularly distributed. Then,

$$A_c \equiv \frac{A}{N} \equiv \pi \rho_c^2 \equiv \pi l^2 (u_c^2 - 1)$$

represents the mean environmental area which may be ascribed to a single pin cell. Also.

$$A_{c/s} \equiv \pi \rho_o^2 \equiv \pi l^2 (u_o^2 - 1)$$

represents the cross-sectional area of the pin at the substrate surface.

The electric flux ψ_p emitted by the cathode from an isolated pin within the pin radius ρ_o is determined by

$$\psi_p \equiv \int_{\text{pin}} d\mathbf{S} \cdot \mathbf{D} = \int_0^1 dv \int_0^{2\pi} d\phi h_v h_\phi D_u$$

where

$$D_u = \epsilon E_u$$

or

$$\psi_p = D_t A_{c/s}$$

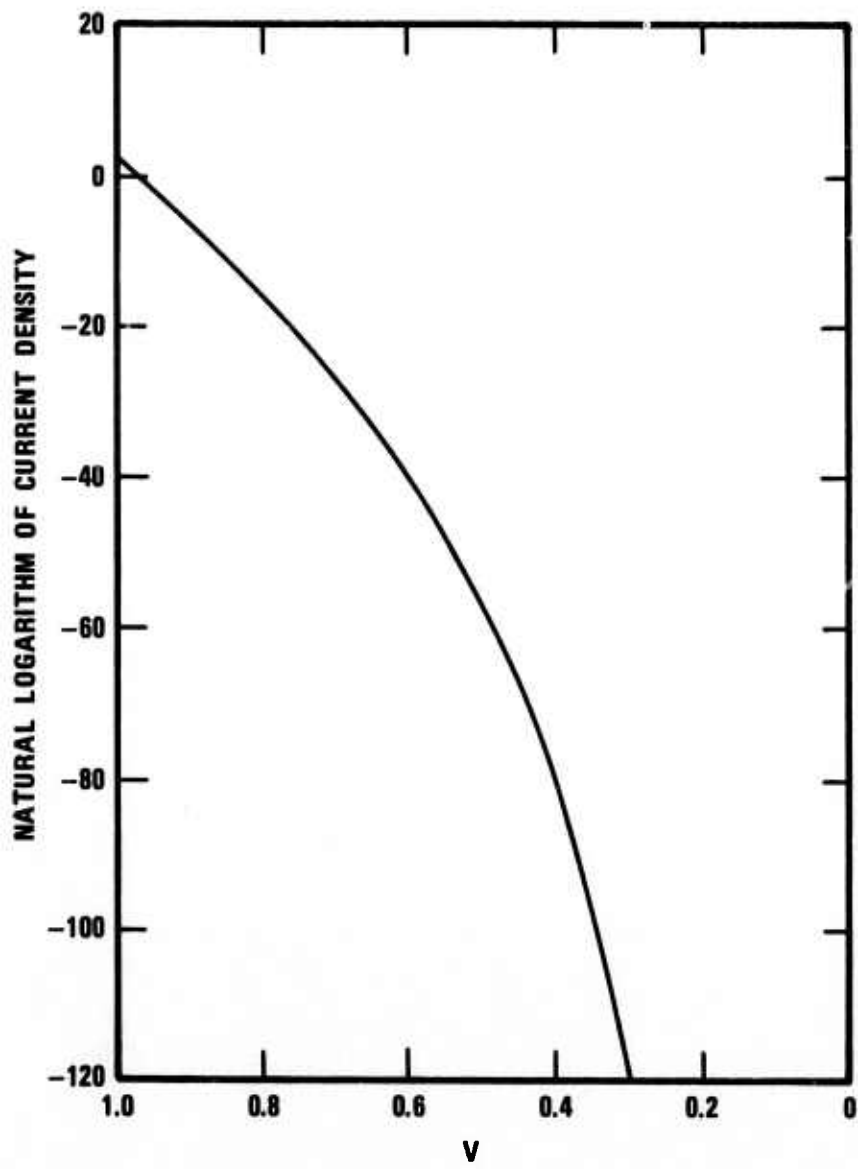


Figure VI-10. Current Density as a Function of v , Assuming a Constant Work Function of 4.5 eV, and a Constant Temperature of 293°K. Anode Voltage 10 kV; Spacing 10 μ m; Pin Height 2 μ m; Pin Base Radius 1 μ m.

where D_t is the electric flux density at the pin tip,
i.e.

$$D_t \equiv D_u \Big|_{u=u_o} = -\epsilon E_\infty \left[1 - \frac{\tau^+(u_o)}{\sigma^+(u_o)} \right]$$

The electric flux ψ_c emitted by the cathode from an isolated pin within the cell radius ρ_c is determined by

$$\psi_c \equiv \psi_p + \int_{\text{cell}} dS \cdot D = \psi_p + \int_{u_o}^{u_c} du \int_0^{2\pi} d\varphi h_u h_\varphi D_v$$

where

$$D_v = \epsilon E_v$$

or

$$\psi_c = D_c A_c + \frac{u_o}{u_c} D_t A_c/s$$

where D_c is the electric flux density at the edge of the cell, i.e.,

$$D_c \equiv D_v \Big|_{u=u_c} = -\epsilon E_\infty \left[1 - \frac{\sigma^+(u_c)}{\sigma^+(u_o)} \right]$$

The mean flux density within the radius ρ_c is determined by

$$\bar{D}_c \equiv \frac{\psi_c}{A_c} = D_c + \frac{u_o}{u_c} \frac{A_c/s}{A_c} D_t$$

Notice that

$$D_t > \bar{D}_c > D_\infty \approx \epsilon E_\infty$$

which demonstrates the field concentration and collection efficiency of an isolated pin.

The mean flux density \bar{D}_c^* of the array of pins is related to the mean flux density \bar{D}_c of the isolated pin through the ratios (1)

$$\frac{\bar{D}_c^*}{\bar{D}_c} \approx \frac{D_t}{\bar{D}_c}$$

where

$$\bar{D}_c^* \approx D_\infty \approx \epsilon E_\infty$$

Therefore, the field enhancement factor ξ is determined by

$$\xi = \frac{\bar{D}_c^*}{D_\infty} \approx \frac{D_t}{\bar{D}_c} = \frac{D_t}{\frac{D_c}{u_c} + \frac{u_c}{A_c} \frac{A_c/s}{A_c} D_t}$$

The field enhancement factor ξ is plotted against the pin cross-sectional radius ρ_o at the substrate surface with the pin height z_o as a parameter for 1×10^6 and 2×10^6 packing densities (see Figs. VI-11 and VI-12) and is plotted against the pin height z_o with the pin cross-sectional radius ρ_o at the substrate surface as a parameter for 1×10^6 and $2 \times 10^6 \mu\text{m}$ packing densities (see Figs. VI-13 and VI-14).

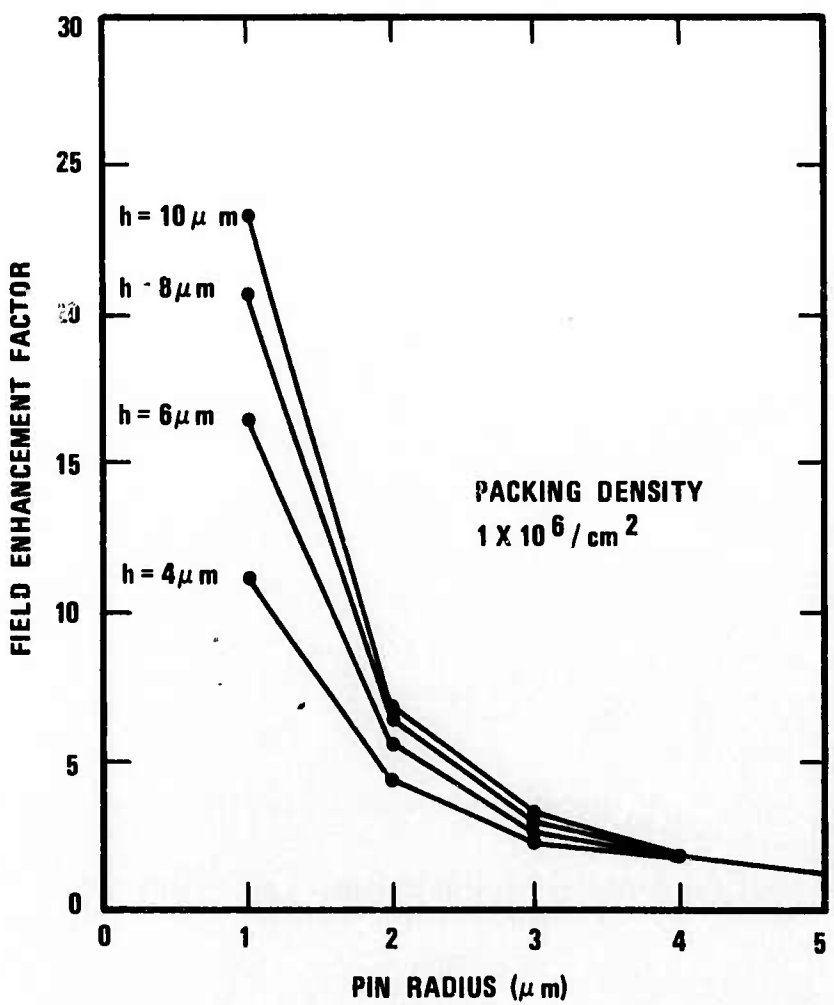


Figure VI-11. Field Enhancement Factor as a Function of Pin Radius, with Pin Height as a Parameter.

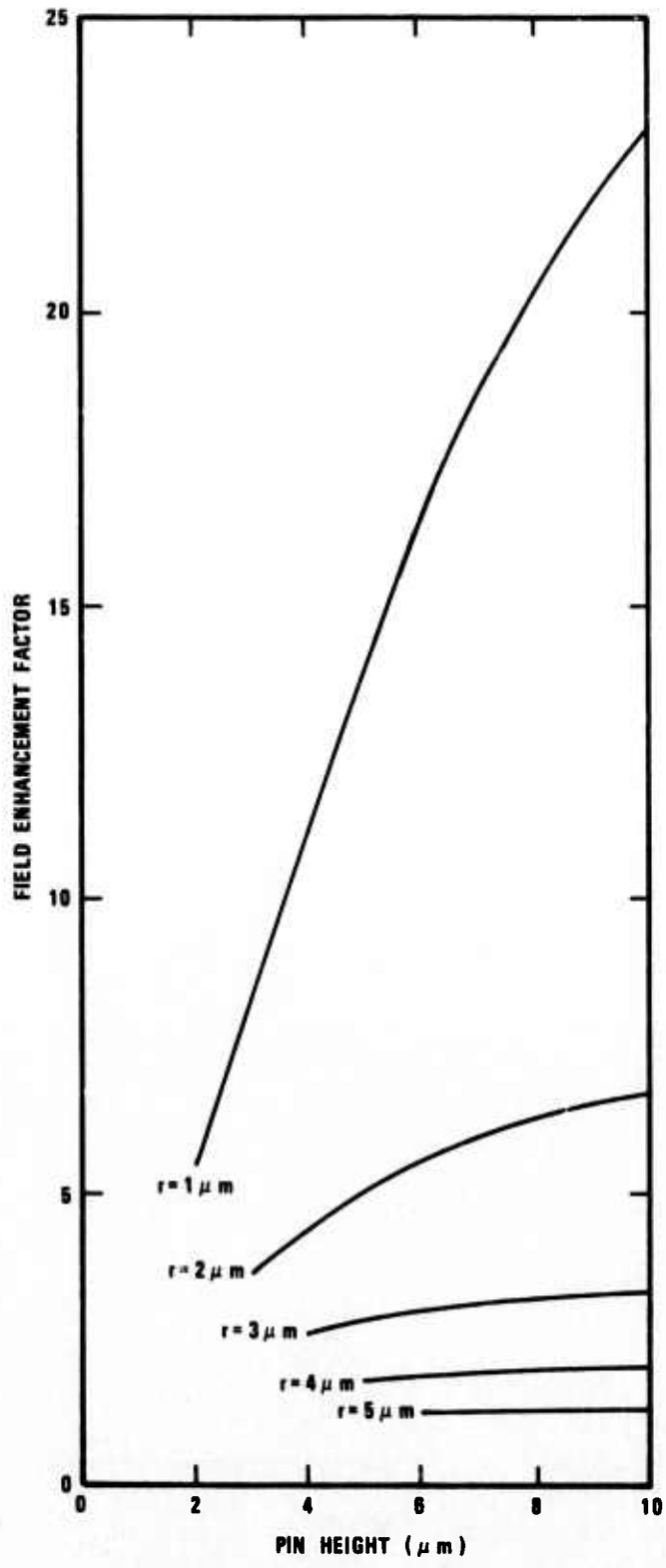


Figure VI-12. Field Enhancement Factor as a Function of Pin Height with Pin Radius as a Parameter. Packing Density is 1×10^6 Pins/cm 2 .

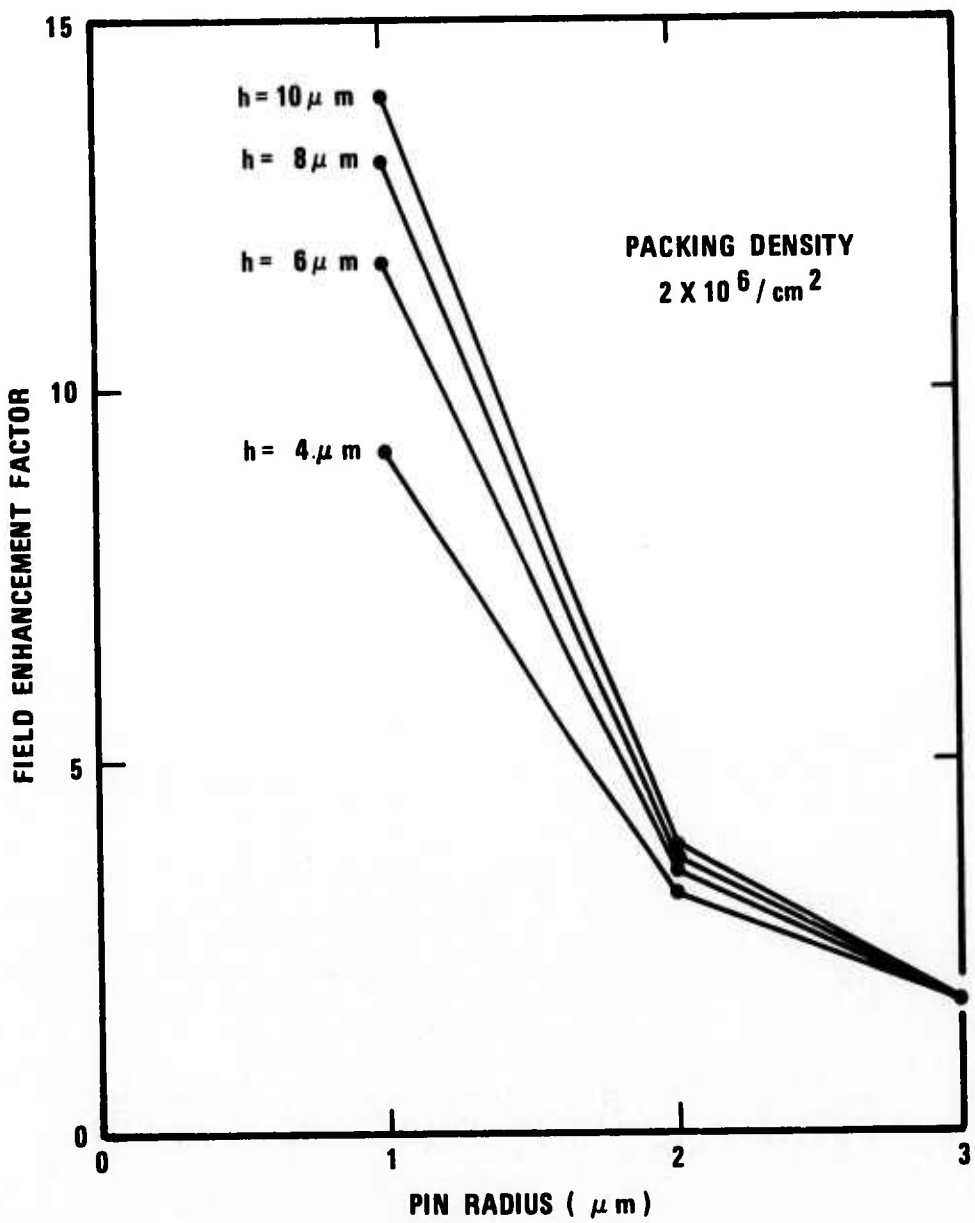


Figure VI-13. Field Enhancement Factor as a Function of Pin Radius with Pin Height as a Parameter.

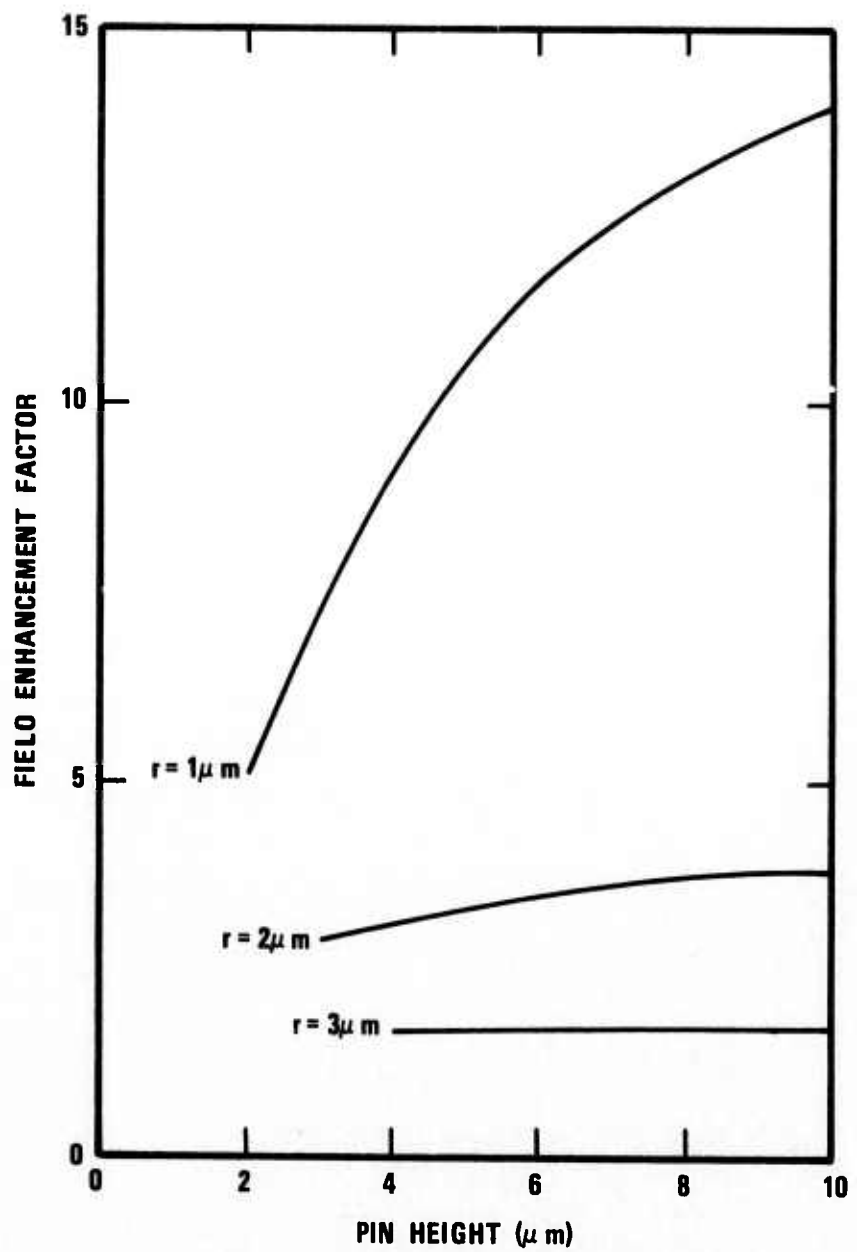


Figure VI-14. Field Enhancement Factor as a Function of Pin Height with Pin Radius as a Parameter. Packing Density is 2×10^6 Pins/cm².

H. SUMMARY

The field enhancement in the vicinity of each pin depends not only on the physical parameters of the pins but also on their arrangement. An individual pin has a greater field enhancement and, therefore, a greater collection efficiency of electric flux lines, if it is sharper, higher, or more distant from the immediately surrounding pins. Therefore, the field enhancement and the collection efficiency of the array decreases with increasing packing density.

SECTION VII

SUMMARY

During the last three and one-half years, oxide-metal composite structures suitable for electron emission testing have been melt-grown under ARPA Order No. 1637. The primary objectives of this study were to investigate the growth process and parameters leading to ordered composite structures during controlled solidification of various oxide-metal mixtures and to produce samples suitable for property evaluation. To meet these objectives the research program was divided into five areas:

- 1) Solidification Behavior of Oxide-Metal Mixtures
- 2) The Formation of Optimum Emitting Arrays
- 3) Oxide-Metal Composite Properties
- 4) Experimental Emission Measurements
- 5) Theoretical Analysis of Electron Emitting Arrays

This section concentrates on achievements obtained during the period since the Semi-Annual Technical Report¹ (January 1973) but, since this is the last report covering the total ARPA program, significant results obtained during prior reporting periods will also be briefly summarized.

At the outset of the research program on "Melt-Grown Oxide-Metal Composites" initiated in 1970, only the systems

UO_2 -W and stabilized ZrO_2 -W had been successfully solidified to yield extensive areas of composite structures. A primary objective of the research was to analyze the solidification behavior of numerous oxide-metal systems to find new systems forming ordered composites, and increase the understanding of the solidification behavior of this unique class of materials. The following list of oxide-metal systems have been successfully unidirectionally solidified during this program to form oxide-metal composite structures (in some systems relatively small composite areas were achieved whereas in others, samples up to 5 cm in length were grown).

TABLE VII-I

OXIDE-METAL SYSTEMS FORMING EUTECTIC STRUCTURES

1. UO_2 -W	6. CeO_2 doped Gd_2O_3 -W
2. Y_2O_3 Stabilized ZrO_2 -W	7. CeO_2 doped Nd_2O_3 -Mo
3. Y_2O_3 Stabilized HfO_2 -W	8. CeO_2 -Mo
4. UO_2 -Ta	9. CeO_2 doped Y_2O_3 -Mo
5. CeO_2 doped Gd_2O_3 -Mo	10. CeO_2 doped Y_2O_3 -W

In addition, limited investigation of several other rare earth oxides (Eu_2O_3 and Ho_2O_3) with CeO_2 and Mo additions indicated these mixtures also formed ordered oxide-metal composite structures.

Also noteworthy in the analysis of oxide-metal solidification behavior was the inability to obtain ordered growth in oxides such as alumina (Al_2O_3) and spinel ($\text{MgO}\cdot\text{Al}_2\text{O}_3$) with the various

refractory metals using either internal or crucible melting techniques. This behavior, along with the successful growth of the systems listed in Table VIII-1, indicated that obtaining a true homogeneous oxide-metal liquid was the primary prerequisite for the growth of aligned composite structures. As a consequence of this parameter, it was soon discovered that oxide stoichiometry played a major role in controlling metal solubilities in systems such as UO_2 -W and CeO_2 -Mo. Doping of the rare-earth sesquioxides with the dioxide, CeO_2 , was shown to significantly increase the solubility of Mo and W in molten Nd_2O_3 and Gd_2O_3 .

The experimental effort to obtain lower temperature oxide-metal systems either using lower melting metals such as cobalt, nickel and iron or with lower melting oxides was unsuccessful. This suggested that, perhaps, the high temperatures ($> 2200^{\circ}C$) are required to disassociate the molten oxide to the extent that it could adequately take the metal into solution on a truly atomic basis.

In the limited experimental work using refractory metal crucibles to encapsulate the molten oxide-metal mixtures composite growth was not nearly as successful as that obtained with the internal induction zone melting technique. Unidirectional oxide-metal solidification in crucibles was plagued by the inability to obtain a well defined and controlled solidification front during growth. Also, the solution of the metal from the crucible into the system made compositional control practically impossible.

In many of the oxide-metal systems listed in Table VII-1, the optimum composition for uniform and extensive composite growth was established as a function of growth atmosphere. Various lowering rates were used to produce composite geometries containing between 5 and 70×10^6 fibers per square centimeter.

Some of the problems associated with the growth in the very high temperatures systems such as UO_2 -W and Y_2O_3 stabilized ZrO_2 -W have been documented. Kinetic processes, such as the depletion of the metal from the molten zone through vaporization and diffusion processes, are active in all systems and these processes must be understood in order to achieve continuous extensive eutectic structures.

A number of parameters which lead to discontinuous, interrupted or banded growth in the oxide-metal systems have been identified. Variable composition, power fluctuations and non-uniform mechanical lowering have been shown to produce interrupted growth.

The mutual orientation between the metal fibers and oxide matrix, and the dominant growth directions of both components in the UO_2 -W and Y_2O_3 stabilized ZrO_2 -W systems have been identified using x-ray diffraction techniques.

In order to successfully utilize this unique class of materials for field emission experiments suitable techniques to form emitting arrays were required. The majority of this development work employed chemical etching and annealing treatments of UO_2 -W samples. Suitable etchants were developed

which dissolved the oxide matrix without attacking the metal fibers leaving an exposed array of pins up to $100 \mu\text{m}$ long.

Various modifications of this etch were employed to sharpen the tips of the individual W pins to form a tip radii of approximately 100 \AA on pins $0.3 \mu\text{m}$ in diameter. Numerous annealing experiments were performed on UO_2 -W samples which showed that the individual W pins could be rounded with heat treatment to yield conical shapes on initially sharp pins or hemispherical caps on blunt pins.

Other etchants were employed which dissolved the metal without effecting the oxide matrix and formed recess pin geometries. Various combinations of etchants were employed to form recessed pins that were pointed. This geometry has excellent prospects for use with insulating and metallic front surface coatings to yield emitting arrays operating at very low applied voltages because of the close pin-anode spacing.

Additional etching studies were conducted with CeO_2 doped Gd_2O_3 -Mo and Y_2O_3 stabilized ZrO_2 -W samples. In the Gd_2O_3 -Mo system both exposed and pointed Mo pins were formed and several of these samples were emission tested.

Concurrent with the etching work was the need to develop suitable means of attaching the composites to a cathode assembly to make a useable emitting structure. Various materials were considered from room temperature silver paste to platinum brazing at 1800°C . After extensive trials it was found that copper brazing worked best and made good contact between the

Mo support structure and the millions of individual metal pins in the oxide-metal composite. Copper also seemed to adequately wet the oxide matrix of the composites when fired in a clean H_2 atmosphere. This selection of a braze making good electrical contact to most of the fibers was responsible for some of the improved emission performance observed during this research program.

During the present report period, an ion beam coater was employed to deposit metallic and resistive layers on both the front and back surface of samples with flush and exposed fibers. Vapor deposited coatings of Au and Mo were deposited on UO_2 -W samples with exposed sharpened pins and a smooth uniform coating was achieved. Front surface coatings were used to assure electrical contact to all the exposed pins. In conjunction with the brazing and coating work, numerous attempts were made to measure the resistivity of the composite and the individual matrix and metal phases. As might be expected, resistivity measurements were very sensitive to the ability to make good contact with the metal pins as well as the oxide matrix. These measurements suggested the oxide had a bulk resistivity in the neighborhood of 10^3 to 10^4 ohm-cm for both UO_2 and the CeO_2 doped Gd_2O_3 matrix. Electrodeposition work was employed to measure the continuity of the fibers in the composites and typically indicated that 70% of the fibers were continuous in single cells. The discontinuous remaining 30% was attributed primarily to fibers growing into cell boundaries.

The major justification for the oxide-metal composite research program was the potential use of these materials for electronic applications, with the major interest on high current field effect emitters. The objective of the experimental emission work was to obtain the maximum electron current densities from a variety of different emitter geometries. Consequently, most of the experiments were run until failure or extensive damage to the cathode structure occurred. In all, over sixty different emission tests were performed in a variety of experimental test diodes. During the latter portion of this program, efforts were made to obtain some life-time data for the better emission geometries. This report also contains an extensive analysis of the possible failure modes for the pin arrays formed from the oxide-metal composites.

At present, the technology exists to produce arrays containing from 5×10^6 to over 50×10^6 single crystal W or Mo pins per cm^2 . Pin tip geometries ranging from hemispherical tips 3000 \AA in diameter to sharpened pins less than 200 \AA across have been produced from UO_2 -W samples. Unfortunately, it has not been possible to perform a systematic evaluation of the pin shapes, spacings, densities and lengths on emission performance in different diode geometries because of the chronological development of many of these parameters. Consequently, as improved emitter structures were obtained through different growth, annealing, etching and brazing

techniques, the new structures were simply emission tested as they became available. In spite of these limitations, many significant achievements were accomplished during the experimental emission portion of this research program and these are briefly summarized.

During the early emission experiments, current densities were limited to several ma/cm^2 at which point major vacuum arcs destroyed large areas of the samples. Improved sample preparation including copper-brazing and better diode bake-out facilities increased the current density to $50-100\text{ ma}/cm^2$ and emitter samples were run for several hundred hours at this current level. For these tests the pin tips were blunt as no effort had been made to round or point the individual metal pins. A major increase in current density ($\sim 500\text{ ma}/cm^2$) was achieved with the development of the sharpened pin structures. Analysis of the pins before and after emission testing showed no gross damage but suggested there was some pin tip blunting which may have helped to improve the current sharing behavior of the total array.

Since the last report¹, a number of unique cathode structures and geometries were tested and these included structures with front surface metallic coating designed to insure electrical contact of all of the pins. This sample operated over 100 hours at $50\text{ ma}/cm^2$ with no apparent damage or deterioration of the cathode structure. Composite structures with the hemispherical tipped pins were tested and generally

exhibited improved current stability. This improvement may be attributed to the more uniform pin tip shape. In an effort to show the potential use of these composite structures for field emitters operating at low voltages, a sample was tested with a very close anode to cathode spacing and produced a current of approximately 0.5 ma/cm^2 at an applied voltage of less than 300 volts.

A specially constructed long-term experimental diode was operated for over 1000 hours with a fairly uniform current density of 4 to 5 ma/cm^2 . A $\text{UO}_2\text{-W}$ sample containing $2 \mu\text{m}$ long pins with hemispherical tips was tested during this report period and maintained a current density between $500\text{-}700 \text{ ma/cm}^2$ for several days at which time the current was increased to over 1.0 A/cm^2 . This current appeared stable for a short period of time at which time a portion of the composite structure dislodged from the cathode structure and terminated the experiment. Post-emission examination of the sample revealed about 5% of the pins were damaged and suggested that with proper selection of cathode geometries current densities of 1.0 A/cm^2 appear feasible using the oxide-metal emitters. Unfortunately, no life-time information is available at this current density.

Efforts to theoretically predict the electron emission from oxide-metal composite structures has advanced to the point where a good qualitative description of emitter behavior is possible. Initial theoretical work centered on a two-dimensional approximation to the emitter array. Such an approach, although not

rigorously correct, provided a rough description of emission dependence upon pin radius, pin density, and interelectrode spacing that qualitatively agreed with experimental results. Later efforts to devise other analytical approximations involved the use of orthogonal sections and provided additional insight into the emission behavior.

Since the exact problem has no analytical solution, a purely numerical approach was undertaken. The numerical method produced results whose accuracy was dependent upon the mesh size used in the calculation of the electric potential. The actual emitter was three dimensional, and therefore the attainment of reasonable accuracy required a very large number of grid cells. The attendant large active storage put severe requirements on the computer used in the calculations. Various schemes were used in order to obtain a large dynamic storage in the available U-1108 Computer. In spite of these efforts, the available computer could not adequately handle a multi-pin array of requisite size in a realistic time period.

In view of the strengths of each of the approaches (analytical and numerical) it was decided to combine the two. This combined approach used numerically calculated (and hence as exact as required) data for a single pin with corrections for the electric flux sharing introduced when several pins were present. This approach, which is outlined in Chapter VI, provides considerable insight into the behavior of the emission. Graphical data are given showing the effect of pin density, pin

radius, and pin height upon the emission. The data, for example, correctly predicts the decrease in emission when pin density is increased from 1×10^7 to $3 \times 10^7/\text{cm}^2$. It is expected that as experience is gained with this method, and additional variables are included in the analysis, that it will prove to be very valuable for emitter performance prediction.

REFERENCES

1. A. T. Chapman, et. al., "Melt-Grown Oxide-Metal Composites", Annual Technical Report (No. 5), ARPA Order No. 1637 and Contract DAAH01-71-C-1046, School of Ceramic Engineering, Georgia Institute of Technology, January 1973.
2. A. T. Chapman, et. al., "Melt-Grown Oxide-Metal Composites", Annual Technical Report (No. 4), ARPA Order No. 1637 and Contract DAAH01-71-C-1046, School of Ceramic Engineering, Georgia Institute of Technology, July 1972.
3. A. T. Chapman, et. al., "Melt-Grown Oxide-Metal Composites", Semi-Annual Technical Report (No. 3), ARPA Order No. 1637 and Contract DAAH01-71-C-1046, School of Ceramic Engineering, Georgia Institute of Technology, January 1972.
4. A. T. Chapman, et. al., "Melt-Grown Oxide-Metal Composites", Final Technical Report (No. 2), ARPA Order No. 1637 and Contract DAAH01-70-C-1157, School of Ceramic Engineering, Georgia Institute of Technology, July 1971.
5. A. T. Chapman, et. al., "Melt-Grown Oxide-Metal Composites", Semi-Annual Technical Report (No. 1), ARPA Order No. 1637 and Contract DAAH01-70-C-1157, School of Ceramic Engineering, Georgia Institute of Technology, January 1971.
6. L. M. Brown and K. S. Mazdiyasni, J. Amer. Cer. Soc. (53) 11 593 (1970).
7. A. T. Chapman, et. al., paper presented at the Pacific Coast Regional Meeting of Am. Cer. Soc., Oct. 30-Nov. 2, 1973.
8. L. M. Hogan, J. Australian Institute of Metals, 7, 228 (1964).
9. B. E. Warren, "X-ray Diffraction", Addison-Wesley Publishing Co., Reading, Mass., 1968.
10. E. N. Aqua and C. N. J. Wagner, Phil. Mag. 9, 565 (1964).
11. O. P. Agnihotri, Phil. Mag. 8, 741 (1963).
12. E. E. Martin, J. K. Trolan, and W. P. Dyke, J. Appl. Phys. 31, 782 (1960).
13. W. P. Dyke, F. M. Charbonnier, R. W. Strayer, R. L. Floyd, J. P. Barbour, and J. K. Trolan, J. Appl. Phys. 31, 790 (1960).

REFERENCES (Continued)

14. C. A. Spindt, J. Appl. Phys. 39, 3304 (1968).
15. C. A. Spindt and J. Kelly, "An Improved Field Emission Cathode for Use in Storage-Tube and Other Electron-Optical Applications", S.R.I. Report November 1970.
16. R. P. Little and S. T. Smith, IEEE Trans. Elect. Devices 77 (1965).
17. J. D. Levine, RCA Rev. 32, 144 (1971).
18. R. Gomer, Field Emission and Field Ionization, Harvard University Press, Cambridge, Mass. (1961).
19. A. P. Komar and V. P. Savchenko, Sov. Phys.-Solid State 4, 986 (1962).
20. L. Cranberg, J. Appl. Phys. 23, 518 (1952).
21. A. Maitland, J. Appl. Phys. 32, 2399 (1961).
22. W. W. Dolan, W. P. Dyke, and J. K. Trolan, Phys. Rev. 91, 1054 (1953).
23. G. N. Fursei and P. N. Vorontsov-Velyaminov, Sov. Phys.-Tech. Phys. 12, 1370 (1968).
24. G. N. Fursei and P. N. Vorontsov-Velyaminov, Sov. Phys.-Tech. Phys. 12, 1377 (1968).
25. G. A. Mesyats, S. P. Bugoev, and D. I. Proskurovskii, Sov. Phys. Usp. 12, 536 (1971).